

EES Batteries

Accepted Manuscript

This article can be cited before page numbers have been issued, to do this please use: B. D. Dandena, D. Tsai, S. Wu, W. Su and B. J. Hwang, *EES Batteries*, 2025, DOI: 10.1039/D5EB00101C.



This is an Accepted Manuscript, which has been through the Royal Society of Chemistry peer review process and has been accepted for publication.

Accepted Manuscripts are published online shortly after acceptance, before technical editing, formatting and proof reading. Using this free service, authors can make their results available to the community, in citable form, before we publish the edited article. We will replace this Accepted Manuscript with the edited and formatted Advance Article as soon as it is available.

You can find more information about Accepted Manuscripts in the [Information for Authors](#).

Please note that technical editing may introduce minor changes to the text and/or graphics, which may alter content. The journal's standard [Terms & Conditions](#) and the [Ethical guidelines](#) still apply. In no event shall the Royal Society of Chemistry be held responsible for any errors or omissions in this Accepted Manuscript or any consequences arising from the use of any information it contains.

Broader context

All-solid-state batteries have garnered increasing interest due to their significant potential for enhanced safety and energy density. However, the only batteries that can currently power electrochemical devices are those that use organic liquid electrolytes. To make solid-state batteries competitive with established technologies, there is a strong need for (electro)chemically stable and superionic solid electrolytes. Sulfide solid electrolytes are promising candidates for all-solid-state lithium batteries (ASSBs) due to their high ductility, improved ionic conductivity, and versatile synthesis methods. Recently, Li argyrodites $\text{Li}_6\text{PS}_5\text{X}$ ($\text{X} = \text{Cl}, \text{Br}, \text{I}$) have been recognized as one of the most promising sulfide electrolytes, thanks to their intrinsically outstanding structures and electrochemical stability, addressing existing limitations. However, their advancement is hindered by significant interfacial incompatibility and rapid dendritic growth. Identifying the factors that influence the interfaces, examining their properties, and proposing mechanisms to address any issues are crucial, as these aspects directly or indirectly affect battery performance. In this review, we explore the factors influencing interfacial phenomena and properties in Li-argyrodite-based ASSBs while summarizing strategies and proposing future directions for developing these batteries.



Review on interface issues of Li-argyrodite-based solid-state Li-metal batteries

[View Article Online](#)

DOI: 10.1039/D5EB00101C

Berhanu Degagsa Dandena ^{1,2}, Dah-Shyang Tsai ², She-Huang Wu ^{3,4}, Wei-Nien Su ^{3,4*}, Bing Joe Hwang ^{1,2,4,5,*}

¹*Nano-electrochemistry Laboratory, Department of Chemical Engineering, National Taiwan University of Science and Technology, Taipei 106, Taiwan*

²*Department of Chemical Engineering, National Taiwan University of Science and Technology, Taipei 106, Taiwan*

³*Nano-electrochemistry Laboratory, Graduate Institute of Applied Science and Technology, National Taiwan University of Science and Technology, Taipei 106, Taiwan*

⁴*Sustainable Electrochemical Energy Development (SEED) Center, National Taiwan University of Science and Technology, Taipei 106, Taiwan*

⁵*National Synchrotron Radiation Research Center (NSRRC), Hsin-chu 30076, Taiwan*

Corresponding authors and E-mail addresses:

Wei-Nien Su: wsu@mail.ntust.edu.tw

Bing Joe Hwang: bjh@mail.ntust.edu.tw



Abstract

View Article Online
DOI: 10.1039/D5EB00101C

Sulfide solid electrolyte-based all-solid-state batteries (ASSBs) offer increased safety, extended cycle life, reduced cost, and increased energy and power density. However, sulfide-based electrolytes exhibit poor interface stability when they contact active materials (anodes or cathodes). The issues of low capacity, inefficient coulombic efficiency, huge polarization, and capacity decay in ASSBs are primarily attributed to sluggish charge transfer kinetics at the interface caused by chemical interactions, electrochemical degradation, weakening interfacial mechanical integrity, etc. Identifying the factors that affect the interfaces, studying the properties of interfaces, and proposing a mechanism to solve the problem are very important, as these properties directly or indirectly impact battery performance. Although the precise mechanism underlying these interface issues remains incompletely understood, combining chemo-mechanical processes and physical and (electro)chemical properties regulate the charge transfer phenomena at the interfaces. In this review, we identify the factors that affect the interfacial phenomena and properties of Li-argyrodite-based ASSBs. Meanwhile, we also summarize the strategies and propose future perspectives to advance Li-argyrodite-based ASSBs.

Keywords: *Interface resistance; solid electrolyte; Li-argyrodite; Li dendrites; solid state battery; interfacial characterization*



1. Introduction

View Article Online
DOI: 10.1039/D5EB00101C

Because of their extended cycle life and greater energy density, lithium-ion batteries are currently highly desirable power sources for electronic equipment and car batteries. However, using an organic liquid electrolyte (LE) for some applications restricts working temperatures and poses safety concerns.^{1, 2} To alleviate these problems, ASSBs with an inorganic solid electrolyte are a safer substitute that can store more energy than micro-batteries while also having good thermal stability.³⁻⁶ The primary concerns with all-solid-state lithium batteries (ASSLBs) are increasing the ionic conductivity (σ) of solid electrolytes (SEs) and ensuring stability between the SE and electrodes.⁶⁻⁸ Due to their relatively fast ion transport at ambient temperature and a moderate electrochemical stability window (ESW), sulfides have acquired much interest among various types of SEs.^{8, 9} Furthermore, sulfides offer an advantage over oxides in cell manufacturing because of their ability to be processed in solution and capacity to deform during cold pressing. The grain boundary resistance of sulfide SEs can be significantly lowered via cold pressing at ambient temperature, eliminating the need for elevated temperature sintering. In ASSLBs, the soft property of sulfide SE helps to provide light contact at the electrode/SE interfaces, inducing a substantial enhancement in cycle performance. Li-argyrodites have favorable electrochemical characteristics for ASSLBs, including high σ .⁹ The electrolyte/electrode interface must be considered despite these various benefits. It has been previously reported that Li-argyrodite SEs $\text{Li}_6\text{PS}_5\text{X}$ (X= Cl, Br, and I) display interfacial reactivity toward layered oxide cathode materials during cycling. $\text{Li}_6\text{PS}_5\text{X}$ can undergo oxidization to produce Li_2S_n , elemental sulfur, P_2S_5 , phosphates, and LiX .¹⁰⁻¹⁴ Moreover, when the sulfide SEs and layered oxide cathodes interact, space-charge layers (SCL) and an elemental mutual diffusion occur. An unstable interface causes cell failure and capacity degradation within ASSBs.^{15, 16} Parallel to this, $\text{Li}_6\text{PS}_5\text{X}$'s incompatibility with Li metal causes an unstable anodic interface, resulting in high interfacial resistance. This leads to unmanageable lithium deposition and results in short circuits. By taking advantage of superior σ , outstanding electrochemical properties, and excellent machinability, it is crucial to boost the compatibility of $\text{Li}_6\text{PS}_5\text{X}$ and electrodes to inhibit interfacial resistance growth and cell short circuits. Consequently, it has been claimed that developing novel SEs with a tendency to make self-limiting interfaces will improve the interfacial stability of SE/electrode.¹⁷

Using Li-argyrodites in a solid-state system offers several interesting benefits over LEs in a liquid system.¹⁸ Firstly, Li-argyrodites can be twisted, punched, and perforated without worrying about safety issues. Secondly, Li-argyrodites have ultra-high σ (approximately 10^{-3}



to $10^{-2} \text{ S cm}^{-1}$)^{19, 20}, which is comparable to that of organic LEs (typically around $10^{-2} \text{ S cm}^{-1}$ at 25°C).^{20, 21} This suggests that SE materials have significant potential for next-generation batteries. Third, Li-argyrodites exhibit greater stability over a wider temperature range than organic LEs, allowing the ASSBs to run effectively within a temperature interval of -30 to +160 °C.²² All these properties show Li-argyrodites great promise for next-generation batteries. However, SE and electrode interfaces pose a significant scientific problem that will prevent the actual deployment of ASSBs.

In this review, we assess interface issues of Li-argyrodite $\text{Li}_6\text{PS}_5\text{X}$ (X= Cl, Br, and I) electrolyte for a range of essential aspects: the interface between Li-argyrodites and anode, the interface between Li-argyrodites and cathode, Li-argyrodite SEs and electrodes assembling issue, and Li-argyrodites and electrodes contact issue. This review also summarizes several advanced interface measurement techniques. Finally, we introduce strategies to improve interface stability and our future perspectives.

2. Interface challenges

Argyrodite-type solid electrolytes, particularly those based on the $\text{Li}_6\text{PS}_5\text{X}$ (X= Cl, Br, and I) family, are considered promising candidates for ASSLBs due to their high lithium-ion conductivity, ease of processability, and relatively low synthesis temperatures.²³ However, despite these advantages, their practical application is hindered by significant interface-related issues.

One of the primary challenges is the chemical and electrochemical instability at the interfaces between the argyrodite electrolyte and electrode materials.^{23, 24} When in contact with high-voltage cathodes (e.g., NMC, LCO), argyrodites tend to undergo interfacial degradation, forming resistive interphases due to the decomposition of thiophosphate species.²⁵⁻²⁷ This leads to increased interfacial impedance, reduced ion transport, and poor long-term cycling performance. In addition, at low potential, argyrodite SEs endures a reduction of phosphorus (around 1.08 V vs. Li/Li⁺) upon electrochemical lithiation and produces Li_2S , LiX and P as a by-product, making it incompatible with Li metal.²⁸⁻³⁰ Argyrodite SEs also produces Li_2S , LiX and Li_3P as a by-product when in contact with Li metal (chemical decomposition).³¹

Furthermore, argyrodites often suffer from poor mechanical properties, which can result in interfacial contact loss during battery operation due to volume changes in active materials or



insufficient densification during cell assembly. This mechanical mismatch contributes further to increased resistance and capacity fading.³²

Therefore, addressing the chemical incompatibility and mechanical instability at the electrolyte–electrode interfaces is critical for unlocking the full potential of argyrodite-based ASSLBs.

In ASSLBs, undesirable physical and chemical interactions at corresponding electrolyte/electrode interfaces generate large gaps between expected and actual performances. The major issues of electrolyte/electrode interfaces in ASSLBs are depicted in Fig. 1a.

Inadequate contact between the SE and the electrode can limit the effective interfacial area. For instance, many SEs are inherently lithiophobic due to their high interfacial energy with Li metal, often resulting in contact angles greater than 90° when in contact with Li. This poor wettability hinders intimate contact and reduces the area available for efficient Li-ion transport.³³ Additionally, designing hierarchically interconnected microstructures in non-Li-based electrodes is challenging, as it demands meticulous control over the shape, size, and spatial arrangement of the electrolyte, active materials, and electronic conductors. If these microstructures are not properly optimized, the contact area for charge transfer at the electrolyte–electrode interface can be substantially diminished.³⁴ Furthermore, the rigid nature of solid–solid interfaces prevents them from adapting to the volume changes of active materials during cycling, accumulating mechanical stress. Over time, this cyclic stress can initiate and propagate cracks at the interface, progressively weakening the interfacial contact.³⁵

Sluggish charge transfer kinetics at the SE/electrode interface can raise the area-specific resistance. Side reactions often exacerbate this, which may occur when the electrode's operating potential lies outside the electrolyte's electrochemical stability window.³⁶ Such reactions irreversibly consume the SE and/or electrode materials, producing interphase layers that are electronically conductive but poorly conductive for Li-ions. These interphases may promote further parasitic reactions or serve as barriers that impede Li-ion transport across the interface.³⁷ Additionally, mismatches in Li-ion chemical potential between the electrolyte and the electrode material can lead to the formation of space charge layers at the interface. These regions, often characterized by local lithium depletion and reduced ion diffusion coefficients, further hinder effective Li-ion transport.³⁸



Li dendrite growth at the Li/SE interface or within the SE can lead to serious short circuits. Dendrite formation is driven by uneven electric fields, which are amplified near protrusions on the lithium surface due to the tip effect and non-uniform Li-ion flux.³⁹ The resistance to dendrite growth arises from the strain energy needed to deform the SE and the interfacial energy associated with expanding the contact area. Dendrite growth can occur spontaneously when the driving forces surpass these resistive barriers. Furthermore, although ideal SEs would conduct only Li-ions, most current materials exhibit some degree of electronic conductivity. In highly electron-conductive electrolytes, electrons can migrate from the lithium metal into the electrolyte, lowering its local electrochemical potential. During charging, this may reduce the electrolyte's potential below 0 V vs. Li/Li⁺, facilitating dendrite nucleation and propagation through microstructural defects.⁴⁰

In addition to the issues, the interfacial reactions induced by the thermodynamic instability between argyrodite SEs and the electrodes are also worth attention. Juergen et al.³¹ used X-ray photoelectron spectroscopy (XPS) to confirm that Li₆PS₅X will decompose at the interface due to the strong reduction of lithium. Some of the Li₆PS₅X decomposed on the surface of lithium metal to form SEI with the ingredients of decomposition products such as Li₃P, Li₂S, and LiX (Fig. 1b). The SEI leads increased in interfacial resistance and hinders the conduction of lithium ions. Further study by Wagemaker et al.³⁰ revealed that the thermodynamic decomposition reaction of argyrodite SEs with the anode side is not instantaneous. Taking argyrodite Li₆PS₅Cl as an example, it was first reduced to the unstable Li₁₁PS₅Cl, and then Li₁₁PS₅Cl was further reduced to Li₂S, LiCl, and Li₃P. In this process, the generated intermediate phases, such as S, Li₂S, and LiCl, not only produce a large volume expansion but also lead to the destabilization of the kinetics. The continued decomposition of argyrodite SEs at the interface as the cycle proceeds is the main reason for the increased interfacial resistance. In argyrodite SE and NCM interface, due to the affinity of oxygen to react with phosphorus and sulfur, phosphate (PO_x) and sulfite/sulfate (SO_x) and polysulfide (S_x) fragments are regarded as indicators for oxygen-involving degradation.⁴¹⁻⁴⁴

Narayanan et al.⁴⁵ studied how interfacial impedance changes depending on the applied current density. To analyze this behavior, they used Nyquist plots and fitted the data using an equivalent circuit model illustrated in Fig. 1c.⁴⁶ This circuit consists of a single resistor in series with three parallel circuits of a resistor and a constant-phase element (CPE) along with an additional Warburg diffusion (W_s) component. Schlenker et al.⁴⁷ attribute the inclusion of the



latter to an impedance at low frequencies arising from a lithium vacancy diffusion gradient generated most likely at the interface between the LiIn and LPSCI. In this equivalent circuit, one of the parallel circuits ($R_2||CPE_2$) in combination with the individual resistor R_1 can be assigned to the bulk and grain boundary resistance, which typically exhibits low effective capacitances (correlating to the term $Q_{CPE} \sim 10^{-6}F.s^{a-1}$, with a as the constant phase, as estimated from the CPE component of the electrochemical impedance spectroscopy (EIS) spectral data fit). The other circuit element pairs ($R_3||CPE_3$ and $R_4||CPE_4$) exhibiting relatively higher effective capacitances ($Q_{CPE} \sim 10^{-4}-10^{-2}F.s^{a-1}$) can be understood to represent the LPSCI-Li interface and charge transfer (CT) processes, respectively, as plating begins with the formation of an SEI.⁴⁶⁻⁴⁸ The variations in impedance can thus be attributed largely to the interface, which comprises the SEI and CT components represented by the spectra's low-frequency segment.⁴⁶⁻⁴⁸ The interfacial impedance (R_{int}) can then be approximated as $R_{int} = R_{SEI} + R_{CT}$ ⁴⁶, where R_{CT} is related to the intrinsic kinetics of the system.⁴⁹⁻⁵¹ Indeed, a plot of combined resistances from SEI and CT contributions (Fig. 1d) suggests that at low current densities (in this study, $J_{0.5}$ and $J_{0.05}$), the interfacial resistance asymptotically reaches a minimum. In stark contrast, for Li plating conducted at a significantly higher current density ($J_{2.5}$), the interface attains the same minimum resistance almost as soon as Li begins plating. Notably, the differences in impedance evolution are most prominent over $\sim 50 \mu Ah cm^{-2}$ of charge passed, beyond which the effect diminishes as expected, while plating proceeds to form a metallic Li layer in both cases. Thus, a rapid drop in interfacial resistance, combined with the appearance of fully reduced reaction products (Li_3P in particular) and the presence of a greater fraction of metallic Li in XPS analyses, all observed within $\sim 10 \mu Ah cm^{-2}$ of charge passed during initial stages of plating, strongly suggest the formation of a more uniform and homogeneous SEI layer as well, for Li plated at high current densities (Fig. 1e).

View Article Online
DOI: 10.1039/D5EB00101C



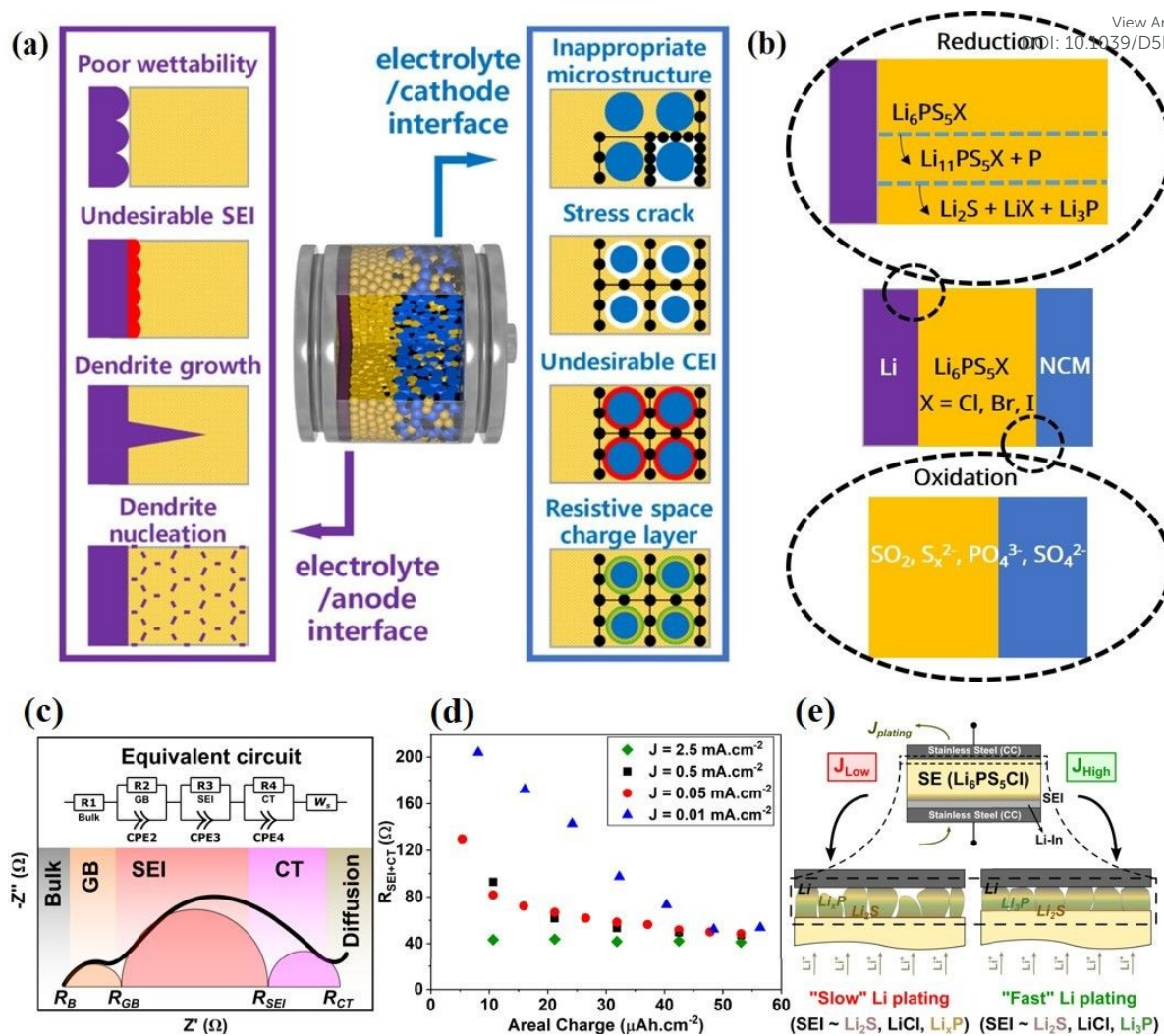


Fig. 1 (a) Challenges of SE and electrode interfaces in ASSLBs.⁵² (b) Scheme illustrating oxidation and reduction of argyrodite $\text{Li}_6\text{PS}_5\text{X}$ (X = Cl, Br, I) SEs when in contact with electrodes during cycling. Interpretation of EIS spectra. (c) Equivalent circuit used for fitting the EIS data along with a schematic describing the impedance contributions from the bulk (R_B), grain boundaries (R_{GB}), SEI (R_{SEI}) and charge transfer (R_{CT}) processes.^{46, 47} (d) Variation in interfacial resistance, R_{int} ($R_{SEI} + R_{CT}$), from fitted EIS data as a function of the amount of charge passed during Li plating at current densities, $J_{2.5} = 2.5 \text{ mA cm}^{-2}$, $J_{0.5} = 0.5 \text{ mA cm}^{-2}$, $J_{0.05} = 0.05 \text{ mA cm}^{-2}$ and $J_{0.01} = 0.01 \text{ mA cm}^{-2}$.^{46, 47} (e) Schematic representation of the likely mechanism of SEI formation and Li plating as a function of applied current density, at $J_{2.5}$ (J_{High}) and $J_{0.01}$ (J_{Low}).⁴⁵

As mentioned above, the increase in impedance at the interface between argyrodite SEs and electrodes is mainly due to interfacial reactions and the accumulation of electrically insulating byproducts.^{31, 53, 54} These reactions, particularly at the anode, result in forming an SEI and



possibly lithium dendrites, both disrupting lithium-ion movement and elevating resistance. The key mechanisms that lead to a continuous rise in impedance include:

- i. Loss of effective contact area: The SEI layer, if not well-adhered and conductive, can reduce the effective contact area between the electrode and the SE, limiting ion transport.⁵⁵
- ii. Insulating reaction products: The formation of insulating byproducts from interfacial reactions can directly block ion transport pathways, increasing the overall resistance.^{53, 54}
- iii. Dendrite growth and short circuits: As dendrites grow and penetrate the electrolyte, they create pathways for current to flow through a non-Faradaic process, significantly increasing impedance and potentially short circuits.⁵³
- iv. Grain boundary contributions: In SEs, grain boundaries may impede ion flow, particularly if they are poorly connected or contain structural defects.^{56, 57}

Furthermore, as particles within the electrode change volume during lithiation/delithiation, they can move and shift relative to each other, leading to loss of contact and increased resistance between particles.^{58, 59} This disrupts the flow of lithium ions within the electrode. Phase changes in the electrolyte, such as the formation of SEIs, can create barriers to ion transport.⁶⁰ These barriers increase the resistance within the electrolyte and impede the lithium ion transfer between the electrode and the electrolyte. Phase transitions within the electrode material, such as the shift between different lithium intercalation stages, can introduce additional resistance.^{58, 59} These phase transitions often involve structural changes that hinder the smooth diffusion of lithium ions. Therefore, these dynamic changes within the battery system create additional interfaces and hinder the efficient movement of lithium ions, resulting in increased internal resistance, SEI/CEI growth and instability, microstructure changes, capacity fading, and reduced power density.

Generally, each interface in an ASSB based on stability can be divided into one of three primary classes^{61, 62} (Fig. 2): Type I, a thermodynamically stable interface lacking a reaction driver. The interface between the solid electrolyte and the electrode is chemically stable under operating conditions, and there is no driving force (i.e., "reaction driver") that would cause undesirable chemical reactions at the interface. This means the materials at the interface are stable and cannot undergo undesirable reactions that could degrade the battery's performance or safety. Type II, reacting to generate a mixed ionic–electronic conducting interphase (MCI), a non-



passivating interphase exhibiting both ionic and electronic conductivity. An MCI can form through a reaction between the two materials in the interface between an SE and an electrode. This interphase is characterized by its ability to conduct both ions and electrons, and it is considered a non-passivating interphase. This means it does not block the flow of electrons or ions, potentially leading to undesirable side reactions and performance issues. Type III, reacting to produce stable SEI and negligible electronic conductivity, thereby preventing additional reactions. When the SE and electrode are not fully chemically or electrochemically compatible, leading to interfacial reactions that produce a new, passivating layer-the SEI. This SEI layer is a stable protective barrier that blocks electronic conductivity (acting as an insulator), and allows for Li-ion transport. By preventing electronic conductivity, the SEI stops further reactions between the electrode and SE, contributing to battery stability and longevity. Only type I (stable) and type III (passivating) interfaces can be anticipated to provide long-range stable battery performances. In type III interfaces, the σ of SEI is essential for overall battery efficiency.⁶³ Although Li-argyrodite SEs have demonstrated impressive scientific and industrial advances, difficulties still present when sulfide SEs are incorporated into ASSLBs, particularly when used with high-voltage cathodes and lithium anodes.⁶³⁻⁶⁵ In addition, the generalized concept of ASSLB cells is displayed in Fig. 3.

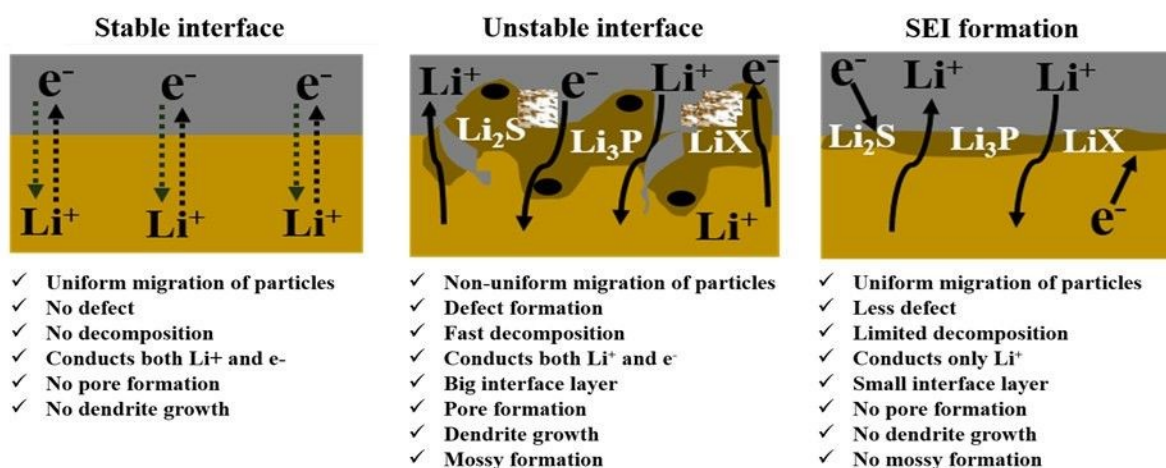


Fig. 2 Scheme illustrating the three possible types of interfaces between $\text{Li}_6\text{PS}_5\text{X}$ ($\text{X} = \text{Cl}, \text{Br}, \text{I}$) and lithium.



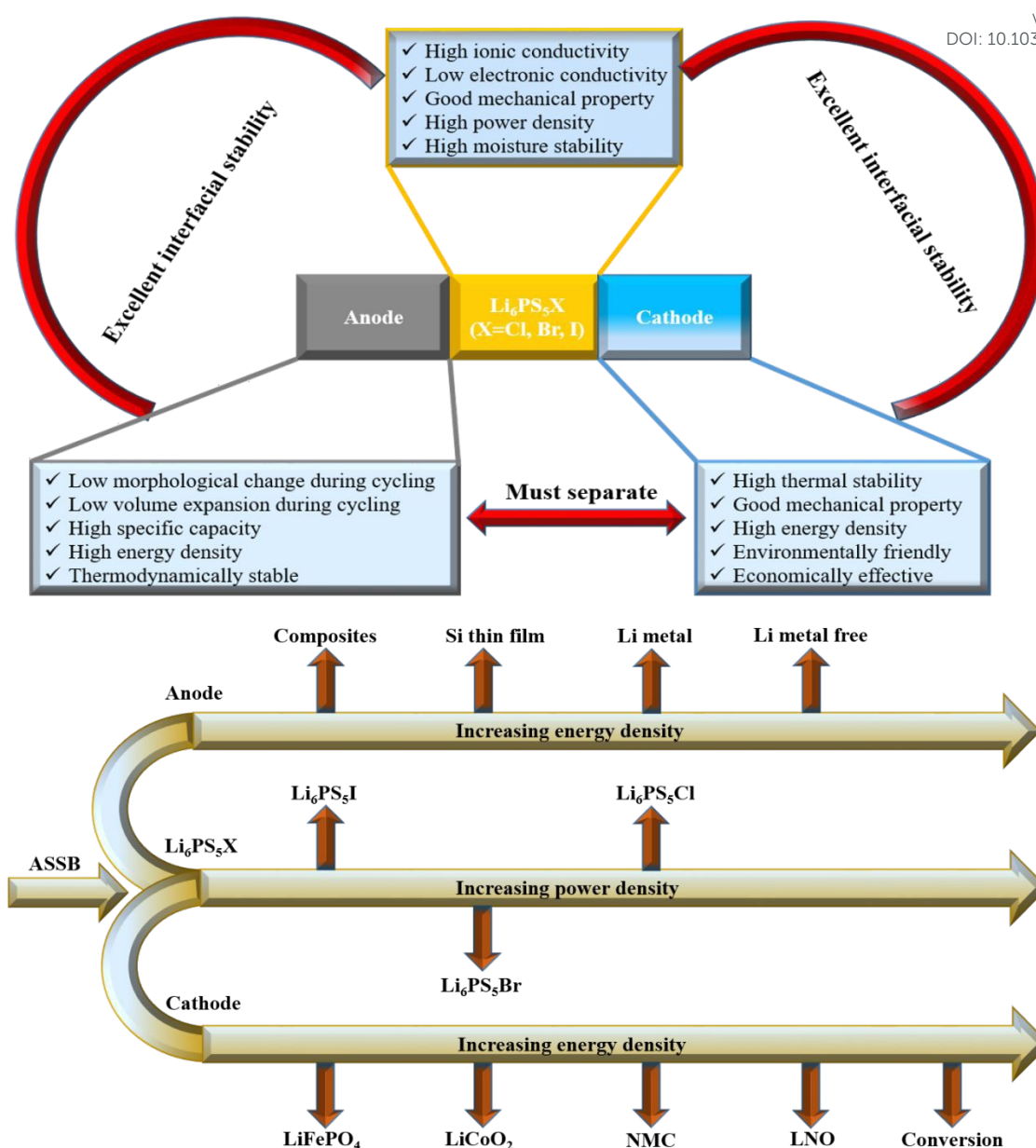


Fig. 3 The generalized concept of Li-argyrodite-based ASSLB cell.

Moreover, although SSBs perform well at room and moderate temperatures (5 °C–20 °C)⁶⁶, their performance significantly declines at low temperatures (below 0 °C) due to reduced ionic conductivity in SEs and slower solid-solid interfacial reaction rates.^{67–69} These limitations hinder overall battery efficiency, and their exact causes remain unclear.^{70, 71} To address this, Lu et al.⁷² introduced a systematic test and analysis framework, which identified the primary limiting factors at low temperatures as sluggish ion movement through the interfacial reaction layer and impaired charge transport at the degraded surface of the LCO cathode.

To explore the behavior of SSBs in low-temperature conditions, simulation methods provide crucial insights into their working mechanisms, aiding the advancement of the field. Shen et



al.⁷³ built a two-dimensional model of SSBs using multi-physics simulation software and discovered that reducing the SE thickness can enhance low-temperature rate performance. Specifically, with an electrolyte thickness of 0.6 μm , the battery retained 99.5% of its capacity even as the discharge rate increased from 3C to 8C. In interface analysis, Guan et al.⁷⁴ introduced an interfacial contact model and an electrochemical-mechanical coupling model accounting for curvature effects. They found that increasing curvature and the contact factor could delay the time to reach the cutoff voltage, thereby improving battery capacity. Additionally, Yan et al.⁷⁵ developed a 2D model incorporating electrochemical-mechanical-thermal coupling to evaluate the multiplicative charging performance of SSBs at low temperatures, considering the impact of interfacial contact degradation. Their findings indicate that both poor interfacial contact and higher charging rates contribute significantly to capacity at low temperatures.

Similarly, exposing SSEs to elevated temperatures can also influence their performance. Shin et al.⁷⁶ conducted electrochemical tests on ASSBs at around 60 °C, as the biphasic solid electrolyte exhibited insufficient ionic conductivity at room temperature, making normal battery operation difficult. Jiang et al.⁷⁷ observed that increasing the temperature from 25 °C to 65 °C significantly reduced the area-specific resistance, improving battery capacity. However, at even higher temperatures, three heat-related processes become closely interlinked. Typically, heat generation initiates the sequence that can lead to thermal failure. Over time, as the battery ages, the cumulative thermal side effects begin to negatively affect performance and compromise stability. This phenomenon is referred to as the aging effect. If heat generation surpasses the system's thermal tolerance and causes sufficient material degradation, it can eventually trigger thermal runaway.

2.1 Electrolyte-anode interface

Although much research is carried out to raise the σ of lithium SEs, electronic transport is also crucial for ASSB cycle stability, calendar life, and energy density. Only Li ions should be able to move between electrodes in an ideal SE, which would have minimal electronic conductivity and elevated σ . The outcome of electronic conduction in SEs would be the self-discharge of ASSBs driven by electronic leakage.⁷⁸ Li kinetics are ultimately hindered by the generated interfacial resistance and electronic conductivity of SEs, which also lead to performance degradation and uncontrollably growing Li dendrites.^{79, 80} Interfacial resistance hinders Li-ion kinetics in batteries by impeding the transfer of Li^+ ions across the interface between the electrode and the SE. This resistance arises from poor contact, an insulating SEI layer, and



sluggish charge transfer reactions at the interface.⁸¹ In addition, if the SE conducts electrons, electrons can leak into regions where only ions should move. These electrons react with Li⁺ in the SE, causing electrolyte decomposition.⁵² The result is the formation of resistive interphases (e.g., Li₂S, Li₃P), which block or narrow Li⁺ pathways. If the SEs have high electronic conductivity, they can provide an easy pathway for electrons to reach the Li metal anode. This allows for rapid and potentially non-uniform Li ion reduction and deposition.^{40, 82} The rapid and non-uniform deposition of Li can lead to the formation of dendritic structures on the Li metal surface.⁴⁰ These dendrites can grow and penetrate the SE, potentially leading to short circuits within the battery.^{40, 83} Dendrites can propagate along grain boundaries due to the inherent structure of the SE.⁸⁴⁻⁸⁶ As dendrites grow, they can cause mechanical stress and damage to the surrounding electrolyte, leading to crack propagation and further dendrite growth. SEs can form new phases with different ionic and electronic conductivities when decomposing. While some decomposition products might be more conductive than the original material, they are still likely to have a lower electronic conductivity compared to the ionic conductivity.⁸⁶⁻⁸⁸ The results of our group and Wang group indicated that the SE with the lowest electronic conductivity demonstrated enhanced capability to suppress lithium dendrite formation.^{40, 89}

For many years, graphite has been commonly utilized as anode material. With a specific capacity greater than 3500 mAh g⁻¹, silicon (Si) has become a viable substitute for graphite anode with a specific capacity of about 370 mAh g⁻¹. This transition aims to boost energy densities for numerous energy-storage applications, including portable electronics and electric cars.^{90, 91} Despite their potential, the commercialization of Si anode is hindered by issues related to their cycling stability and shelf life. These limitations are aggravated by the significant volumetric expansion of silicon (over 300%) during lithiation. This expansion often leads to a decline in specific capacity upon cycling, which is linked to stress formation⁹², mechanical fractures, and irreversible degradation reactions caused by the volume changes⁹³. Lithium metal is widely considered the best alternative anode material with its exceptionally high theoretical specific capacity (3,860 mAh g⁻¹) and a very low redox potential (-3.040 V versus SHE).^{94, 95} Due to this, there is considerable interest in utilizing lithium metal as an anode in ASSB configurations.⁹⁶ In the following parts, Li anode is generally referred to, although it is important to note that this analysis is also relevant to silicon and carbon anodes.

Metallic Li has been the main focus of most ASSB studies to maximize cell energy densities.^{97,}

⁹⁸ A great obstacle in improving the efficiency of ASSLMBs is the interface between SE and



electrodes. This interface is crucial for understanding battery electrochemistry, as it is the site where lithium ions and electrons interact and are deposited in the electrode through processes such as intercalation, alloying, or plating.⁹⁹⁻¹⁰⁴ The interface is often complicated by the existence of the passivation layers on the electrode. The characterization of this layer on negative electrodes started with Dey's findings of Li metal immersed in non-aqueous electrolytes.⁹⁹ In 1979, Peled announced the idea of the SEI as a passivation layer that is electronically insulating and ionically conductive, emerged between the electrode and electrolyte, and functioning as an SE.¹⁰⁰ Thus, it is called the SEI. This model was further enhanced with compositional information observed over two decades and summarized by Peled et al.¹⁰¹ in 1997 and Aurbach et al.¹⁰² in 1999. On one hand, a dense and undamaged SEI can hinder electron passage, thereby preventing further degradation of the SE, which is essential for the chemical and electrochemical stability of ASSB. Conversely, the emergence and development of SEI consume active Li and SE, leading to capacity loss, rising battery resistance, and reduced power density.¹⁰⁵ Meanwhile, the uneven SEI may cause Li dendrite growth and safety concerns upon charging.

The composition and growth rate of the SEI layer between lithium metal and argyrodite-type solid electrolytes (e.g., $\text{Li}_6\text{PS}_5\text{X}$, where $\text{X} = \text{Cl}, \text{Br}, \text{I}$) can vary significantly, impacting interfacial resistance and overall battery performance.^{31, 106} When lithium metal contacts argyrodite electrolytes, a chemical reaction occurs, leading to the formation of an SEI composed of Li_3P , Li_2S , and LiX . The rate at which interfacial resistance increases can differ among various argyrodite compositions. For example, $\text{Li}_6\text{PS}_5\text{Cl}$ forms a protective interphase consisting of Li_3P , Li_2S , and LiCl when in contact with lithium metal. In contrast, $\text{Li}_6\text{PS}_5\text{I}$ exhibits a more reactive behavior, resulting in a different SEI composition and potentially higher interfacial resistance.^{12, 31, 106, 107}

In general, the composition of the SEI layer and the rate at which interfacial resistance increases between lithium metal and argyrodite electrolytes are influenced by several factors, including the specific halide component of the argyrodite, the growth mechanism of the SEI, and the condition of the lithium anode surface. Understanding these variables is crucial for optimizing the performance and longevity of solid-state batteries utilizing lithium metal anodes.

Thus, there are still plenty of challenges to overcome before Li metal anodes can be used in ASSLMBs: (1) unmanageable lithium dendrite development due to electrochemical and mechanical instability at the SE/Li interface causes serious safety issues¹⁰⁸; (2) the



thermodynamic instability of lithium metal because of its high Fermi energy level can result in irreversible and continuous reaction between lithium and SE that produce thick solid SEI layer on the lithium metal surface, consume lithium and SE, and elevate the internal resistance, thus shorten cycling span; and (3) repeated plating and stripping operations can cause significant volumetric and morphological alterations in the lithium metal anode; however, the mentioned earlier SEI coatings are very thin to inhibit such substantial alterations in the lithium metal anode completely.¹⁰⁹⁻¹¹³ These adverse effects may result in significant safety risks and a loss of efficiency. These harmful effects might be mitigated by SEs that are chemically stable towards lithium anode. Nevertheless, several unanswered questions remain about the kinetics and nature of ion transports at Li/SE interfaces. To realize energy-dense ASSLBs, Li metal morphology must be controlled during stripping/plating processes at the Li/SE interface.^{46, 114, 115}

At low potential, $\text{Li}_6\text{PS}_5\text{Cl}$ undergoes a reduction of P (approximately 1.08 V vs. Li/Li^+) during lithiation, resulting in the byproducts Li_2S , LiCl , and P (Fig. 4a), which renders it unstable towards lithium anode.²⁸⁻³⁰ $\text{Li}_6\text{PS}_5\text{Cl}$ also produces Li_2S , LiCl , and Li_3P as byproducts when in contact with the lithium anode (chemical decomposition).³¹

Narayanan et al. studied the development of SEI during virtual electrode plating at $\text{Li}_6\text{PS}_5\text{Cl}$ surface via XPS measurement.⁴⁵ At the left panel of Fig. 4c, the Li 1s spectra at 30 μA electron beam current (EBC) with $j_{eq} \approx 0.15 \text{ mA cm}^{-2}$ initially show the peak widening and then a gradual shift to lower binding energies. The observed peak broadening can be directly linked to the creation of Li_2S , Li_xP , LiCl , and other byproducts from contaminants such as Li_2O and Li_2CO_3 .^{31, 116} In addition, the authors determined that Li deposits more rapidly at greater current densities compared to lower ones (Fig. 4d). As shown in Fig. 4e, for the S 2p signal, a doublet feature associated with Li_2S (with a $2p_{3/2}$ binding energy around 160 eV, highlighted in brown in Fig. 4e) quickly emerges as more lithium is plated. This component of the Li– $\text{Li}_6\text{PS}_5\text{Cl}$ SEI is well-documented and forms even in conditions where Li is deficient.^{31, 116, 117} A close analysis of the constitution from spectra collected at various EBC (Fig. 4f), reveals that the reduction of $\text{Li}_6\text{PS}_5\text{Cl}$ to Li_2S occurs significantly faster via 0.15 mA cm^{-2} (greater CD). In contrast, at lower current densities ($j_{eq} \leq 0.05 \text{ mA cm}^{-2}$), only about 70% of the S 2p spectrum consists of the reduced sulfide families. This suggests that reaction kinetics are slower at low CDs due to multiple reduction reactions competing for the available reactants, such as plated lithium. Furthermore, analyzing the P 2p spectra shows that at the highest current density (j_{eq}), for equivalent charges passed less than $5 \mu\text{Ah cm}^{-2}$, there is a rapid reduction to a low binding



energy doublet feature ($2p_{3/2} \approx 126$ eV), indicative of fully reduced Li_3P (Fig. 4g, left panel, green area). In comparison, at lower current densities ($j_{\text{eq}} \leq 0.05 \text{ mA cm}^{-2}$) and the same extent of charge, the initial SEI consists more notably of a broad spectral feature ($126 \text{ eV} < \text{B.E. } 2p_{3/2} < 131 \text{ eV}$), which is indicative of partly reduced Li_xP . Over time, continued plating at these lower current densities also leads to the formation of Li_3P . However, this process is slower and followed by a notable reduction in the total P 2p spectral intensity, indicating a deposition of plated lithium metal. These findings indicate that a Li_3P -rich SEI forms more quickly in the early stages of plating via large CDs, even with a low equivalent charge passed. The fragment of Li_3P as a function of equivalent charge passed, especially for $q_A < 10 \mu\text{Ah cm}^{-2}$ (Fig. 4h), supports this observation. Additionally, as seen in Fig. 4e and 4g, the XPS signal for pristine $\text{Li}_6\text{PS}_5\text{Cl}$ components diminishes more rapidly at high current densities for the same equivalent charges passed (e.g., $q_A = 12.8 \mu\text{Ah cm}^{-2}$).

In our group's studies, we noted that the Li (1s) spectra at the Li/ $\text{Li}_6\text{PS}_5\text{Cl}$ interface after cycling revealed the emergence of LiCl. Furthermore, the S(2p) spectra of $\text{Li}_6\text{PS}_5\text{Cl}$ after cycling showed an increase in the signal intensity for polysulfide, P_2S_n , accompanied by decomposition products, including lithium polysulfide (Li_2S_n) and Li_2S , resulting from the sulfide decomposition.⁸⁹ According to Zeier's group, $\text{Li}_6\text{PS}_5\text{X}$ disintegrates into an interphase made of Li_3P , Li_2S , and LiX when it comes into contact with Li metal.³¹ This interphase acts as an SEI and raises the interfacial resistance. For instance, according to this group, after contact with Li metal, $\text{Li}_6\text{PS}_5\text{Cl}$ decomposes into Li_2S , Li_3P , and Li_2O (Fig. 4i). The degradation of SEs is prompted by increased interfacial resistance.



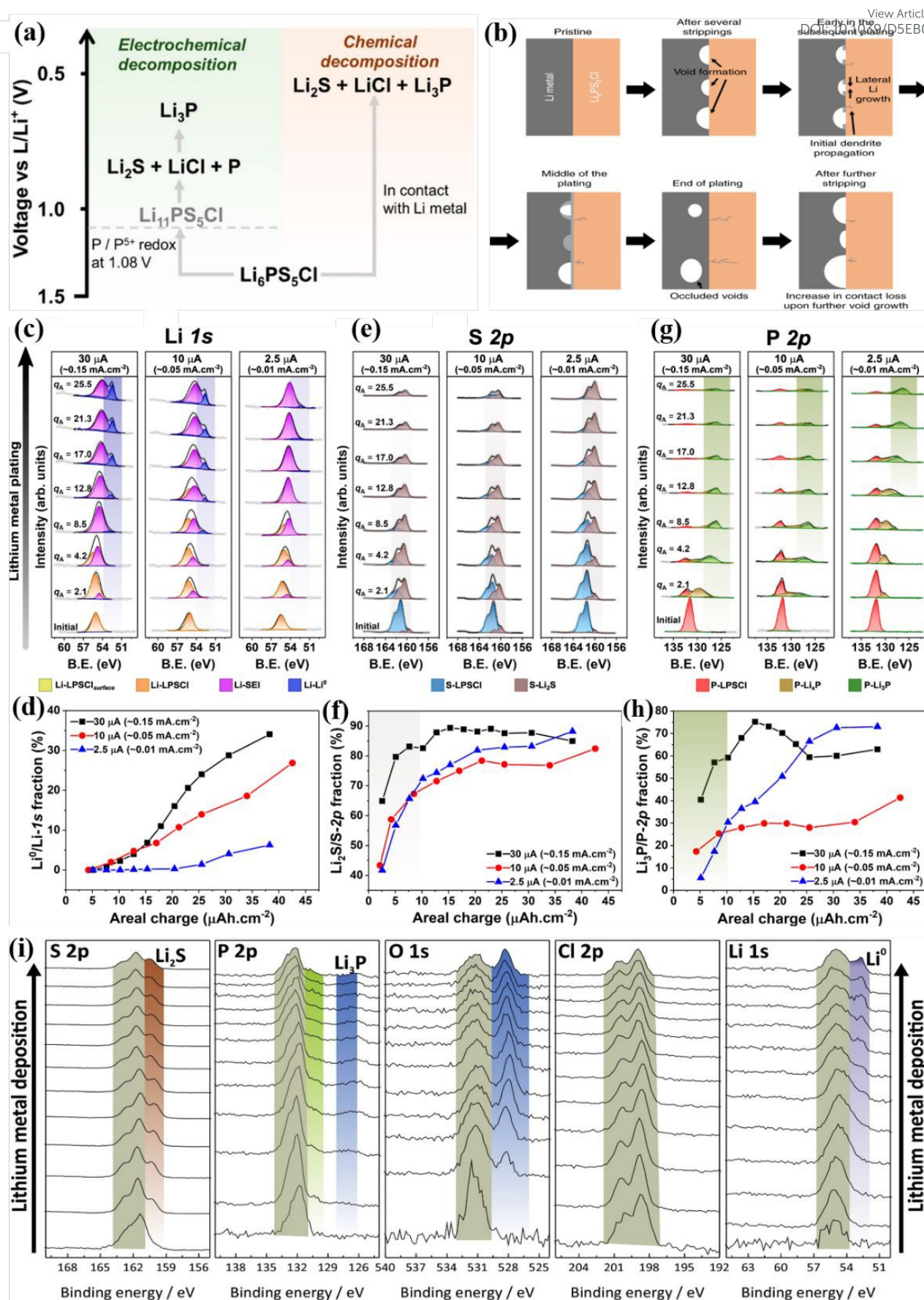


Fig. 4 Decomposition pathway and XPS analysis. (a) Electrochemical/chemical degradation pathway of $\text{Li}_6\text{PS}_5\text{Cl}$.¹¹⁸ (b) The diagram illustrates the emergence of voids at the Li/Li-argyrodite SE interfaces.⁴⁶ Progression of core-level XPS spectra during the virtual electrode plating process at the $\text{Li}_6\text{PS}_5\text{Cl}$ surface for (c) Li 1s, (e) S 2p and (g) P 2p. Quantification of XPS spectra as a function of different quantities of charge passed at various CDs, showing compositional fractions of (d) metallic Li (Li^0) in Li1s, (f) Li_2S in S2p, and (h) Li_3P in P2p. A higher fragment of Li^0 (shown in panel d) and Li_3P (indicated by green area in panel h) at low charge levels and elevated CDs suggests that the reaction kinetics at the interface are more rapid, leading to a more immediate emergence and development of a metallic Li layer during plating.⁴⁵ (i) XPS spectra for S 2p, P 2p, O 1s, and Cl 2p of a $\text{Li}_6\text{PS}_5\text{Cl}$ SE as the quantity of accumulated Li metal rises (progressing from bottom to top).³¹

Another issue at the Li/Li argyrodites interface is the growth of Li dendrites.¹¹⁹⁻¹²² Lithium dendrite is broadly seen in various types of SEs.¹²³ Dendrites typically expand in the direction of grain boundaries. Sulfide SEs exhibit apparent dendrites because of a weaker adhesion between sulfide particles, which results in a lower resistance to dendrite formation than in oxide SEs.⁵⁰ The irregular lithium deposition at the anodic interface allows lithium dendrite to pass through the grain boundaries or voids within the bulk of Li argyrodite SEs, inducing battery degradation. Kasemchainan et al. recently showed that the critical current density (CCD) is essential for the lithium plating/stripping characteristics utilizing $\text{Li}_6\text{PS}_5\text{Cl}$ SEs.⁴⁶ As seen in Fig. 4b, voids develop with lithium bulk around the interface with the SE when lithium is withdrawn from the interface at a CD that exceeds the rate of replenishment. These voids accumulate over the course of subsequent cycling. The margins of these voids concentrate greater CD than other areas, eventually causing the formation of Li dendrite.

The quantity of the CCD is crucial as it determines the power density of a cell. Small CCDs are typically attributed to uneven potential drops caused by SE/electrode interfacial impedance. This impedance is predominantly determined by chemical, electrochemical, and mechanical stability issues at the interface. Understanding these uneven loss mechanisms and interpreting CCD tests can be difficult since SEs may experience “soft shorts” that remain unnoticed in symmetric cell tests using thick Li metal (greater than 30 μm).¹¹⁵ Moreover, as the CCD depends on plating capacity and cell stack pressure, precise data interpretation requires the reporting of specific experimental conditions (such as Li-metal thickness and stack pressure).¹¹⁴



Critical stack pressure is a recently developed concept by Sakamoto and colleagues that emphasizes pressure dependence in CCD measurements.¹¹⁴ This measure is a crucial addition to the other metrics used to assess the characteristics of Li electrodes at SE interfaces. Dendrite nucleation may originate from pore formation in lithium metal during stripping and unequal lithium ion transport at Li/SE interface.¹²⁴⁻¹²⁶ A minimal stack pressure can help prevent pore evolution during Li stripping. Nonetheless, Li plating causes Li filament development and propagation. In Li-Li cells, when these happen at the same time, the pressure will have a big impact on the CCD. Nevertheless, it remains uncertain how these effects will manifest in full cells, where plating and stripping operate independently. More investigation is required to reconcile discrepancies between full-cell and symmetric measurements.

Currently, ASSLMB's performance is still far from its targets. In general, CCD is a crucial criterion for assessing ASSLMBs. It offers opportunities to fully comprehend failure processes, interfacial behaviors, and other electrochemical performance features.⁵⁰ The performance of Li/Li symmetric cell configurations utilizing Li-argyrodite SEs is summarized in Table 1. Apart from SE characteristics, the mechanical characteristics of the Li metal also play a significant role in the existence of lithium filament within SEs. Recent investigations on the bulk mechanical behavior of lithium metal have shown that power-law creep is the predominant deformation mechanism over a broad range of strain rates and temperatures.^{127, 128} These findings provide a viscous-flow perspective that helps explain how mechanical stresses change as lithium plating taking place on SE surface.

The linked interactions between CD and strain rate directly affect stress build-up at the solid-solid interface. This has considerable indications for the model of Porz et al.,¹²⁹ where the ejection of lithium metal from the heterogeneous surface of the SEs contributes to the CD-dependent mechanical failure of the SEs.

For the lithium metal anode to work in a reliable, reversible, and safe manner, we must resolve any problems driven by the inherent morphological instability while plating and stripping Li metal at the SE interface^{49, 130}. Recent work has significantly advanced our understanding of both dendrite emergence and development and pore formation during stripping, as shown in Fig. 5a and 5b, respectively.^{131, 132} However, many of these studies operate under excessively high stack pressures, while the ideal pressure should be below 0.1 MPa to align with the stack pressures typical of lithium-ion batteries.



The CCD in solid batteries is influenced by numerous internal and external factors, many of which are interrelated. Due to poor interfacial compatibility in solid-state systems, CCD is more sensitive to external influences than systems using LEs. The major issues are summarized in Fig. 5c. Establishing good physical contact is one of the most essential requirements for SSBs.¹³³ The interfacial contacts are directly related to the interfacial physical contacts and chemical stability. In SSBs, where liquid components are absent, Li-ion pathways rely solely on solid–solid contact.¹³⁴ Additionally, reactions between Li metal and SEs can cause volume changes and generate interfacial byproducts, further altering interfacial contact.¹³⁵

The intrinsic characteristics of SEs, such as relative and compacted densities, chemical composition, and mechanical strength, also significantly influence CCD.¹³⁶ Most SEs are polycrystalline, comprising multiple single crystals, grain boundaries, isolated particles, impurities, and inherent flaws. These structural features impact internal ionic flux and provide sites for Li filament nucleation and propagation. In ASSB systems, increasing the areal capacity during Li stripping leads to significant contact loss. As reported, 1 mAh cm⁻² corresponds to a Li thickness of 4.9 μm.¹³⁷ For commercial viability, areal capacities above 4 mAh cm⁻² are needed, which could create void layers nearly 20 μm thick upon full discharge, severely impacting interfacial contact and performance, especially at high current densities.¹³⁸ Additionally, large-scale Li cycling causes substantial volume expansion and worsening contact degradation. According to the terrace-ledge-kink model, losing active plating/stripping sites is difficult to recover due to the sluggish and uncontrollable surficial Li adatom diffusion according to the terrace-ledge-kink model. The Li growth exhibits a complexity highly related to initial morphology and the current density, leading to poor CCD.

SSBs must also operate reliably across wide temperature ranges in real-world applications. Temperature affects CCD by altering both lithium's physical properties and electrochemical behaviors, such as ionic conductivity and diffusion at the interface. Elevated temperatures improve CCD by enhancing Li⁺ mobility. In liquid systems, high current dendrite formation is often explained using diffusion-limited models; similar models are now applied to solid-state systems. According to Sharafi et al., higher CCD reflects a higher Li⁺ flux across interface regions.¹³⁹

Pressure is another key external factor influencing CCD. Lithium metal's mechanical properties, such as elasticity, plasticity, and creep behavior, allow it to deform under applied



stress. Li shows pronounced creep at higher temperatures, especially under operational stress levels. Accurately predicting lithium's deformation behavior is essential to enabling its use in SSBs. Masias et al. systematically measured the Young's modulus, shear modulus, time-dependent deformation (creep), and stress-dependent deformation.¹²⁸ The elastic and plastic properties are directly related to the solid–solid contacts. The deformed Li gradually flows to the side boundary of batteries without a hydrostatic pressure, increasing the risk of short circuits. The pre-stressed system constrains the undesirable flow of Li metal. The deformation of Li metal also induces microstructural evolutions, significantly reducing interfacial troubles and enhancing the CCD values. Pre-pressing Li also minimizes creep-induced shorting.¹²⁸ Li metal is softer than most inorganic solid-state electrolytes in Li metal-based SSBs. The deformation of Li metal dominates the deformation-dependent impedance reduction. Thus, increasing pressure helps expand the true contact area at the interface and stabilize battery performance.

View Article Online
DOI: 10.1039/D5EB00101C



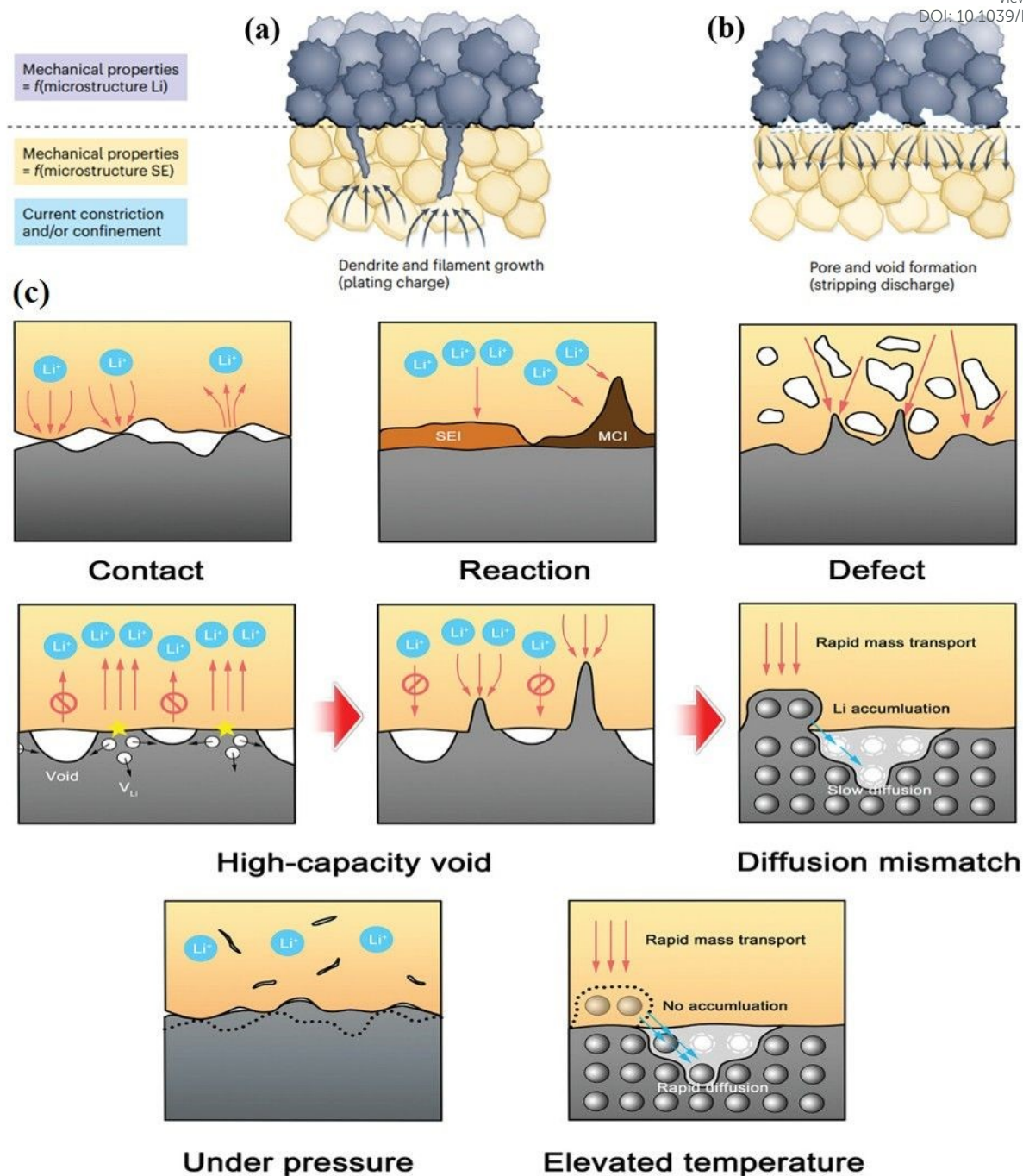


Fig. 5 Crucial concerns with the lithium metal anode. (a) Filament and dendrite development. (b) Pore and void development.¹⁴⁰ (c) Scheme illustrating the main factors affecting CCD.⁵⁰

The loss of electrode-electrolyte contact primarily stems from the accumulation of vacancies at the interface and the volume changes occurring during the continuous stripping of lithium metal.¹⁴¹ During the process of lithium stripping, the release of lithium atoms creates vacancy sites, contributing to vacancy accumulation. This accumulation results in the formation of pores and flaws at the operational interfaces. Over time, these flaws diminish the efficient interfacial

areas, leading to a partially concentrated flux of lithium ions (Fig. 6g). Moreover, this concentrated lithium ion flux exacerbates the contact loss further.

Kazyak et al. investigated that at elevated current densities and areal capacities, there is an uneven depletion of lithium and accumulation of voids.¹³⁸ It has been demonstrated that the interfacial capacitances primarily stem from these voids at the interface. Microelectrodes were utilized to visualize void accumulation (Fig. 6a). Clear areas of lithium depletion were detected following lithium stripping at 1.07 and 1.47 mAh cm⁻² (Figs. 6b and 6c). These depleted regions signify areas of contact loss, resulting in increased polarization (Fig. 6d) and interfacial impedance (Fig. 6e). Additionally, during lithium plating, significant volume expansion leads to the formation of more cracks, thereby accelerating lithium pulverization.¹⁴²

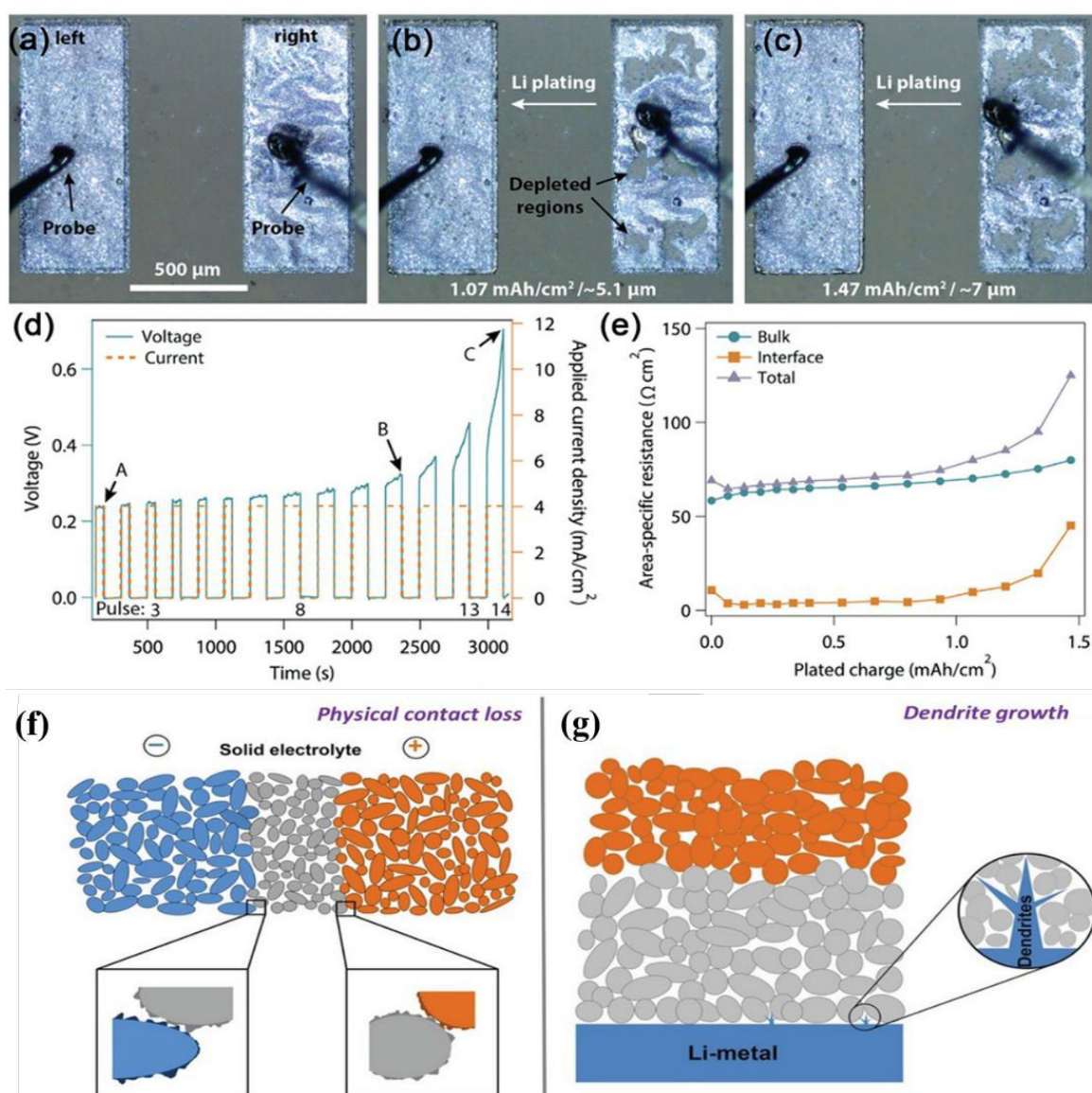


Fig. 6 Contact loss at the anode in ASSLMBs. (a) Microelectrodes arrangement for experimental use. Depletion regions of (b) 1.07 mAh cm^{-2} stripping and (c) 1.47 mAh cm^{-2} . (d) Increase in polarization following contact losses. (e) Rise of impedance with continuous stripping.¹³⁸ Schematic illustrations demonstrate physical contact losses in ASSBs (f) and dendrite evolution within ASSLMBs (g).¹⁴¹

Moreover, inadequate contacts present a significant difficulty to ASSBs and can stem from both physical and chemical factors. Contact loss typically manifests during battery fabrication and exacerbates over-cycling. Therefore, the electrochemically active contact area between the active materials and SE is a critical parameter in ASSBs.⁸⁷ In the case of active materials in LIB electrodes, most of the surface area of active materials is fully contacted with the LE except for the area covered by the electric conductor and polymeric binder; hence, it can be considered as an electrochemically active contact area. However, the surface of active materials is not sufficiently covered with SEs due to its original shape and mechanical stiffness. Therefore, the real specific contact area ($a_s = A_c/V_a$)^{143, 144}, which is defined as the contact area (A_c) between the active material and SE divided by the bulk volume (V_a) of the active material, is considered an important parameter to improve the design of ASSBs. An adequate a_s is typically on the order of $a_s \geq 10^5 \text{ cm}^2/\text{cm}^3$. For example, a high-performance ASSB using a sulfide SE with nano-engineered composite cathodes might achieve $a_s \approx 10^6 - 10^7 \text{ cm}^2/\text{cm}^3$. This corresponds to well-distributed and conformal contact between electrolyte particles and active material.⁸⁷ Physical contact issues predominantly affect bulk-type ASSBs (Fig. 6f). Achieving atomic-scale and conformal contact is paramount for optimal performance. However, attaining these perfect contacts in practice is challenging due to particle-particle contact and the presence of pores.¹⁴¹

Recent research by Kasemchainan et al.⁴⁶ revealed that the buildup of voids at the Li/Li₆PS₅Cl (LPSCI) interface during continual plating/stripping processes triggers the evolution of Li-dendrite. After multiple cycles of stripping and plating, voids were observed at the LPSCI-Li interface compared to the pristine interface. The formation of interfacial voids may result when Li filaments are removed more quickly than they can be replenished. Li-dendrite initiations begin at the triple junction where lithium metal, voids, and SE coexist, eventually leading to short circuits and failure in ASSBs. Additionally, pre-existing flaws and cracks can serve as pathways for the development and spreading of Li-dendrites through the SEs.¹⁴⁵ Understanding how micro-cracks influence Li-dendrite propagation through SEs is crucial, necessitating in-



situ operando prediction of microstructural alteration, particularly in micro-crack formation during battery cycling.¹⁴⁵

Table 1. Li/Li symmetric cells performance utilizing Li-argyrodite electrolytes.

Cell configuration	Critical density (mA cm ⁻²)	current	Cut-off capacity (mAh cm ⁻²)	Test temperature (°C)	Ref.
Li _{6.3} P _{0.9} Cu _{0.1} S _{4.9} Cl _{1.1}	3.0		3.0	50	89
Li _{6.25} PS _{4.75} ClN _{0.25}	1.52		1.52	RT	146
Li ₆ PS ₅ Cl _{0.3} F _{0.7}	6.37		5.0	RT	79
Li ₆ PS ₅ Cl	0.55		0.55	RT	147
Li ₆ PS _{4.7} O _{0.3} Br	0.90		0.90	RT	148
Li ₆ PS ₅ Br	0.45		-	RT	148
Li _{6.05} P _{0.95} Mo _{0.05} S _{4.9} O _{0.1} Cl	0.55		-	RT	149
Li _{6.04} P _{0.98} Bi _{0.02} S _{4.97} O _{0.03} Cl	1.1		0.1	RT	150

RT: Room temperature.

2.2. Electrolyte-cathode interface

In contrast to metallic anodes, cathode components consist of active material (AM) particles like LiCoO₂ (LCO), LiMn₂O₄, LiNiMnCoO₂, LiNiCoAlO₂, and LiFePO₄. These particles combine with a suitable SE (ionic conductor), carbon (electron conductor), and/or binder to improve ion and electron transportation. In an LE battery, the LE fills the voids between cathode components and provides intimate contact with the electrodes. On the contrary, solid-solid interfaces in ASSBs rely on physical contact. To analyze the impacts of interfaces, Luntz et al.¹⁵¹ utilized a symmetrical cell to assess the internal resistance (IR) drop at both cathode/SE and anode/SE interfaces. Figs. 7a–7b presents the evaluation method and findings. In their experimental work, an Au/SE/Au configuration was used as the reference for IR drop measurement. A negligible IR drop was observed when using a Li/SE/Li configuration, indicating interface resistance between Li and SE. However, combining SE with carbon electrodes (Figs. 7c and 7d) led to a significantly higher IR drop compared to Li, showing greater interfacial resistances. The IR drop at the Li/SE interface was ascribed to SEI generation and inadequate contact. In contrast, the electrochemical processes at the carbon-electrolyte



interface are more complex. Although their findings highlight the distinct contributions of interface resistance at both electrodes, they focused solely on carbon electrodes when concluding that the greatest interfacial resistance happens at the carbon/SE interfaces.

When two materials with differing Fermi levels come into contact, electrons will flow from the material with higher Fermi energy to the one with lower Fermi energy until equilibrium is reached. This electron transfer causes band bending at the interface, forming space charge regions and potential barriers that can impede charge carrier movement.

When gold (Au) and a SE come into contact, their Fermi levels (E_F), representing the chemical potential for electrons, are typically not aligned initially. The electrons flow from one to the other and lead to electronic leakage, causing decomposition. This impacts charge transfer and interfacial stability.

In the case of carbon and SEs, the Fermi level of carbon may align differently with the conduction band of the SE. This misalignment can influence the charge transfer kinetics and the stability of the interface, potentially leading to issues such as interfacial resistance or degradation over time.

From a physical point of view, one may relate the cell voltage to the difference of the (electro-)chemical potential of the electrons between the cathode and anode as given by the position of their Fermi levels (see Fig. 7e). Note, however, that the chemical potential difference of lithium between anode and cathode may be expressed as the sum of the chemical potential difference for both electrons ($\Delta\mu_{e^-}$) and the lithium ions ($\Delta\mu_{Li^+}$), Eq. 1:^{152, 153}

$$-eV_{OC} = \Delta\mu_{e^-} + \Delta\mu_{Li^+} \quad (1)$$

Therefore, considerations restricted to the Fermi level (electron chemical potential) of (single) electrode materials in discussing electrode potentials are approximate, albeit often resulting in reasonable accuracy.

Besides the active (intercalation) material, commercial Li-ion electrodes consist of polymer binder and conductive additives, forming complex, often nano-sized, 2-D or 3D composites. The performance of these composite electrodes is highly dependent on the distribution, ratio, and type of the different constituents.^{154, 155} From an idealized point of view, the voltage and capacity of Li-ion batteries are only determined by the thermodynamic bulk properties of the active phases. However, contact potentials and kinetic effects in real batteries strongly influence the practically achieved voltages, capacities, and current densities. As a consequence,



all practical performance data (e.g., energy and power density, lifetime) are influenced by kinetic factors, which are often dominated by interface effects and continually evolve with time due to side reactions and other degradation phenomena.¹⁵⁶

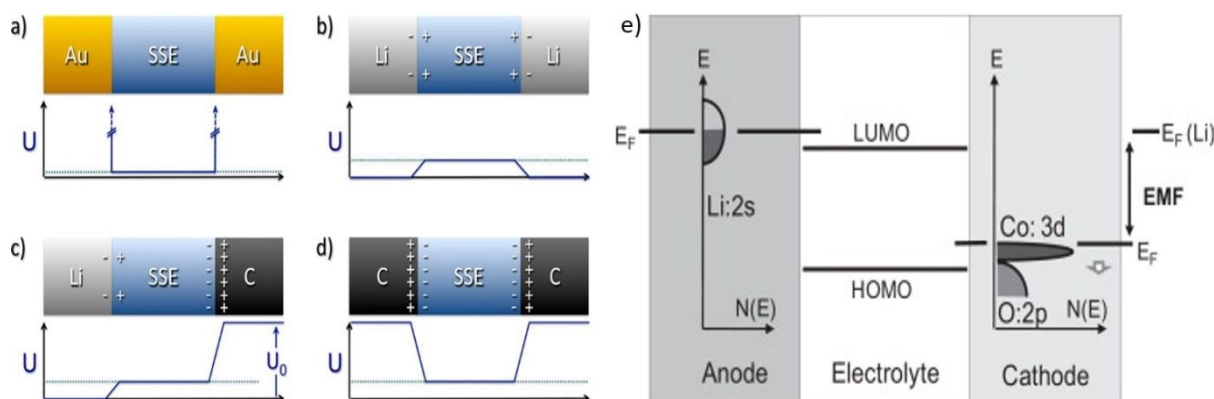


Fig. 7 Common cathode/SE interfaces in ASSBs. (a) Au/SE/Au. (b) Li/SE/Li. (c) Li/SE/C. (d) C/SE/C.¹⁵¹ Potential variation (U), carbon (C). (e) A schematic energy level diagram of a Li cell using LiCoO₂ as the cathode and Li metal as the anode shows how the electromotive force (EMF) originates. In this diagram, the Fermi level of the lithium anode lies above the electrolyte's LUMO, which explains the typical reduction of the electrolyte upon contact with Li. Additionally, during Li deintercalation from the cathode, the Fermi level of LiCoO₂ shifts downward, as indicated by a small arrow in the diagram.¹⁵⁷

Nowadays, layered LiMO₂ materials (M = Ni, Co, Mn) are widely recognized as standard cathode active materials (CAMs) for high-energy-density battery. Particularly, LiNi_aCo_bMn_cO₂ ($a + b + c = 1$; NCM-abc) and LiNi_xCo_yAl_{1-x-y}O₂ (NCA) are capable of achieving higher voltages and higher volumetric specific energy. As a result, they have established themselves as primary CAMs in electric vehicle applications.

For instance, Ni-rich NCM cathodes, such as LiNi_{0.8}Mn_{0.1}Co_{0.1}O₂ (NCM811), are highly attractive due to their competitive capacity and energy density compared to advanced LIBs.¹⁵⁸⁻

¹⁶¹ However, integrating sulfide-based ASSLMBs with Ni-rich oxide cathodes faces significant difficulties: 1) sulfide SE degradation occurs at high voltages due to their restricted ESW; 2) undesirable interfacial reaction between sulfide SEs and NCM811 results in the existence of ionic-insulating degradation products; 3) an SCL forms between sulfide SEs and oxide cathode materials because of mismatched chemical potentials, leading to a high-resistant lithium depletion layers at the sulfide SE side; 4) structural deterioration at the surface and grain



boundaries of Ni-rich oxide cathode particles leads to capacity and voltage decay issues.^{52,162} Article Online
DOI: 10.1039/D5EB00101C

¹⁶⁵ Although raising the upper cutoff voltage can enhance the capacity of Ni-rich NCM811 cathode materials, it also risks material degradation due to issues such as cracking and oxygen loss. Grasping these degradation mechanisms is essential for facilitating high-voltage operation and enhancing the capacity of advanced materials.^{166, 167} Recently, studies have focused on single-crystal (SC) NCM-based cathodes for ASSLBs. These materials typically have a lower nickel content to reduce volume changes during cycling, although this approach does come with the trade-off of decreased discharge capacity.¹⁶⁸⁻¹⁷⁰

Chemical decomposition of an SE can lead to contact loss between the cathode and SE due to the volume decrease associated with the chemical reaction, which can cause physical separation or cracking.^{25, 171, 172} The decomposition process can form new interphase layers or degrade the existing ones, hindering the ionic conductivity and leading to resistance increases. In addition, chemical and mechanical degradation at the solid electrolyte/cathode interface can interact synergistically, accelerating performance decline in solid-state batteries.¹⁷³⁻¹⁷⁵ Chemical degradation, such as the formation of resistive reaction layers or the dissolution of cathode materials, can induce mechanical stresses at the interface, leading to cracking or delamination. Conversely, mechanical stress from cathode expansion/contraction during cycling can accelerate chemical degradation by exposing fresh reaction sites. This can lead to capacity loss, reduced rate capabilities, and a general decline in battery performance.

From a microstructural perspective, lattice mismatches present physical contact challenges. Such interfaces often arise around the contact area of solid materials with differing lattice parameters. This mismatch can happen around electrode/SE interfaces, inducing strain and the existence of super-lattices, consequently elevating interfacial resistance.¹⁴¹ In contrast, interfaces between materials with minimal lattice differences exhibit substantially lower interfacial resistances and higher σ compared to those with significant lattice deviations. It's important to note that lithium-ion transport throughout all ASSBs is also affected by interface impedance and bulk σ . Indeed, weak Li^+ transport may also manifest at lattice-matched interface with inadequate bulk σ .

Theoretical calculations help elucidate the electronic/atomic distributions around lattice mismatched interfaces. Utilizing DFT calculation, Jand and Kaghazchi investigated LiCoO_2/SE interface structures.¹⁷⁶ This investigation can be done by varying the biaxial compressive and tensile strain magnitude. Their simulations identified three energetically



favorable interfaces. Analysis of all three models revealed atomic rearrangements and big strain at the interface due to lattice mismatch. While this model does not include ab initio molecular dynamics, it showcases the successful application of DFT methods in simulating and predicting interfacial characteristics in ASSBs. Nevertheless, predicting interfacial behavior in ASSBs remains complex. Therefore, a sophisticated computational technique employing an intelligent algorithm is necessary to find energetically favorable interface structures. This provides a comprehensive understanding of lattice-mismatch mechanisms.

Recently, Gao et al. introduced an estimation method to understand lattice-mismatched structures around interfaces using the particle swarm optimization (CALYPSO) method.¹⁷⁷ This approach considered both lateral and vertical displacements. By combining the CALYPSO approach and DFT calculations, they identified 6 kinds of $\text{LiCoO}_2/\text{Li}_3\text{PS}_4$ interface structures, as illustrated in Fig. 8. Simulation results highlighted the existence of highly energetically favorable interfaces, such as cobalt sulfide and phosphorus oxide. Here, cation (cobalt/phosphorus) and anion (sulfur/oxygen) inter-diffusion occur around interfaces. Those theoretical findings align well with experimental observations.¹⁷⁸ A viable strategy to alleviate lattice variations is by employing materials with greater structural resemblance for both electrodes and SEs.

Generally, when a sulfide SE comes into contact with layered oxide cathode materials with a low lithium ion chemical potential (μLi) vs. S^{2-}/S , the sulfide SEs undergo oxidation even under open circuit voltage (OCV) conditions. This oxidation process contributes to the degradation of both the SEs and the CAMs, leading to structural damage.

Even though ASSBs have gained significant attention owing to their potential increased energy density and high safety, the thermal runaway of batteries cannot be mitigated just by utilizing nonflammable SEs. The interface between the cathode material and the electrolyte is a critical area for safety concerns.¹⁷⁹⁻¹⁸² Safety issues in solid-state batteries, particularly with argyrodite SE and layered cathode materials, are often linked to interfacial phenomena like SO_2 gas formation during exothermic reactions.¹⁸³ These reactions can lead to heat buildup, decomposition of the SEI, and ultimately, thermal runaway. Safety hazards with exothermic behaviors and combustion phenomena were demonstrated between sulfide SEs (glassy-ceramic and crystalline types) and the fully delithiated Ni-rich ($\text{LiNi}_{0.8}\text{Co}_{0.1}\text{Mn}_{0.1}\text{O}_2$, NCM) layer cathode. The heat generation of sulfide SEs + NCM was 900% larger than that of LE + NCM.¹⁸³ The interaction between the cathode and electrolyte can also reduce the decomposition



temperature and exacerbate safety concerns. Compared with the comprehensive investigations on the safety of LEBs,^{184, 185} it is imperative to reveal the comprehensive safety characteristics of ASSBs from multiple aspects, guiding the safety design of sulfide-based ASSBs.

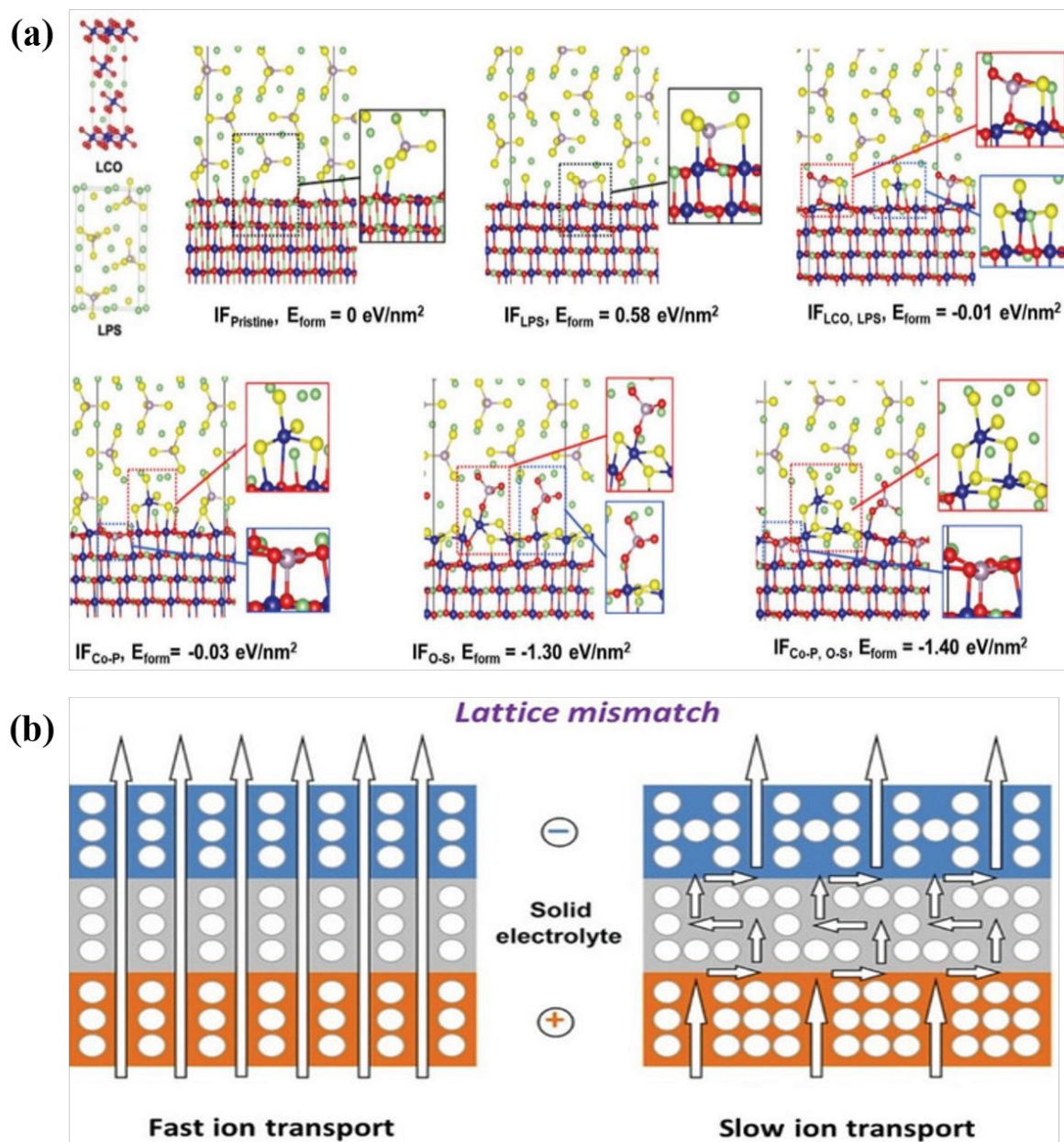


Fig. 8 (a) Predicted low-energy interface structures between LiCoO_2 and Li_3PS_4 for six different energy states.¹⁷⁷ (b) lattice-(mis)match¹⁴¹

2.3. Mechanical property

The mechanical characteristics of SEs represent a crucial aspect in the development of ASSBs.³² For instance, SEs need to possess high processability to establish close solid-solid



contact between electrode active materials (EAMs) and SEs.¹⁸⁶⁻¹⁸⁸ Achieving intimate contacts between solid particles is vital for ensuring high-performance metrics such as increased capacity, extended cycle life, and enhanced rate capability. In ASSBs, where both EAMs and electrolytes are solid, establishing close contact between the electrode and SE is challenging compared to traditional batteries employing LEs. Moreover, maintaining this contact throughout charging and discharging is essential despite the volume alterations experienced by the EAMs during these processes. The mechanical properties of both the electrode and SEs play a vital role in determining the integrity of the electrode/electrolyte contacts upon cycling. The elastic modulus serves as a crucial mechanical property for evaluating the electrode/SE contact.¹⁸⁹

In ASSBs, EAMs undergo expansion and contraction during the charge/discharge process. For example, silicon electrodes boast high theoretical capacities (3579 mAh g⁻¹ for the Li₁₅Si₄ phase) but experience significant volume changes exceeding 400%.¹⁹⁰⁻¹⁹² SEs play a crucial role in maintaining electrode/electrolyte contacts despite these volume changes in the EAMs. However, when SEs with very high elastic moduli are employed, the EAMs endure substantial stresses due to the volume alterations. Consequently, they may fracture and lose contact with the SEs, resulting in capacity degradation. The elastic modulus of SEs influences this fragmentation of electrode materials; ideally, SEs should possess an average elastic modulus that is neither excessively high nor extremely low.¹⁹³ SEs with moderate elastic moduli can alleviate such large stresses, thereby enhancing the longevity of ASSBs.

The physicochemical behavior of SEs differs significantly from that of LEs, especially in how they influence Li deposition. SEs are intrinsically inhomogeneous, containing grain boundaries and grains with distinct mechanical properties and carrier transport characteristics. Notably, the bulk electronic conductivity of SEs is higher than that of LEs, allowing Li ions to be reduced and deposited directly within the SE matrix. At the interface between SEs and electrodes, electrochemical reactions such as Li metal deposition occur at solid–solid contact points, enabling the transfer of charge carriers (either electrons or ions).¹⁹⁴⁻¹⁹⁶ These reactions induce mechanical changes in the SE, often resulting in localized lattice deformation.¹⁹⁷ Typically, such deformations are confined to surface regions, creating localized stress fields. In most SEs, which typically exhibit linear elastic fracture behavior, the level of local stress directly influences the ability of crack formation, as well as the dimensions, such as the length and width, of any cracks that develop.¹⁹⁸⁻²⁰⁰ The severity of the resulting mechanical damage



depends on the intensity of the stress and the dimensions of the developing cracks. Various theoretical models have been proposed to explain how Li protrusions grow within SEs, and all of them emphasize the strong relationship between Li metal electrochemical deposition and the generation of local mechanical stress.¹²⁵

The different mechanical processes in SSBs, localized in different areas of the cell, are illustrated in Fig. 9a. Key processes include: losing contact at the electrode/electrolyte interfaces, detachment from current collectors (Cu or Al foils), void generation at interfaces, crack propagation inside SEs, and the application of external pressure. These processes are induced and influenced by many electrochemical, chemical, and external factors. First, the volume changes (expansion or shrinkage) in cathodes and anodes due to the lithiation or delithiation have a profound effect on the solid/solid interface between electrode and electrolyte. The second major factor is the external pressure applied to the packaged cell and/or module, which is inevitable in single-cell and large battery packs. Moreover, dendrites and byproducts generated at the interfaces can also add local pressure. These mechanical effects have a significant influence on further electrochemical processes, such as impedance increasing, uneven distribution of the lithium-ion flux and the electrical field, fast decay in capacities, and short circuits. As a whole, the mechanical processes are intimately coupled with the electrochemical ones. The mechanical parameters in evaluating SSBs and corresponding characterization methods are summarized in Fig. 9b.

In addition, SSBs use composite electrodes made up of electrochemically active materials, SEs, and, when needed, additional components such as binders or conductive additives like vapor-grown carbon fibers (VGCF). In these composite structures, achieving sufficiently high ionic conductivity (σ_{io}) and electronic conductivity (σ_{e}) is essential, as both charge carriers must effectively reach the active material during charging and discharging. A significant mismatch between ionic and electronic conductivity can result in uneven reaction rates across the electrode's thickness. It is crucial to balance these transport properties to ensure efficient electrode utilization and prevent localized reaction fronts during operation.^{201, 202}

The transport of charge carriers is strongly affected by the microstructure of the composite. For example, Froboese et al.²⁰³ showed how varying the size of inclusions impacts the composite's effective ionic conductivity. Further research on NCM622-LPSCI²⁰¹ and Si-LPSCI-C²⁰²



electrodes demonstrates that changes in active material particle size significantly influence battery performance, reinforcing the importance of microstructural control. Similarly, adjusting the SE particle size in $\text{LiNi}_{0.83}\text{Co}_{0.11}\text{Mn}_{0.06}$ (NCM83)-LPSCI²⁰⁴ composites leads to more uniform ion flow and better electrode utilization. These findings highlight that the particle sizes of both the active material and the solid electrolyte are critical factors in optimizing electrode design.

Ketter et al.²⁰⁵ measured the effective ionic and electronic conductivities in NCM83-LPSCI composite cathodes by varying the volume fractions of NCM83 (ϕ_{NCM}) and LPSCI (ϕ_{LPSCI}), using EIS. To analyze electronic and ionic conductivity separately, they applied ion-blocking contacts for electronic measurements and electron-blocking contacts for ionic measurements (as shown in Fig. 9c). The impedance data were interpreted using a transmission line model (TLM), previously developed for similar NCM622-LPSCI composite systems.²⁰⁶ This TLM acts as an equivalent circuit representing ion and electron transport through interconnected pathways in the composite cathode. Although the model simplifies the complex nature of charge transport in such composites, it captures key behaviors and allows accurate determination of total effective conductivities from EIS data.²⁰⁶

Figure 9d illustrates typical impedance results and their TLM fits for a composite cathode with 40% NCM83. To further validate the TLM, the researchers used an alternative equivalent circuit commonly applied to mixed ionic-electronic conductors²⁰⁷ to assess the same data, demonstrating consistent results. In addition, DC polarization experiments were performed to evaluate ionic and electronic currents by applying different voltages and blocking contacts to isolate each charge carrier type. These measurements, interpreted using Ohm's law (Eq. 2), yielded effective conductivity values. An exemplary dataset for $\phi_{\text{NCM}} = 40\%$ is shown in Fig. 9e.

An equivalent relation for the movement of charge carriers (ions and electrons) as a response to an electric field is given by Ohm's law (Eq. 2), following²⁰⁸:

$$\mathbf{J} = -\sigma \nabla \phi \quad (2)$$

where \mathbf{J} , σ , and $\nabla \phi$ are the electrical flux density, the electrical conductivity, and the potential gradient, respectively.



The measured and simulated effective electronic and ionic conductivities are in good agreement as shown in Fig. 9f. Consistent with previous findings²⁰⁶, the effective conductivities of both ions and electrons vary dramatically depending on the ratio of NCM83 to LPSCl. Specifically, electronic conductivity spans from about 10^1 mS cm⁻¹ to 10^{-2} mS cm⁻¹, while ionic conductivity ranges from 10^1 mS cm⁻¹ to 10^{-5} mS cm⁻¹ across the compositions tested. The best ionic and electronic transport balance is observed at $\phi_{\text{NCM}} = 40$ %. However, as the content of either LPSCl or NCM83 becomes too low, both conductivities drop sharply due to a loss of percolation pathways. Since the percolation threshold is highly influenced by the material's microstructure, significant discrepancies between experimental and simulated conductivity values are more likely near the threshold as only simplified, virtual microstructures are assumed in the resistor network simulations.^{209, 210} Differences in the measured and simulated effective ionic conductivities for compositions with $\phi_{\text{NCM}} > 40$ % may be attributed to this effect.



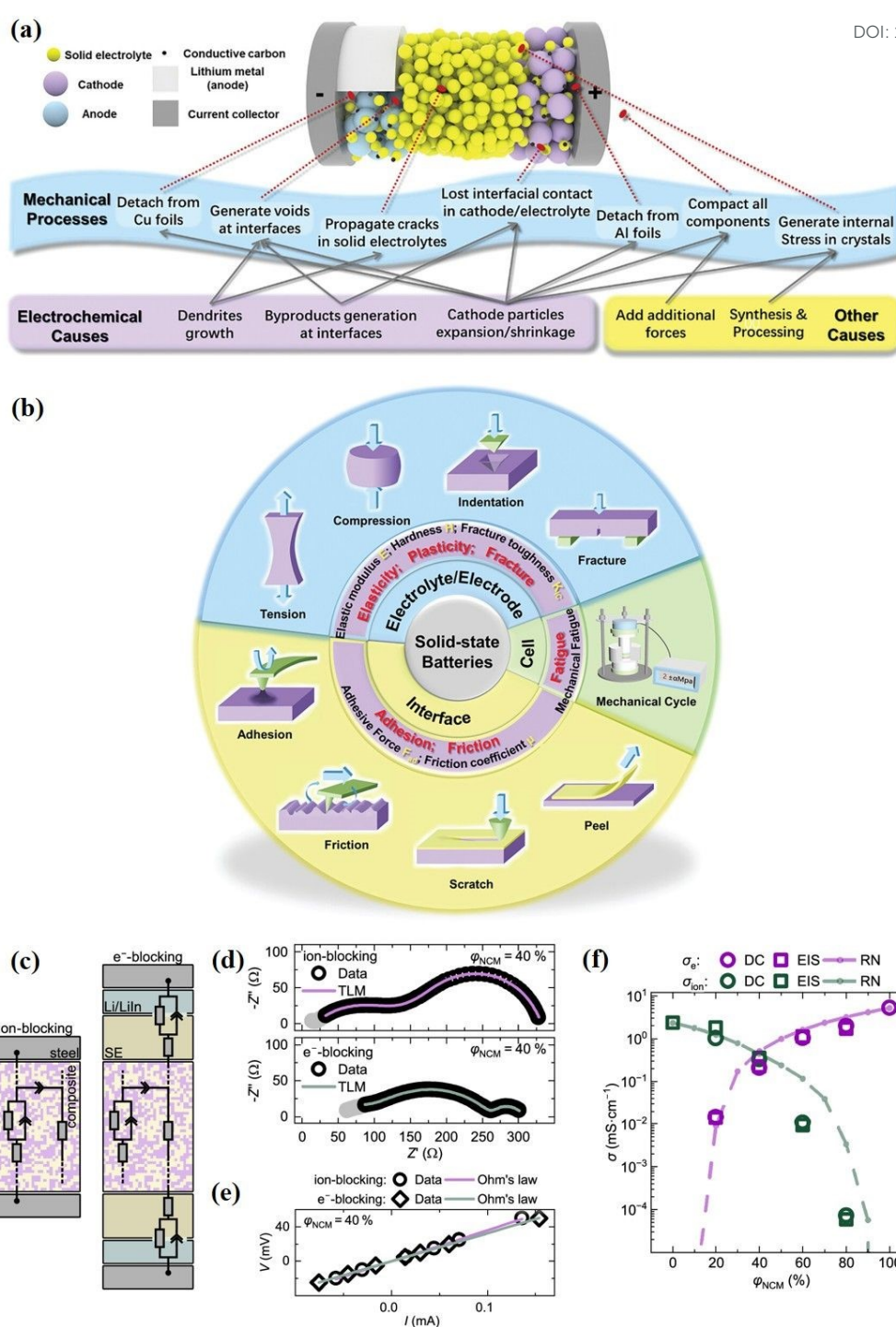


Fig. 9 (a) Schematic of mechanical processes and their causes in SSBs. (b) The mechanical parameters and corresponding characterization methods used in SSBs.²¹¹ (c) Schematic setups used to ensure ion-blocking and electron-blocking measurement conditions respectively together with transmission line models (TLM) used to evaluate impedance data. (d) EIS data (circles) measured under ion- and electron-blocking conditions are exemplary for an NCM83-LPSCl composite with an NCM volume fraction of 40 %. (e) Direct current (DC) polarization





data measured under ion-blocking (circles) and electron-blocking (diamonds) conditions respectively, as well as the corresponding fits (line) are exemplarily shown for an NCM83-LPSCI composite with a NCM volume fraction of 40 %. (f) Resulting effective ionic- and electronic conductivities as a function of NCM volume fraction. Effective electronic conductivities measured via DC polarization (circles) and EIS (squares) are shown in purple, whereas effective ionic conductivities are depicted in green. Each data point corresponds to a single measurement. Effective conductivities from simulations with the resistor network model are shown as dots connected with straight dashed lines as guide to the eye.²⁰⁵

Recently, researchers have utilized first-principles calculations to predict the elastic moduli of different SEs.²¹² This effort underscores the significance of identifying the optimal mechanical properties for ASSBs and advancing the development of SEs with enhanced mechanical characteristics.¹⁹³ Key mechanical parameters to be taken into account for SEs are outlined in Table 2.

Table 2. First Principles Calculations for bulk modulus (B), shear modulus (G), Young’s modulus (E), Poisson’s ratio (ν), and Pugh’s ratio (G/B) of Li-argyrodites $\text{Li}_6\text{PS}_5\text{X}$ (X = Cl, Br, I) utilizing PBEsol functional.²¹²

Electrolyte	B (GPa)	G (GPa)	E (GPa)	ν	G/B
$\text{Li}_6\text{PS}_5\text{Cl}$	28.7	8.1	22.1	0.37	0.28
$\text{Li}_6\text{PS}_5\text{Br}$	29.0	9.3	25.3	0.35	0.32
$\text{Li}_6\text{PS}_5\text{I}$	29.9	11.3	30.0	0.33	0.38

Addressing interfacial resistance entails optimizing the contact between materials, a pursuit that has been investigated on a macro scale through different synthesis and assembly methods.²¹³ Enhanced adhesion contributes to prolonged mechanical lifespan in ASSBs by ensuring consistent interface contact during cycling. Experimental evidence supports this notion, as demonstrated by the application of pressure to cells, facilitating improved wetting or adhesion of interfaces.²¹⁴ In ASSBs, expanding the contact area between materials is crucial for leveraging the bulk σ offered by Li-P-S systems.

3. Strategies to improve the interface stability

View Article Online
DOI: 10.1039/D5EB00101C

Because of Li metal's strong reactivity, limited materials are stable towards Li.^{63, 215} The critical factor for effectiveness in LIBs is the self-passivating SEI layer formed at the LE/electrode interfaces. This concept recently started to be explored in the ASSB domain. Advancing the discovery of non-reactive SEs at interfaces is a critical step for the development of next-generation batteries. However, this focus does not address the operational voltage or interfacial resistance criteria.²¹⁶

The strategies proposed to improve the interfacial stabilities include coating, electrolyte modification by doping, wetting, and multilayered approaches.

3.1 Coating

Applying coating materials is the best approach to tackle the interfacial problems, and enabling a wider range of combinations of SE and electrodes to be used for the success of the battery. Coatings must possess electrochemical stability windows that sufficiently cover the entire operational voltage range of the electrodes. Nevertheless, even if two materials are chemically inert and show stability in similar voltage ranges, they can still encounter significant interfacial resistance.²¹⁷

Kimura et al.²¹⁸ systematically investigated how the thickness of a coating layer (CL) affects the protection of SEs, under fixed values for electronic conductivity (σ_{ele}) and other related parameters. They assumed σ_{ele} values of $1.0 \times 10^{-11} \text{ S cm}^{-1}$ for the SE and $1.0 \times 10^{-14} \text{ S cm}^{-1}$ for the CL, with the lithium-ion conductivity (σ_{Li^+}) of the CL set at $1.0 \times 10^{-6} \text{ S cm}^{-1}$. Fig. 10a shows the lithium chemical potential (μ_{Li}) distribution within the SE and CL when the thickness of the CL is 10, 50, and 100 nm and the thickness of the SE is 100 μm . As the CL thickness increases, the μ_{Li} variation within the coating becomes larger, which raises the μ_{Li} at the CL/SE interface. Notably, coatings thicker than 50 nm shift the μ_{Li} above the SE's oxidation limit, making the SE thermodynamically stable. This supports the intuitive understanding that thicker coatings offer stronger protection, especially when ultra-low σ_{ele} materials aren't available.

However, the required thickness of a CL to effectively protect a SE varies considerably based on the thickness of the SE. As shown in Fig. 10b, the protective effect changes when the CL remains 10 nm thick but the SE thickness is varied (100, 50, and 20 μm). For the 100 μm SE, μ_{Li} at the interface remains below the oxidation limit, indicating instability, while SEs 50 μm



or thinner show interfacial μ_{Li} values within the stable electrochemical window. Hence, the thickness of the SE directly impacts how well a given CL performs.

Figure 10c plots the relationship between μ_{Li} at the interface and the thickness ratio ($L_{\text{CL}}/L_{\text{SE}}$). A sharp increase in interfacial μ_{Li} is observed until the CL reaches about 0.2% of the SE thickness, stabilizing around 0.02%. This means that, for a 100 μm -thick SE, a coating thickness below 200 nm is often sufficient for protection. Crucially, this shows that the relative thickness, not the absolute thickness, of the CL determines its effectiveness. Consequently, a CL that performs well in thin-film SSBs may not offer the same protection in bulk-type batteries, and vice versa. Any comparison of CL performance across systems must consider the SE geometry.

Moreover, the ideal CL thickness also depends on the relative σ_{ele} values of the CL and SE. Figure 10d shows a heat map of μ_{Li} at the CL/SE interface under varying σ_{ele} and thickness ratios. A white dashed line marks the oxidation stability limit. For a CL to protect the SE thermodynamically, both its thickness and σ_{ele} must fall below this line. The map reveals that at very thin coatings (e.g., <10 nm for a 100 μm SE), small changes in thickness dramatically shift the required σ_{ele} . Therefore, in practical battery design, achieving effective SE protection requires carefully balancing both the thickness and electronic conductivity of the coating layer.

As previously outlined, the protective effect of a CL on an SE in SSBs is influenced by both σ_{ele} of CL and its thickness. While a lower σ_{ele} and greater thickness are generally favorable for SE protection, practical considerations in composite electrodes, especially those without conductive additives, complicate this relationship. In composite electrodes, especially those lacking conductive additives, CAMs serve as the primary electron conduction pathways. Applying a thick CL with low σ_{ele} , as illustrated in Fig. 10e, over the CAMs can significantly increase the electron conduction resistance across the entire electrode, potentially degrading SSB performance.^{219, 220} However, in real composite electrodes with the CL, such a substantial increase in resistance is often mitigated by partial fracturing of the CL during electrode fabrication processes, such as pressing (Fig. 10e). These fractures can restore electron conduction pathways, reducing the overall resistance. The impact of the proportion of CLs is shown in Fig. 10f. When 70% of the CAM surface is coated, the resistance shows significant variation depending on the arrangement of the AM and SE lattices, likely because of differences in the availability of current percolation pathways that allow current to flow solely through the CAM regions. When the CL coverage is reduced to 50% or less, the increase in



electron conduction resistance remains within acceptable limits, suggesting that partial coverage can balance SE protection and electron conduction. However, this means that over half of the interface remains unshielded, underscoring the challenge of achieving solid electrolyte protection and low resistance in practical composite solid-state battery electrodes.

An alternative strategy involves coating the SE instead of the CAMs. This approach maintains direct contact between CAMs, preserving electron conduction pathways, and typically results in a less pronounced difference in σ_{Li^+} between the SE and CL compared to the σ_{ele} difference between CAMs and CL (Fig. 10g). Consequently, the overall ion conduction resistance of the electrode does not increase significantly, even with a fully coated SE. Fig. 10h presents violin plots illustrating the electron conduction resistance of the whole electrode under various CAM coating conditions. The total resistance in the case of fully coated CAMs is about 8 to 9 orders of magnitude higher than uncoated CAMs. This outcome clearly shows that even though the CL is much thinner than the CAM, a coating layer with low σ_{ele} can significantly increase the overall electron conduction resistance of the electrode, indicating the strong influence of the CL on electrode performance. Fig. 10i presents the total ionic resistance of the composite electrode when the SEs are coated with a 10 nm-thick CL. In this model, the σ_{Li^+} of the SE and CL are set to 0.5×10^{-3} and $1.0 \times 10^{-6} \text{ S cm}^{-1}$, respectively, with ion transport attributed solely to the SE and CL. Under these conditions, the increase in ionic resistance remains relatively minor, even with full coating of the SEs. This indicates that applying the coating to the SE rather than the CAM may be a promising approach to simultaneously protect the SE and maintain low internal resistance. However, some technical hurdles may need to be addressed.

These findings demonstrate the importance of considering not only the intrinsic properties of the CL but also its spatial arrangement within the composite electrode. The geometry and coverage of the CL relative to the SE and CAMs are critical design parameters that influence the performance and thermodynamic stability of SSBs.



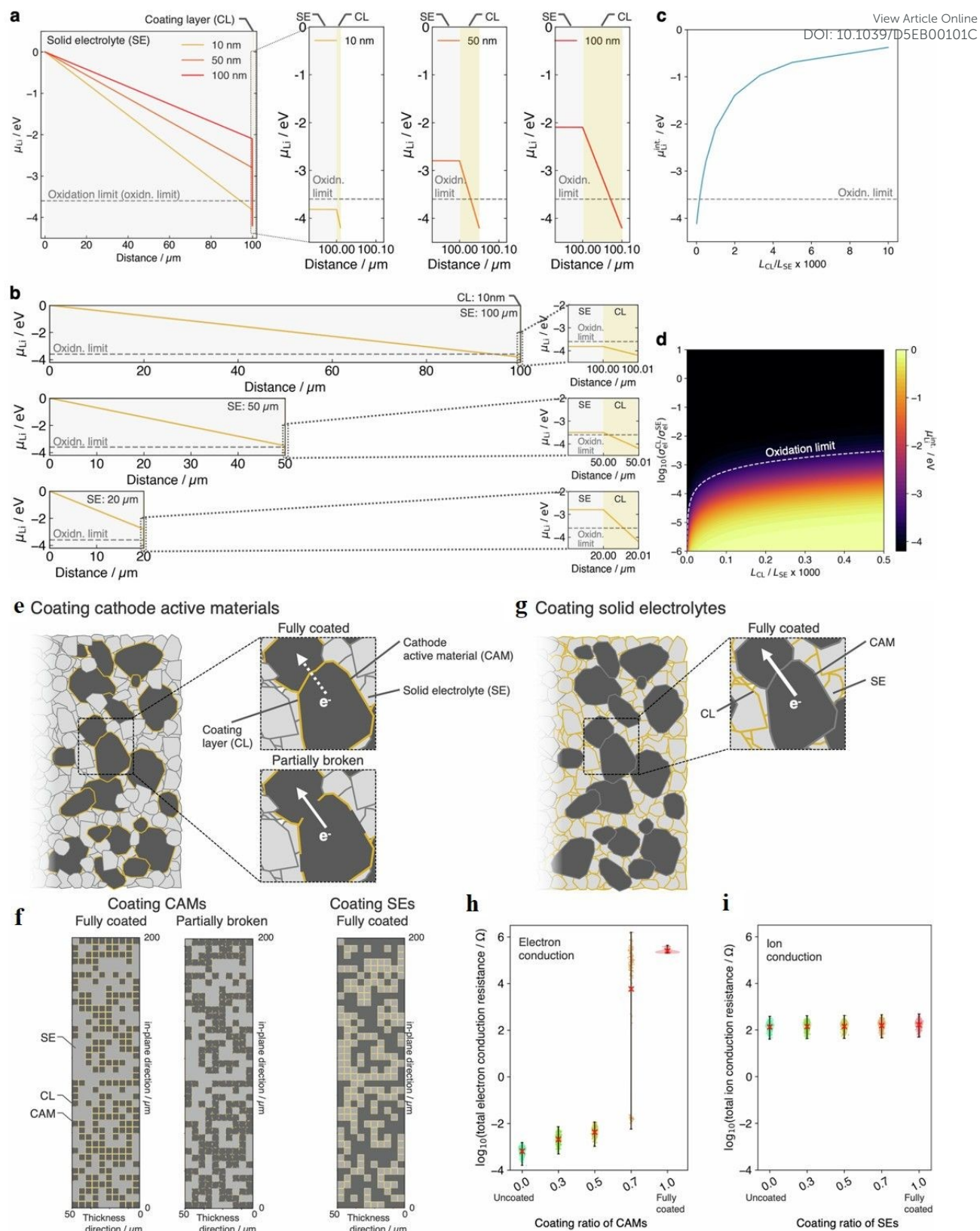


Fig. 10 Influence of the thickness of the CL and SE on the protective capability of the CL. (a) μ_{Li} distribution within the SE and CL for the thickness of the CL of 10, 50, and 100 nm, with the thickness of the SE constant at 100 μm . (b) μ_{Li} distribution with the thickness of the SE of

100, 50, and 20 μm , maintaining the thickness of the CL at 10 nm. (c) μ_{Li} at the interface as a function of the thickness ratio of the CL to SE. (d) Heat map illustrating the μ_{Li} at the interface between the SE and CL across varying thickness ratios and σ_{ele} ratios of the CL to SE. Influence of the arrangement of the CL in composite electrodes on the ohmic resistance. (e) Schematic of a composite SSB electrode with CLs applied to CAMs. (f) 2D lattice model of the composite SSB electrode with CAMs either fully or partially covered by CLs (left) and SE-coated configuration (right). (g) Schematic of a composite SSB electrode with CLs applied to SEs. Violin plots of (h) the electron conduction resistance of the entire electrode under various CAM coating ratios and (i) the ion conduction resistance of the entire electrode under various SE coating ratios. The red cross in each plot represents the average resistance for each condition.²¹⁸

3.1.1 Electrolyte coating

A coating layer protects the direct contact of SE and electrode. This layer helps as an artificial SEI, facilitating the Li^+ conductivity while inhibiting electron conduction. As a result, it extends the effective stability range of the solid electrolytes. The thickness of the coatings can be adjusted to fall within the range of 1 to 10 nm^{178, 221, 222}, typically thinner than an SEI formed in situ.^{178, 223-225} The coating material must meet crucial criteria: it should be chemically stable towards the SE and the corresponding electrode and demonstrate stability across the operational voltage ranges of the electrodes. As a result, the constitution of cathode and anode coatings could be individually optimized based on the specific solid electrolyte-electrode combination.

Hood et al. examined the role of Al_2O_3 coating towards $\text{Li}_6\text{PS}_5\text{Cl}$ powders.²²⁶ To gain a comprehensive understanding of how atomic layer deposition (ALD) alumina coatings and their thickness influence the electrochemical performance of argyrodite, the authors assessed key properties such as ionic conductivity, Arrhenius activation energy, and electronic conductivity using pellets formed from coated powders. Prior research has shown that fine-tuning both bulk and surface chemistry is crucial for optimizing the electrochemical behavior of fast lithium-ion conducting electrolytes.^{118, 227, 228} Using EIS, the authors measured the total ionic conductivity of both coated and uncoated argyrodite pellets (see Figs. 11a and 11b). The uncoated (pristine) argyrodite exhibited a Li^+ conductivity of $0.9 \pm 0.05 \times 10^{-3} \text{ S cm}^{-1}$ at room temperature (25 °C), with an activation energy of $0.31 \pm 0.03 \text{ eV}$. Interestingly, the materials coated with 1 and 10 cycles of ALD Al_2O_3 showed significantly improved ionic conductivities of $1.2 \pm 0.05 \times 10^{-3} \text{ S cm}^{-1}$ and $1.7 \pm 0.05 \times 10^{-3} \text{ S cm}^{-1}$, respectively. This enhancement was accompanied by a slight reduction in activation energy, to $0.30 \pm 0.02 \text{ eV}$ for 1 cycle and 0.28



± 0.02 eV for 10 cycles, indicating that thin ALD coatings can enhance Li^+ transport. However, when the coating thickness was increased to 100 ALD cycles, the ionic conductivity dropped sharply to $0.27 \pm 0.05 \times 10^{-3} \text{ S cm}^{-1}$ at 25 °C, while the activation energy remained relatively low at 0.29 ± 0.02 eV. This decline in conductivity is likely due to the thicker Al_2O_3 layer acting as a barrier to Li^+ movement across grain boundaries, given the poor lithium-ion conductivity of Al_2O_3 . These results suggest that the optimal ALD coating thickness lies around 1–2 nm, beyond which Li^+ transport becomes impeded.

The authors hypothesize that the enhanced electrochemical performance, specifically the increase in room-temperature ionic conductivity and the reduction in activation energy, is likely due to a combination of matrix and grain boundary effects. These effects arise from the redistribution of vacancies and interstitial sites, such as space-charge regions, at the interface between the ALD alumina coating and the argyrodite electrolyte.^{229–232} This behavior is similar to previously reported electrochemical results observed in $\beta\text{-Li}_3\text{PS}_4\text{:Al}_2\text{O}_3$ composites.²³² While ball milling-based composite formation can introduce layers of electronic and ionic point defects, the close interfacial contact formed via ALD can similarly influence ion transport. However, when the ALD coating is too thick and non-conductive, it acts as a barrier to Li^+ movement, significantly lowering ionic conductivity, as seen with 100 ALD alumina cycles coatings. Thus, precise control over both the coating thickness and its chemical properties is essential to properly manipulate space-charge effects and enhance ionic transport. Applying highly conductive ALD coatings to Li argyrodite materials could be a promising strategy for improving total ionic conductivity.

Besides aiding Li^+ transport, ALD alumina coatings also reduce electronic conductivity in argyrodite powder-based pellets. Electronic conductivity was measured using symmetric cells under a 200 mV bias (Figs. 11c and 11d). For the uncoated $\text{Li}_6\text{PS}_5\text{Cl}$, the electronic conductivity was $6.3 \pm 0.05 \times 10^{-9} \text{ S cm}^{-1}$ at 25 °C. After applying 1, 10, and 100 ALD Al_2O_3 cycles, the electronic conductivity dropped significantly, reaching as low as $1.7 \pm 0.05 \times 10^{-9} \text{ S cm}^{-1}$. These results show that carefully adjusting the ALD coating's thickness and composition enables control over both lithium-ion transport and undesirable electronic leakage in solid electrolyte membranes.

The authors concluded that coating improved the stability of argyrodites in humid and oxidizing conditions, effectively protecting them from reacting with Li metal. This



improvement led to significantly enhanced overall electrochemical performance, enabling higher current densities, Li metal plating/stripping capacities, and extended cycle lifetimes.

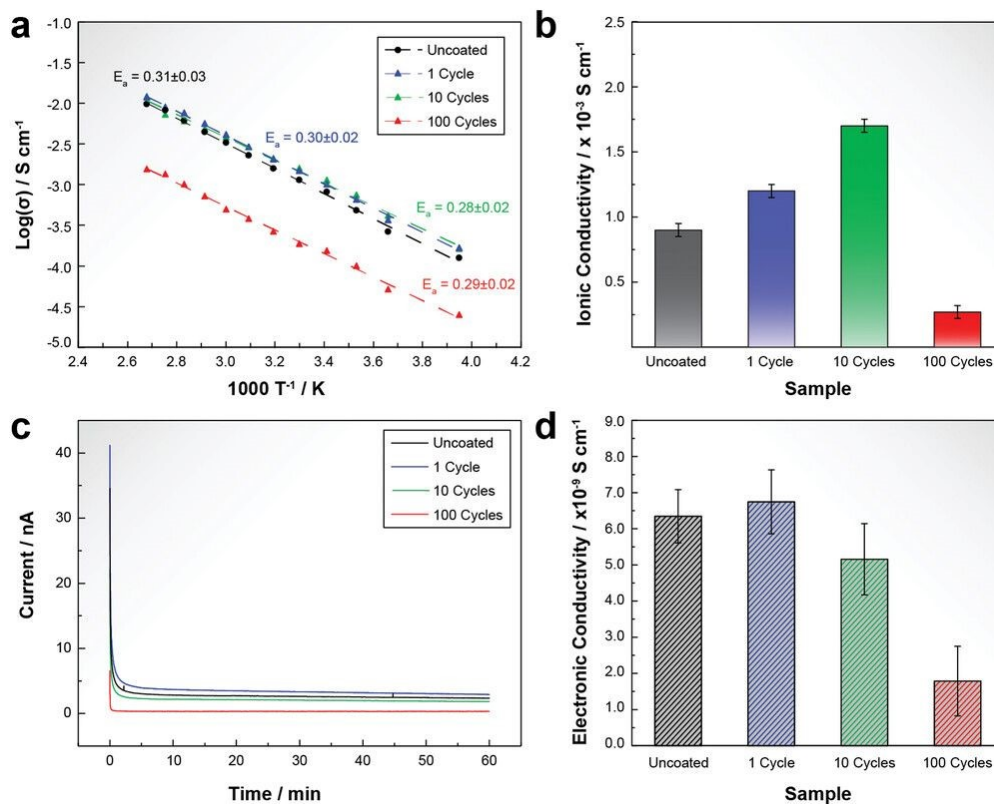


Fig. 11 (a) Arrhenius plots, (b) ionic conductivity at 25°C, (c) current-time curves (DC polarization at 200 mV, 25°C) and (d) electronic conductivity at 25°C for $\text{Li}_6\text{PS}_5\text{Cl}$ pellets pressed from powders coated by 1, 10, and 100 ALD alumina cycles in comparison to pellets pressed from uncoated powders.²²⁶

Through computational work, Ransom et al. identified LiAl_5O_8 and LiAlSiO_4 as leading coating candidates for various electrolyte systems²³³. Their flexible morphologies enable simpler synthesis approaches and offer versatile avenues for optimization, including adjusting the lithium content. These coatings exhibited good adhesion characteristics, along with $E_{\text{rxn}} < 0.1$ eV. The versatility in synthesizing LiAl_5O_8 material into nanowire composites sintered thin films, and sol-gel coatings, each offering different electrochemical enhancements, provides ample opportunities for optimizing this compound.²³⁴⁻²³⁶ Despite its individual Li-ion conductivity being around $\sim 10^{-6} \text{ S/cm}$, its capability to form films thinner than 10 nm can mitigate the effects of its low σ .²³⁷ LiAl_5O_8 also helps reduce electrochemical reaction and chemical decomposition of the cathode materials. Wang et al. further discovered that LiAl_5O_8



can inhibit lithium metal dendrite formation in ASSBs.²³⁶ Its ability to optimize various electrochemical metrics makes LiAl_5O_8 highly promising for further development. LiAlSiO_4 is similarly feasible for further research, having demonstrated improved capacity retention and been experimentally confirmed for synthesis and assembly into the battery.²³⁸ The synthesis approaches leverage the glassy nature of this material, with its amorphous phase enhancing σ .²³⁹ LiAlSiO_4 may be produced and coated utilizing simpler solution and dry methods, making it an attractive option for further development. There is potential for optimizing lithium content, as studies have explored adjusting the weight ratios of the coatings and enhancing σ through thin film morphologies.^{240, 241} Li_4SiO_4 and $\text{Li}_5\text{GaSi}_2\text{O}_8$ share structural similarities with LiAlSiO_4 , suggesting that exploring the glassy phases of these coatings could enhance σ .²⁴² Furthermore, $\text{Li}_2\text{B}_6\text{O}_9\text{F}_2$ has emerged as the most efficient coating specifically for sulfide SE systems and has been verified via computational investigations.²⁴³

3.1.2 Anode coating

As we already mentioned, the theoretical capacity of lithium metal anodes (3860 mAh g^{-1}) is approximately ten times greater than that of graphite (372 mAh g^{-1}). This makes lithium metal a leading candidate for high-energy-density ASSBs. It has been extensively researched for use in both LE-based and ASSBs.²⁴⁴ However, the cycling life of batteries utilizing lithium metal anodes still requires enhancement for practical applications.

Failures in lithium metal batteries often originate from the lithium anode. The initially shiny metallic lithium foil becomes black after several cycles due to the formation of a microporous, mossy structure (Fig. 12a)²⁴⁵. This mossy lithium is covered by a passivation layer (SEI), and the emergence of "dead lithium" reduces anode capacity²⁴⁶. Additionally, the porous nature of lithium metal with a high surface area encourages a degradation reaction and rapidly depletes the SE, which raises cell impedance. Therefore, various approaches are proposed to enhance the cycling span of lithium anodes, mainly focusing on reducing the degradation reaction between Li and SE while ensuring electrical contact among the deposited Li particles (Fig. 12c). One of the best approaches to address this issue is applying protective coatings.

Protective coatings serve as ion-conductive layers that allow for the electrodeposition of lithium metal (Fig. 12b). As lithium ions move throughout coatings, the ion flux will be highly uniform around the electrode's surfaces, promoting even lithium deposition.^{246, 247} Protective layers also minimize the electrolyte/lithium contact areas, reducing side reactions. Unlike the SEI layer that forms from side reactions within batteries, protective coatings are considered



artificial SEI layers. The constitution of these coatings can be adjusted to enhance σ and mechanical strength^{248, 249}.

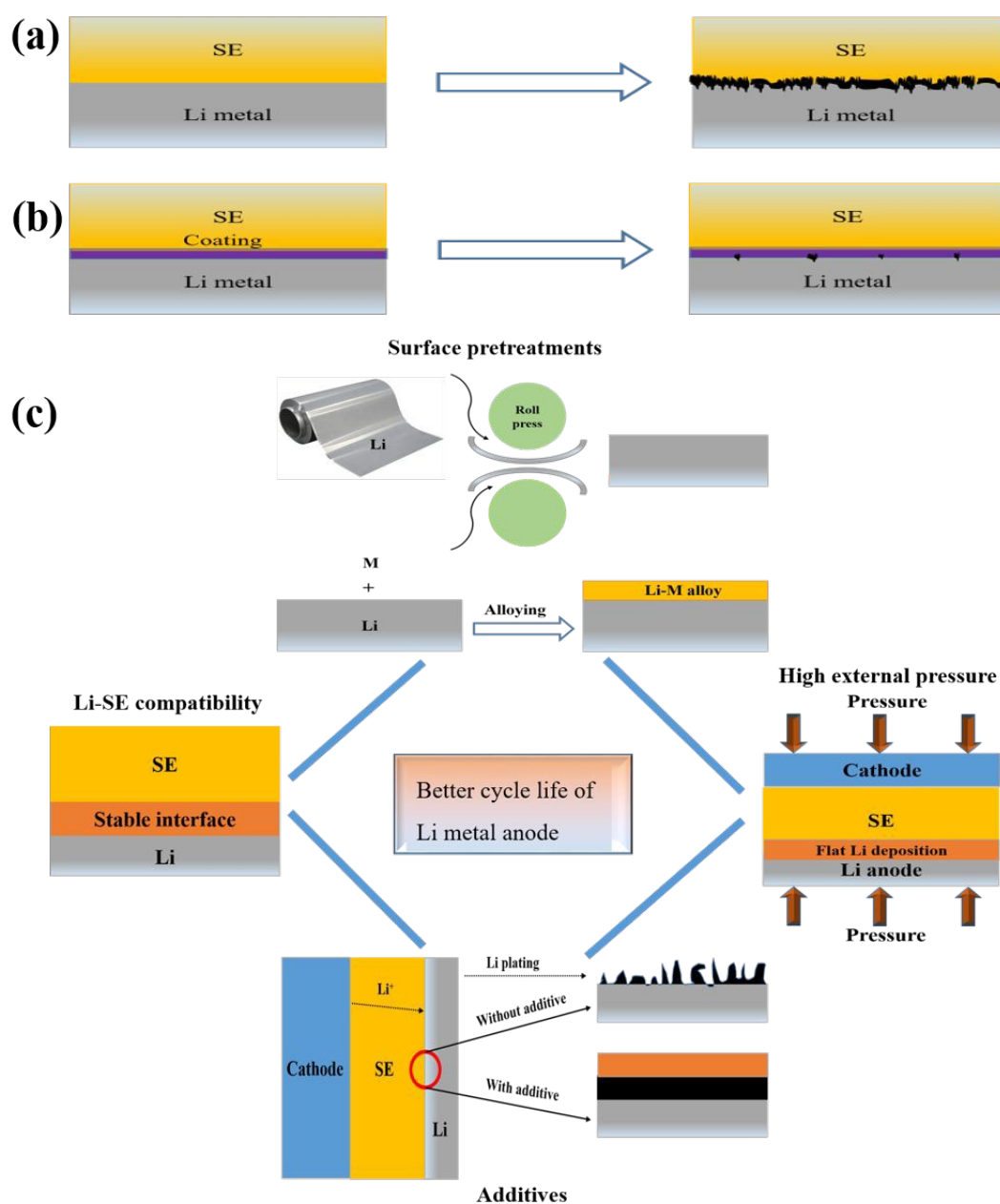


Fig. 12 (a) Porous surface of electroplated lithium anode after extended cycling. (b) The dense surface of lithium anode is electroplated underneath the protective coating. (c) Approaches to enhance the cycling span of lithium metal anodes.

To stabilize the SE/Li interface, various kinds of materials, such as oxides and nitrides, has been employed. Compounds within the Li–Al–O chemical family have effectively protected different solid electrolytes from lithium metal.^{33, 250, 251} The computed stability window of Li_5AlO_4 ranges from 0.06 to 3.07 V, indicating strong stability of Al^{3+} contacted with Li, which



aligns with XPS measurements at the SE/Li interfaces.²⁵² Additionally, *in situ*-formed polyanionic compounds like Li_3PO_4 and LiH_2PO_4 have been utilized to stabilize SE/Li interfaces.^{253, 254} DFT calculations predict that Li_3PO_4 will generate Li_3P and Li_2O when in contact with lithium, while LiH_2PO_4 will yield LiH . These reaction products help create a passivating layer that facilitates stable cycling in Li symmetric cells.²⁵³ Furthermore, in investigating alternative anion chemistries for stabilizing the solid electrolyte against reduction by lithium, nitrides have shown the lowest calculated reduction limits among various anion types, making them promising for protecting the SEs on the anode side.²⁵⁵ Notably, boron nitride (BN) has recently been reported to effectively safeguard the SE/Li interface²⁵⁶, and an SE has shown excellent stability with lithium, as evidenced by a stable cycle life in a Li symmetrical cell.²⁵⁷

The coatings with the highest stability for the sulfide system demonstrate good adhesion towards the lithium anode (E_{rxn} of 0 eV). However, they exhibit less favorable adhesion towards the SEs. Recent studies have explored the combined use of LiCl and LiBr to enhance σ , as LiCl alone has been found to have inadequate conductivity (approximately 10^{-6} S/cm).²⁵⁸⁻²⁶⁰ Previously, Lutz et al. examined LiCl species as a coating material, although the potential of CsLiCl_2 has not been thoroughly investigated.²⁶⁰ Additionally, Marcela et al. prepared an argyrodite type $\text{Li}_6\text{PS}_5\text{Cl}$ -based SE-coated graphite (graphite: $\text{Li}_6\text{PS}_5\text{Cl}$, 64:36 weight ratio) using a dissolution-precipitation method and investigated its application as a negative electrode in ASSBs. The half-cell assembled with the argyrodite-coated graphite and a carbon additive in a 100:1 weight ratio showed discharge capacities of 335 and 372 mAh g^{-1} at 8C via 25 °C and 100 °C, respectively.²⁶¹

Besides the above observations, Zheng et al. developed a dual-purpose functional material that both protects the Li metal from air/water corrosion and acts as an SE.²⁶² As shown in Fig. 13a and Fig. 13b, bare lithium transforms from a smooth surface to a porous network after 30 minutes in a 60% humidity environment. In contrast, lithium protected by PVDC (Li@PVDC) retains its metallic shine and remains smooth and crack-free under the same conditions. Fig. 13c indicates that the Li/Li symmetric cell performance of Li@PVDC initially matches that of bare lithium, highlighting its effectiveness in facilitating lithium ion transport. However, after 30 minutes of air exposure, bare lithium significantly increases plating/stripping overpotential, indicating diminished performance. In contrast, Li@PVDC maintains stable overpotential levels (Fig. 13d). The bare lithium cell experiences rapid polarization increases and short circuits around 155 hours, while the Li@PVDC cell demonstrates consistent performance for



over 250 hours, underscoring the protective coating's role in enhancing stability and reducing dendrite formation during cycling.

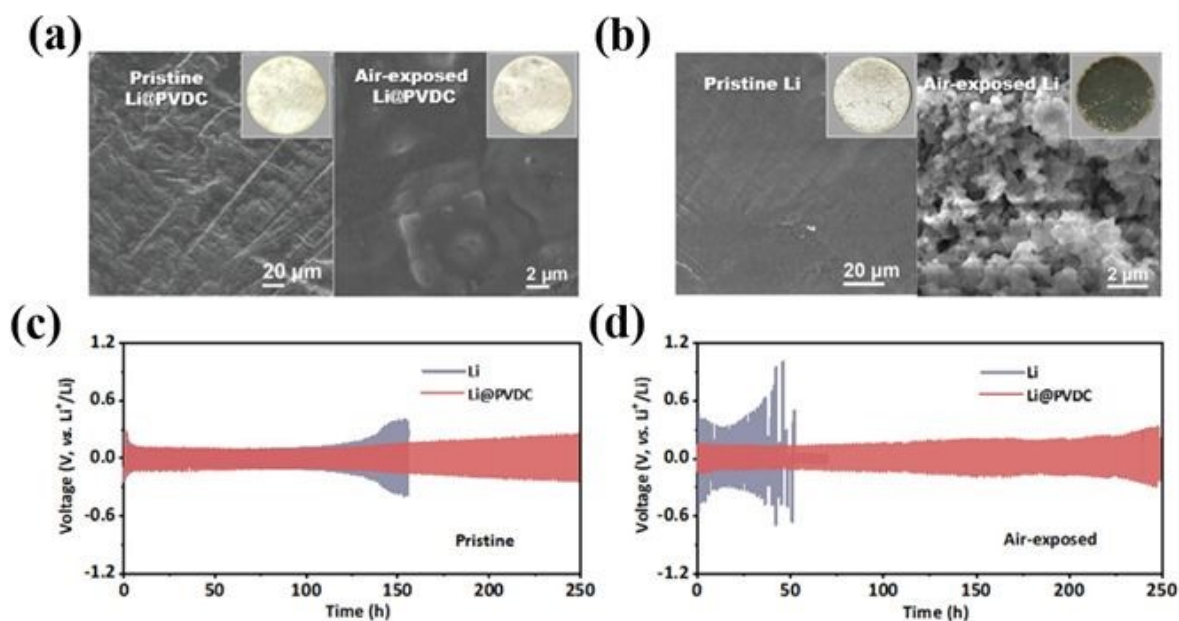


Fig. 13 The role of interlayers in suppressing air corrosion in lithium metal anode. SEM images of (a) Li@PVDC and (b) bare lithium before and after exposure to ambient air 30 min. Voltage profiles of bare lithium and Li@PVDC symmetric cells (c) without and (d) with 30 min air exposure at 1 mA cm^{-2} and 1 mAh cm^{-2} .²⁶²

3.1.3 Cathode coating

Many studies concentrate on the cathode/SE interface because it is crucial to always ensure efficient ion transport across this interface. Maintaining thermodynamic stability here is difficult due to the limited ESW of various SEs and their significant chemical reactivity with cathodes. When the solid electrolyte is thermodynamically unstable at elevated voltages, it can degrade into phases that typically exhibit lower σ . For instance, sulfide electrolytes are expected to oxidize above approximately 2.5 V versus lithium metal^{29, 80, 263} and may degrade into phases with diminished or negligible Li amount.⁸⁰ Moreover, the inter-diffusion of elements/chemical reactions at solid electrolyte/cathode interfaces can produce phases that hinder ionic transportation.^{178, 263}

The main approach to address the strict stability requirements is to apply electronically insulating but ionically conductive coating. This coating introduces coating/electrode material and coating/solid electrolyte additional interfaces. The coating acts like a secondary electrolyte, necessitating stability at the electrode voltages and resistance to chemical interactions towards



electrode and solid electrolyte. But, if imperfections in the coatings leave portions of the electrode exposed to the SE, undesirable interfacial reactions may still take place within the coated electrode system. Conversely, these imperfections might be essential for facilitating electron transportation at coated electrodes/CC interfaces, creating a dilemma in currently used coating strategies.²¹⁹ LiAl_5O_8 , used as a coating on nickel-manganese-cobalt cathodes, has been shown to enhance coulombic efficiency and capacity retention.²³⁴ In addition, ASSLBs using gradient $\text{Li}_3\text{P}_{1+x}\text{O}_4\text{S}_{4x}$ coated NCM811 were reported to show an elevated reversible capacity of $\sim 160 \text{ mAh g}^{-1}$ at 0.089 mA cm^{-2} at $25 \pm 5^\circ \text{C}$ with excellent retention of 80% after 250 cycling when combined with the commercial sulfide SE.²⁶⁴ Fig. 14 provides a schematic representation of the diverse range of interfaces found in cathode composites.

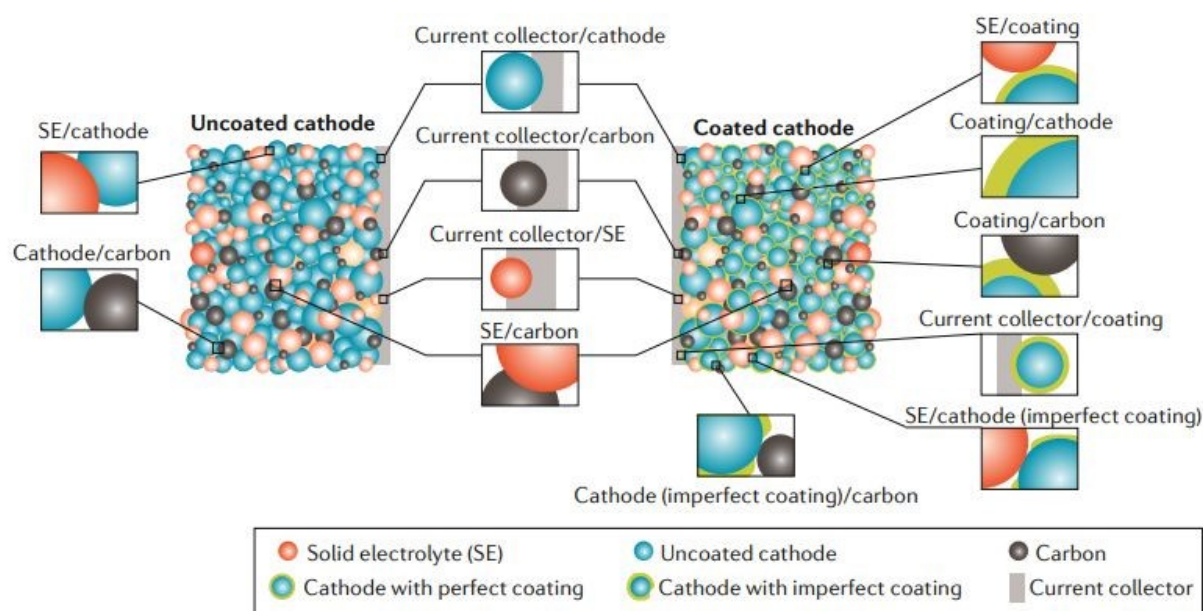


Fig. 14 Interfaces within cathode composites. A schematic representation of the different cathode composite interfaces within ASSBs, both with and without cathode coatings.⁶³

Furthermore, Jung et al. explored the distinct impact of cathode and sulfide SE chemical reactions in solid-state batteries.²⁵ Their findings revealed that the impedance of the composite electrodes, including bare NCM and LiNbO_3 -coated NCM, exhibited two semicircles representing ionic and electronic pathways (Figs. 15a and 15b). The bare NCM showed an initial total impedance of approximately 100Ω , lower than the 300Ω observed for the LiNbO_3 -coated NCM, but it increased more rapidly over time, suggesting that the coating helped



prevent chemical degradation. Upon initial charging, the specific capacities for bare NCM and LiNbO_3 -coated NCM were 247 mA h g^{-1} and 222 mA h g^{-1} , respectively (Fig. 15c). However, after aging, the bare NCM maintained 83% of its initial capacity, while the LiNbO_3 -coated version only saw a 5% decrease (205 mA h g^{-1}), highlighting the coating's effectiveness in maintaining performance. Analysis indicated that the aged bare NCM experienced significant degradation, reducing active sites even at a state of charge (SOC) of 0. In contrast, the coated NCM retained its capacity due to slower chemical reaction kinetics. Secondary ion mass spectrometry (SIMS) analysis confirmed the formation of a thick reaction layer in the bare NCM, primarily consisting of chlorine-based byproducts (Cl , LiCl , and LiCl_2), while the thickness of the interface for the LiNbO_3 -coated NCM remained relatively unchanged (Figs. 15d and 15e).²⁵

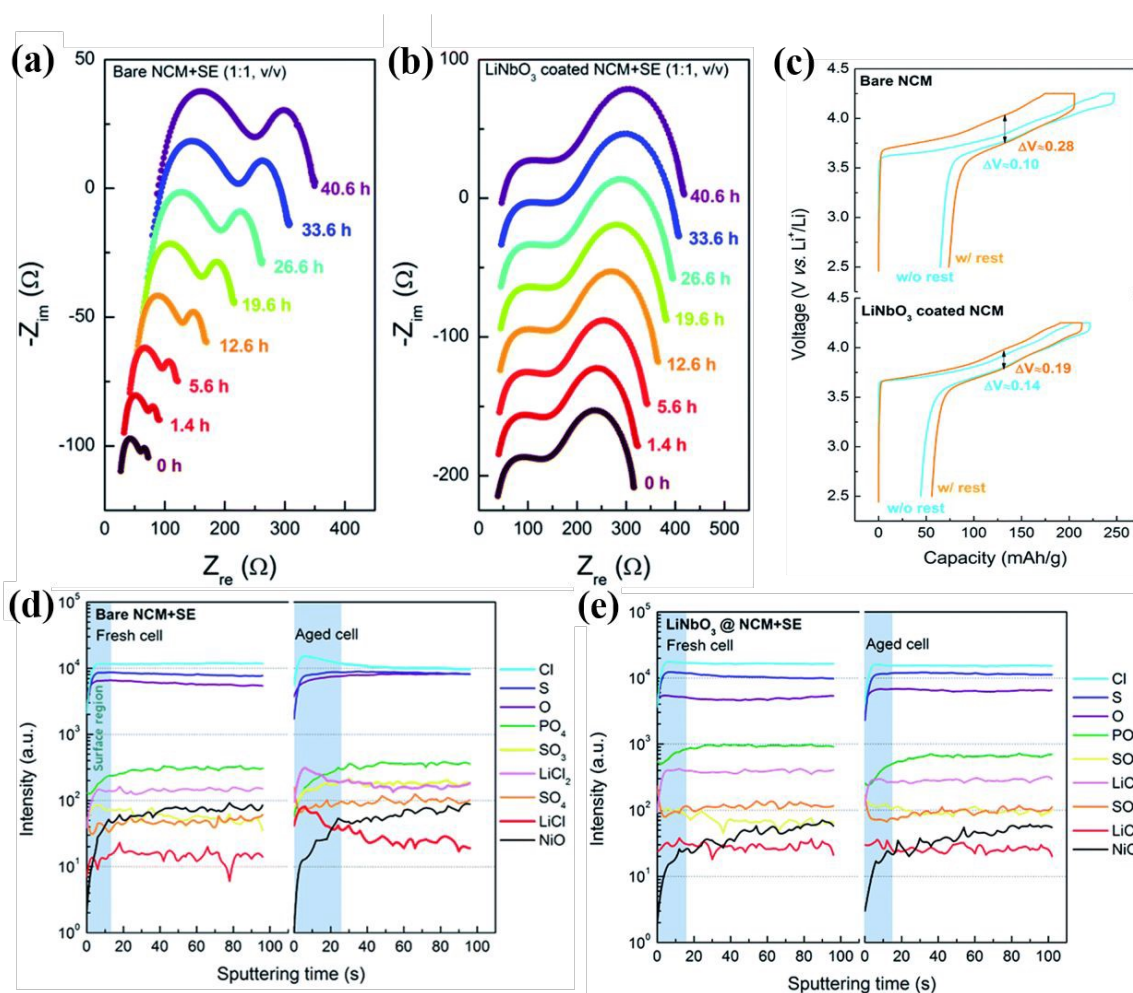


Fig. 15 Chemical and electrochemical performance of bare and coated NCM. Chemical decomposition between the cathode and SE at the steady state. (a and b) EIS spectra of the uncoated bare NCM or LiNbO_3 -coated NCM with the argyrodite SE. Impacts of chemical instability at the cathode-SE interface on electrochemical performance. (c) Electrochemical



performance of the first cycle for both a fresh cell (without rest) and an aged cell (with rest), with charge and discharge CDs of 16 and 7 mA g⁻¹, respectively. TOF-SIMS profiles as a function of sputtering time of fresh (left) and aged cells (right) of (d) bare NCM and (e) LiNbO₃-coated NCM composite pellet.²⁵

In general, coatings help mitigate surface-related degradation issues in layered transition metal oxides (LTMOs), while dopants are primarily used to enhance structural integrity by reducing irreversible phase changes during cycling. Additionally, they can improve rate capability by enhancing electronic and σ , which results from expanded lithium diffusion channels and defect formation that lowers polarization resistances.²⁶⁵ In certain instances, dopants within LTMOs containing greater Ni amount can further increase σ by decreasing the number of unwanted defects (like Ni_{Li}). This suppresses oxygen releases due to stronger M–O bonding energy.²⁶⁶ High-valence ions are commonly utilized to enhance the stability of nickel-rich LTMO cathodes.^{267, 268} These ions typically occupy transition metal sites and raise the repulsive forces between interlayers.²⁶⁹ Compared to smaller ions like Ni³⁺, Mn⁴⁺, and Co³⁺ (0.53–0.56 Å), high-valence dopants are generally larger, which can enhance Li layer spacing and lattice parameters, thereby improving Li diffusion. Moreover, they form stronger M–O bondings that contribute to the stability of the layered structures upon cycling processes.

For comparison, Xu et al. examined how coating and doping of NCM622 affects battery performance.²⁷⁰ The authors claimed that the coating significantly lowers electrochemical impedance and enhances battery cycling performances. The doping ions minimize the mixing of Ni²⁺ and Li⁺ in the NCM622 cathode material, facilitating Li⁺ diffusion and thereby increasing the stability of the cathode while preventing structural damage to NCM622 during charging and discharging cycles.



3.2. Modified electrolyte by doping

View Article Online
DOI: 10.1039/D5EB00101C

3.2.1 Interfacial stability of cation-doped $\text{Li}_6\text{PS}_5\text{X}$ ($\text{X} = \text{Cl}, \text{Br}, \text{I}$) for lithium anode

Because of the strong reducing tendency of lithium metal, all sulfide-based SEs can be reduced by lithium metal during electrochemical cycling or even upon contact (as shown in Fig. 16a).^{119, 271} Zhu et al. conducted computational simulations that established the reduction potential of $\text{Li}_6\text{PS}_5\text{Cl}$ SEs at 1.71 V (vs. Li/Li^+) and identified the reduction products at the $\text{Li}/\text{Li}_6\text{PS}_5\text{Cl}$ interface as P, Li_2S , and LiCl ²⁹, which was later confirmed experimentally by Wenzel et al. in 2018³¹.

Doping is a useful approach for improving the compatibility of electrolyte/electrode interfaces.²⁷²⁻²⁷⁵ Recently, yttrium ions (Y^{3+}) were introduced as dopants to replace phosphorus (P^{5+}) in $\text{Li}_6\text{PS}_5\text{Cl}$, enhancing interfacial stability against lithium metal and inhibiting dendrite growth.²⁷⁶ Indium-doped $\text{Li}_6\text{PS}_5\text{I}$ ($\text{Li}_{6.5}\text{In}_{0.25}\text{P}_{0.75}\text{S}_5\text{I}$) has shown improved interfacial stability compared to its pristine form.²⁷⁷

The Sun group demonstrated that a $\text{Li}/\text{Li}_{6.2}\text{P}_{0.8}\text{Sn}_{0.2}\text{S}_5\text{I}/\text{Li}$ symmetric cell could achieve ultra-stable lithium plating and stripping for over 700 hours (350 cycles) at 0.1 mA cm^{-2} and 0.1 mAh cm^{-2} via ambient temperature. However, significant fluctuations and increasing overpotential suggested subpar kinetics at the $\text{Li}/\text{Li}_6\text{PS}_5\text{I}$ interface.²⁶ Meanwhile, Nazar's group reported that $\text{Li}_{6.7}\text{Si}_{0.7}\text{Sb}_{0.3}\text{S}_5\text{I}$ exhibits excellent stability with lithium metal, maintaining a steady voltage profile for 600 hours at 0.3 mA cm^{-2} and for 1000 hours at a higher CD of 0.6 mA cm^{-2} . Their findings indicated that a stable interphase formed between lithium metal and $\text{Li}_{6.7}\text{Si}_{0.7}\text{Sb}_{0.3}\text{S}_5\text{I}$, which is promising for developing long-lasting ASSLMBs.²⁷⁸

Using cation-doped Li-argyrodites rather than undoped versions may be beneficial, as these substitutions can facilitate the formation of a lithium-metal alloy (Li-M) at the interface (see Fig. 16b).²³ The Li-M alloy could promote uniform lithium deposition and enhance cycling longevity. Additionally, cation substitution may influence these materials' thermodynamic and kinetic stability, ultimately affecting the battery's long-term performance.

Furthermore, due to the rigid nature of SEs, voids, and cracks are observed on the surface of solid electrolytes during pelletizing or battery assembly. This void and crack formation promotes the fast development of dendrite, which reduces the lifetime of the battery (Fig. 17a). However, doping of liquid metal to SE wets the gaps between the electrolyte particles as well as the gaps between the electrode and electrolyte as the physical contact is expected for solid-solid interfaces in ASSBs. This avoids the formation of voids and cracks on the surface of the



electrolyte and prevents dendrite formation (Fig. 17b). In addition, incorporating liquid metal as a dopant reduces Young's modulus, helping to prevent early short-circuit formation in the battery. The presence of liquid dopant allows the formation of M-Li alloy, which is critical in facilitating uniform Li deposition at the interface and leads to outstanding long-term stable cycling (Fig. 17c). Furthermore, doping of liquid metal can boost the mechanical properties of SEs by enhancing wettability and sealing any voids and cracks (Fig. 17d).

Apart from this, due to its unique rheological and metallic properties, low-melting point liquid metal has seen growing applications in thermal control processes.²⁷⁹⁻²⁸³

3.2.2 Interfacial stability of cation-doped $\text{Li}_6\text{PS}_5\text{X}$ (X = Cl, Br, I) towards cathode materials

Sulfide-based SEs, as discussed above, play a crucial role in ASSBs because their high σ , intrinsic softness that facilitates good contact between electrode and SE, and robust mechanical properties.^{284, 285} However, the interfacial stability between electrode materials and sulfide SEs is often poor, which adversely affects battery performance.^{9, 17, 286} The degradation of the interfaces between cathodes and sulfide-based SEs has been identified as a significant contributor to battery failure, using various methods such as electrochemical impedance analysis,^{25, 35, 287-289} macroscopic measurements,^{31, 42, 290, 291} and AIMD simulation.^{290, 292-294} Our research team has also performed macroscopic and microscopic investigations that reveal degradation at the LiFePO_4 and $\text{Li}_6\text{PS}_5\text{Cl}$ interface, resulting in products like FeS , $\text{Li}_2\text{FeP}_2\text{O}_7$, and LiCl . DFT calculations further confirmed these continuous decomposition reactions.²⁴ To tackle these challenges, researchers have proposed doping Li-argyrodites to modify the composition of SEs and enhance interfacial stability.^{6, 272, 295-298}

3.2.2.1 Interfacial stability of cation-doped $\text{Li}_6\text{PS}_5\text{X}$ (X = Cl, Br, I) towards the sulfur cathode

Jiang et al. conducted a study using a sulfur cathode to evaluate the effectiveness of the $\text{Li}_{5.6}\text{Cu}_{0.2}\text{PS}_{4.8}\text{Br}_{1.2}$ SE.²⁹⁹ They reported that this sulfur cathode achieved an impressive initial discharge capacity of 931 mAh g^{-1} at a rate of 0.05 C , along with strong cycle stability, retaining 83% of its capacity after 100 cycles at 0.1 C . In contrast, a full-cell configuration using $\text{S}/\text{Li}_6\text{PS}_5\text{Br}/\text{Li}$ exhibited a notable voltage polarization and a lower discharge capacity of 851 mAh g^{-1} at the same rate. The researchers attributed the reduced discharge capacity of the $\text{Li}_6\text{PS}_5\text{Br}$ to its lower σ compared to $\text{Li}_{5.6}\text{Cu}_{0.2}\text{PS}_{4.8}\text{Br}_{1.2}$. Furthermore, the $\text{S}/\text{Li}_6\text{PS}_5\text{Br}/\text{Li}$ setup experienced a soft short circuit during the 20th cycle, primarily due to poor interfacial compatibility with the sulfur cathode, which negatively affected its cycle performance. The



$\text{Li}_{5.6}\text{Cu}_{0.2}\text{PS}_{4.8}\text{Br}_{1.2}$ demonstrated excellent rate capability, recovering to 810 mAh g^{-1} when the CD was adjusted back to 0.1 C. However, during rate capability testing, a short circuit was also observed in the S/ $\text{Li}_6\text{PS}_5\text{Br}$ /Li configuration. These results indicate that $\text{Li}_{5.6}\text{Cu}_{0.2}\text{PS}_{4.8}\text{Br}_{1.2}$ is highly stable when paired with the sulfur cathode, suggesting its potential for future applications in Li-S batteries.

3.2.2.2 Interfacial stability of cation-doped $\text{Li}_6\text{PS}_5\text{X}$ (X = Cl, Br, I) towards layered oxide cathodes

Layered oxide cathodes are strong contenders for high-capacity, high-energy-density applications in advanced LIBs. However, integrating these cathodes with sulfide-based ASSLMs presents challenges. Increasing the upper cutoff voltage for layered oxide cathodes can enhance their capacity but may lead to material degradation due to processes such as oxygen loss and cracking. This degradation can cause parasitic interactions at the interface with $\text{Li}_6\text{PS}_5\text{X}$ (where X = Cl, Br, I), resulting in the formation of ion insulators byproducts like Li_2S , SO_4^{2-} , and PO_4^{3-} (see Fig. 16c). Understanding these mechanisms is essential for enabling high-voltage operation and enhancing the performance of current materials. A promising solution is cation-substituted Li-argyrodite, which can bind strongly with sulfur and prevent oxygen from displacing it (Fig. 16d).

Liu et al. examined $\text{LNO@NCM/Li}_6\text{P}_{0.925}\text{Sb}_{0.075}\text{S}_5\text{Cl/Li}$ cell performance, reporting an initial discharge capacity of 129.9 mAh g^{-1} , which stabilized at 107.4 mAh g^{-1} after 60 cycling, achieving a magnificent capacity retention of 82.6%.²⁷ In contrast, the ASSLB configuration using $\text{Li}_6\text{PS}_5\text{Cl}$ ($\text{LNO@NCM/Li}_6\text{PS}_5\text{Cl/Li}$) showed a significant capacity drop ($116.2 \rightarrow 31.3 \text{ mAh g}^{-1}$) after 60 cycling, resulting in only 26.3% retention. The authors attributed the better performance of $\text{Li}_6\text{P}_{0.925}\text{Sb}_{0.075}\text{S}_5\text{Cl}$ to its superior σ and interfacial stability. EIS revealed that the impedance of $\text{LNO@NCM/Li}_6\text{PS}_5\text{Cl/Li}$ increased sharply after cycling, while $\text{LNO@NCM/Li}_6\text{P}_{0.925}\text{Sb}_{0.075}\text{S}_5\text{Cl/Li}$ showed minimal change, indicating enhanced stability at the interface. Additionally, the rate capability of $\text{Li}_6\text{P}_{0.925}\text{Sb}_{0.075}\text{S}_5\text{Cl}$ configuration was evaluated, with a capacity recovering of 118.6 mAh g^{-1} when the CD returned to 0.2 C, demonstrating its excellent performance.

In addition, Zhao et al. reported on Sn-doped $\text{Li}_6\text{PS}_5\text{I}$ solid electrolytes, achieving a remarkable first-cycle coulombic efficiency of 91% with a capacity of 123.7 mAh g^{-1} in their Li/LPSI-20Sn//LGPS//LCO@LNO//LGPS setup. They attributed this high efficiency to the enhanced interfacial stability of LPSI-20Sn.²⁶



For practical solid-state battery applications, thick electrode designs are essential to maximize energy density.³⁰⁰⁻³⁰² Zeier's group developed thick cathodes (160 micrometers) and anodes (160 micrometers) using $\text{Li}_{6.6}\text{P}_{0.4}\text{Ge}_{0.6}\text{S}_5\text{I}$ solid electrolyte (450 micrometers).³⁰³ Their findings revealed that this configuration delivered an initial charging capacity of 120.8 mAh g^{-1} and an initial discharge capacity of 88.8 mAh g^{-1} at 0.25 C via 60°C .^{35, 288, 304} Notably, the cell operated stably over 50 cycles without carbon additives,²⁸⁹ exhibiting minimal capacity fade and high coulombic efficiency even after 1 C . The total resistance of the cell remained below $13 \Omega \text{ cm}^{-2}$ at 60°C , attributed to the outstanding interfacial compatibility between $\text{Li}_{6.6}\text{P}_{0.4}\text{Ge}_{0.6}\text{S}_5\text{I}$ and NCM-622. The researchers concluded that employing excellent ionic conductor sulfide SEs combined with effective interphase formation results in superior battery performance.

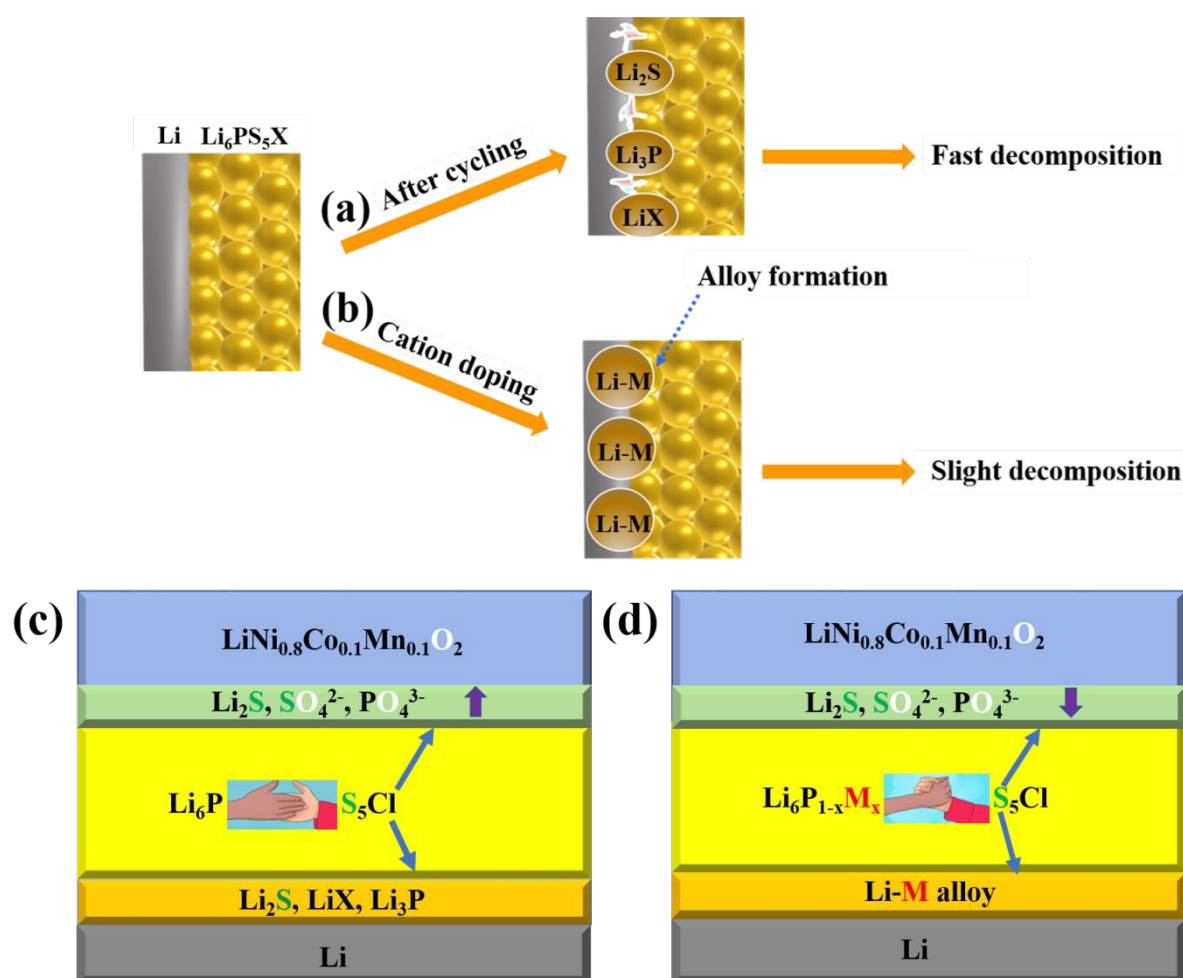


Fig. 16 Scheme illustrating the role of cation-substituted $\text{Li}_6\text{PS}_5\text{X}$ (X = Cl, Br, I) SEs. Anode side interface: (a) bare and (b) cation-doped SEs towards Li metal after cycling. Cathode side



interface: (c) bare and (d) cation-doped electrolyte with layered oxide cathode materials after cycling.

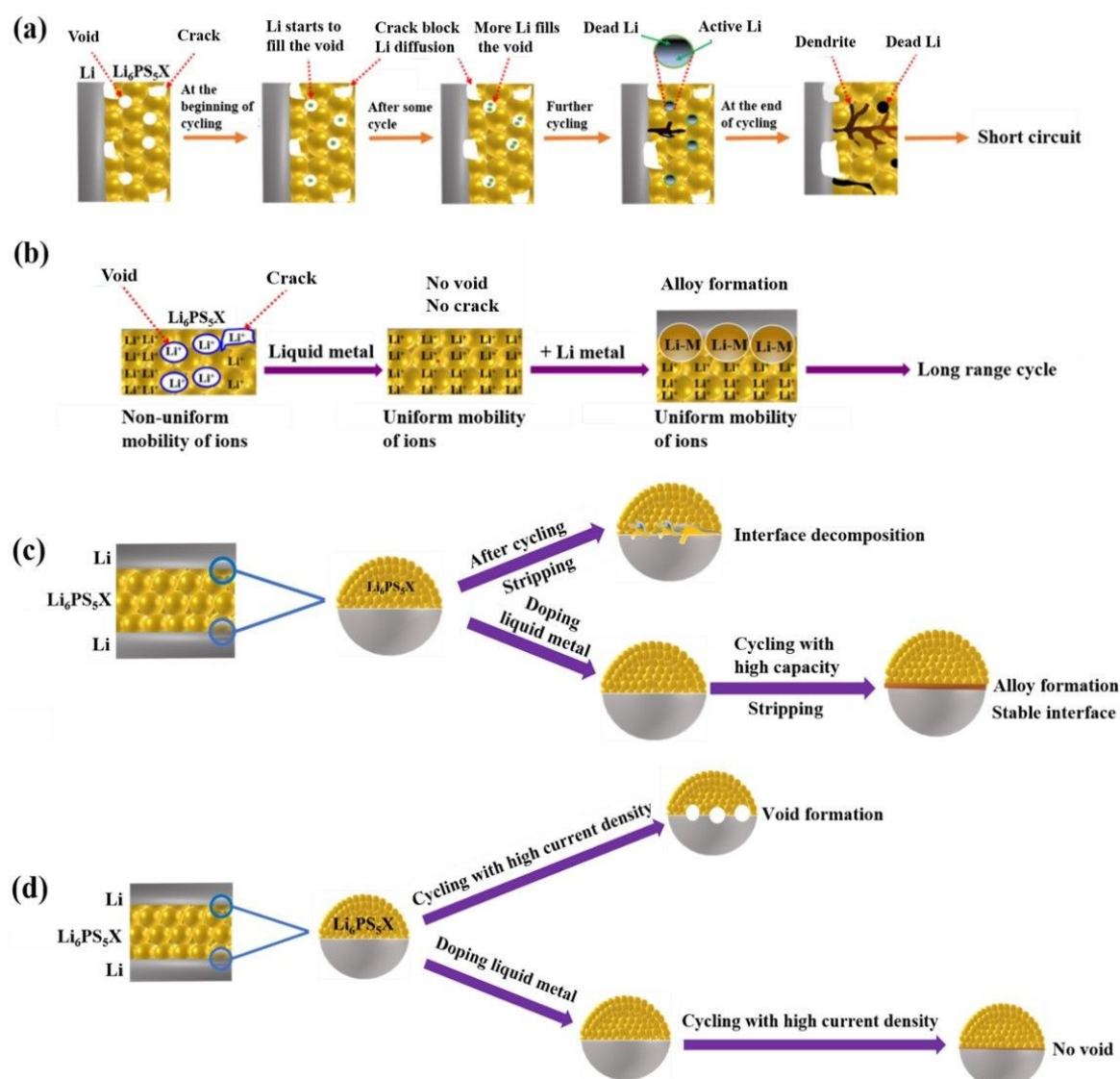


Fig. 17 (a) Mechanism for the formation of a short circuit at the Li/Li-argyrodites interfaces. (b) A suggested pathway to prevent dendrite growth at the Li/Li-argyrodites interfaces via liquid metal dopant. The role of liquid metal dopant for cycling with (c) high capacity and (d) high current density.

3.2.3 Thermal stability of cation-doped Li₆PS₅X (X = Cl, Br, I)

Otoyama et al. investigated the thermal stability of sulfide SEs Li₃PS₄ and LiSnS₄ toward oxide-positive electrode materials.³⁰⁵ They assessed that the side reactions occur at the electrolyte-electrode interfaces when the composite electrodes are heated in an accelerated



aging test. Their findings indicated that the Sn-containing LiSnS_4 SE demonstrated superior thermal stability due to the reduced substitution reactions between sulfur and oxygen (see Fig. 18). Additionally, thermally stable sulfide SEs facilitate enhanced cell construction processes. The sintering of composite electrodes incorporating Li_4SnS_4 resulted in denser electrodes with improved σ , thus boosting battery performance. Therefore, similar benefits can be expected from using cation-doped Li-argyrodites to enhance the thermal stability of solid electrolytes.

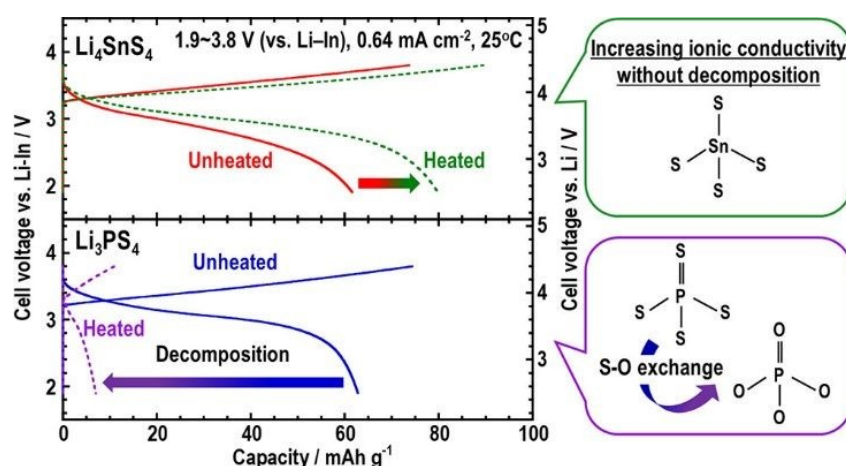


Fig. 18 The role of cation dopant in thermal stability.³⁰⁵

3.3 Multi-layer electrolyte

Luhan et al. developed a multilayer electrolyte system consisting of a less stable electrolyte positioned between two more stable SEs.³⁰⁶ This design effectively inhibits Li dendrite evolution through well-localized decomposition within the less stable layer. They conducted experiments using symmetric cells to evaluate the stability of $\text{Li}_{10}\text{Ge}_1\text{P}_2\text{S}_{12}$ (LGPS) and $\text{Li}_{5.5}\text{PS}_{4.5}\text{Cl}_{1.5}$ (LPSCI) electrolytes in contact with Li metal. The symmetric cell featuring pure Li metal electrodes and LGPS electrolyte demonstrated rapid failure, indicated by a voltage spark (Fig. 19a). While most sulfide SEs experience some level of decomposition upon contact with lithium, the Li-argyrodites $\text{Li}_{6-y}\text{PS}_{5-y}\text{Cl}_{1+y}$ exhibit greater stability in this context compared to LGPS.^{10, 31, 46, 97, 307} In tests, the LPSCI symmetric battery was able to operate for over 150 hours (Fig. 19b) before ultimately experiencing a short circuit. Figs. 19a and 19b illustrate two common failure modes: electrolyte decomposition causing increased overpotential and a sudden voltage drop due to short-circuiting.^{46, 308} XPS analysis revealed significant decomposition of LGPS into reduced sulfur and germanium, while LPSCI showed minimal decomposition, indicating that short-circuiting in the LPSCI battery was likely due to



lithium dendrite penetration. The multilayer electrolyte design provided impressive cycling performance, lasting 1,800 hours at a CD of 0.25 mA cm^{-2} (Fig. 19c), significantly outperforming batteries using a single electrolyte type. Moreover, the multilayer symmetric battery demonstrated the ability to cycle at an exceptionally high CD of 20 mA cm^{-2} with a low overpotential of approximately 0.5 V without noticeable short-circuiting at 55°C (Fig. 19d).

Subha et al. proposed a bilayer SE comprising Li argyrodite LPSCI and halide SEs, in which halide SEs face the cathode, and LPSCI faces the anode.³⁰⁹ When the LPSCI is placed at the cathode side, it aggressively reacts with LCO (Fig. 19e). They noted that the oxidative stability of the halide electrolytes enables their use alongside high-voltage cathodes, addressing the instability of LPSCI under such conditions (Figs. 19f and 19g). Fig. 19h outlines the desired properties of electrolytes used in a multilayer design.

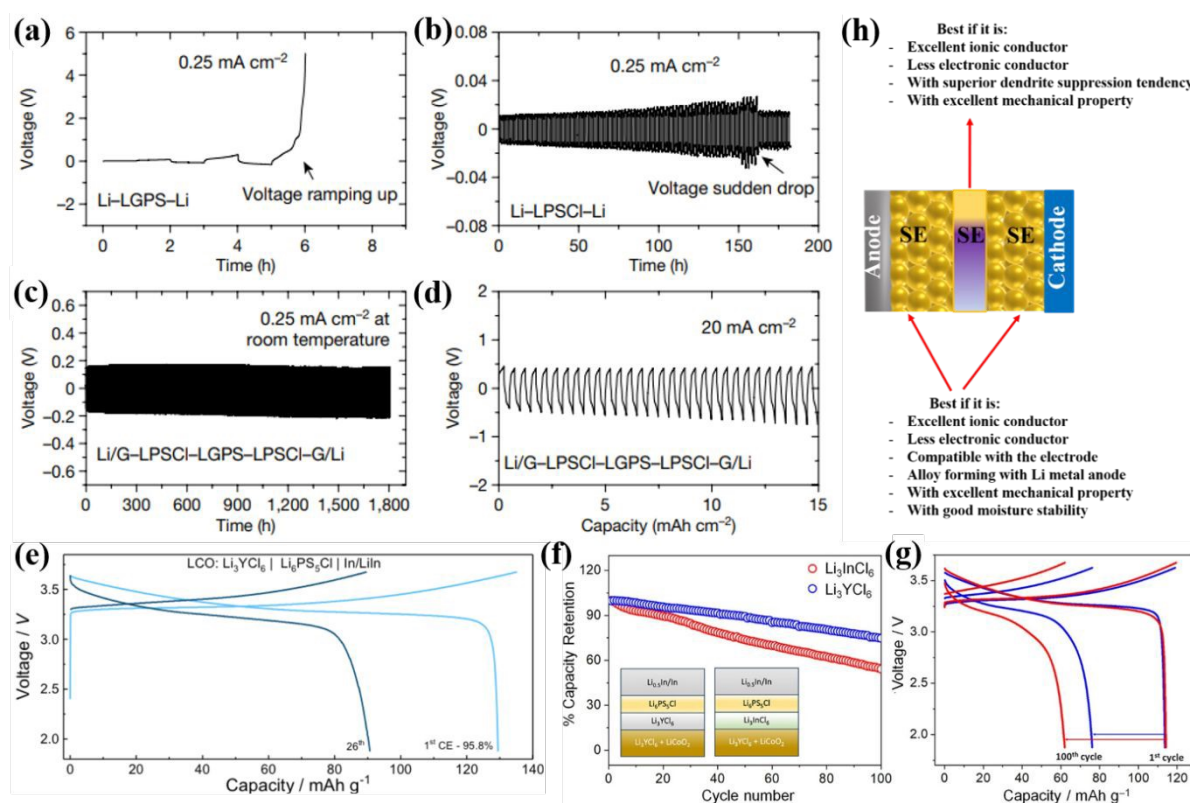


Fig. 19 Designing multi-layer SE. a) and b) Li-Li symmetric cells comprising LGPS and LPSCI SEs, respectively. c) and d) Long cycling using multi-layer SEs.³⁰⁶ e) Charge-discharge profile of LiCoO_2 : Li_3YCl_6 | $\text{Li}_6\text{PS}_5\text{Cl}$ | Li-In at 10 C. f) Capacity retention and g) charge-discharge profile of LiCoO_2 : Li_3YCl_6 | Li_3InCl_6 | $\text{Li}_6\text{PS}_5\text{Cl}$ | Li-In (red) and LiCoO_2 : Li_3YCl_6 | Li_3YCl_6 | $\text{Li}_6\text{PS}_5\text{Cl}$ | Li-In (blue) at 10 C. h) Scheme illustrating the suggested property of electrolyte needed to fulfill in the multi-layer design system.³⁰⁹



4. Techniques for exploring interfaces

The type and characteristics of interfaces in ASSBs are crucial because of the significant impact of contact extent and big charge transfer impedance at these interfaces.³¹⁰⁻³¹² Therefore, to advance the development of next-generation ASSBs that fulfill diverse industrial and consumer needs, it is vital to understand the phenomena of interfacial impedance, which can be studied through advanced characterization techniques that reveal morphological changes and electrochemical processes. While there are established methods for examining LE battery systems, investigating interfacial behavior in ASSBs presents a significant challenge. The interfaces in ASSBs are harder to isolate than those in LE systems. For instance, in LE systems, electrode materials can typically be extracted for post-experimental analysis without causing damage. In contrast, the fabrication of ASSBs often involves techniques like hot-press and chemical or physical evaporation to achieve optimal interfacial contact.³¹³ As a result, these tightly integrated interfaces are not easily accessible without harming their surface conditions, making it challenging to gather critical information regarding interfacial reactions and kinetics, particularly for Li/SE interfaces.⁶² Thus, a new approach, ideally involving in situ measurements, is necessary.³¹⁴ Traditional studies often rely on ex-situ measurements conducted in coin cells. However, interfacial research can also be performed using hybrid cell³¹³, symmetric cell¹⁵¹, or a combination of ex-situ and in situ methods.

The primary challenges in characterizing interfaces in ASSBs include the limited exposed surface area and the sensitivity of these interfaces when extracted for analysis.⁶² As a result, many conventional techniques used for LE interfaces, such as infrared spectroscopy (IR), are not suitable for ASSB interface characterization.³¹⁵ Therefore, characterization methods that offer high measurement accuracy in a narrow area and high protective properties of samples during analysis are available for characterizing the interfaces in ASSBs.

In situ characterization is vital for examining interfacial phenomena in SSBs, as it enables the observation of real-time changes in materials and interfaces during actual operating conditions like charging, discharging, or temperature variations. Unlike ex-situ methods, which assess the system after these changes have occurred, potentially missing or altering transient interfacial states, in situ techniques are ideal for dynamic processes. However, ex-situ approaches still play a key role by offering detailed structural insights (e.g., via TEM, TOF-SIMS), analyzing surface chemistry under ultra-high vacuum conditions (e.g., with XPS), and evaluating bulk properties after extended cycling periods.



Here, we discussed about various characterization techniques such as chemical/electrochemical, diffraction and images.

View Article Online
DOI: 10.1039/D5EB00101C

4.1 Coulometric titration time analysis (CTTA)

The CTTA method is effective for quantitatively analyzing decomposition reactions between Li and argyrodite electrolytes, offering valuable insights into electrolyte stability.³¹⁶ This versatile approach can also be applied to various electrodes and allows for the investigation of how key operational factors, such as temperature and CD, affect the characteristics of the SEI and cell degradation.

Burak et al.³¹⁶ developed the CCTA technique to quantify side reactions that occur between redox-active electrode material and SE. Fig. 20 displays the results from a CTTA measurement. In an ideal scenario, where the electrolyte is stable, and no decomposition reaction occur, the cell potential would rapidly stabilize at $E = 0$ V after a period, as Li dictates the potential of both the working and counter electrodes, achieving a symmetric cell stage. This would result in an infinite potential at $E = 0$ V. However, if the SE is unstable and a decomposition reaction take place, these unwanted reactions gradually consume the lithium metal that has been ‘titrated’. As long as some Li remains at the working electrode, the potential stays at $E = 0$ V. Eventually, once all the lithium metal is depleted, the potential at the working electrode becomes variable, leading to an increase in cell voltage. In LPSCl solid electrolyte, the rise in potential happens swiftly after the initial titration step (Fig. 20b). When the potential hits 0.05 V, an identical titration step is performed (marked in gray), resulting in the cell voltage dropping back below $E = 0$ V as fresh lithium is accumulated on the current collector. During the subsequent OCV period, it is observed that the time taken to consume all Li was greater than during the preceding OCV period, indicating a reduced rate of side reactions following the second titration step. As illustrated in Fig. 20c, the consumption of a similar extent of Li metal takes progressively longer as the measurement continues, suggesting that side reaction products form a passivating SEI layer. Fig. 20d presents the total charge used for side reactions ($q_{\Sigma} = \Sigma q(\tau_i)$, where the total is the number of titrations multiplied by the step charge) in relation to the duration of the experiment, enabling precise quantification of SEI growth over time. Fig. 20e indicates that this growth exhibits a linear relationship with the square root of time. For LPSCl, a charge of $1 \mu\text{Ah cm}^{-2}$ (approximately $3.7 \times 10^{-8} \text{ mol cm}^{-2} \text{ Li}$) leads to an SEI thickness of about 9 nm, supposing a compact mixture of Li_2S , LiCl , and Li_3P , without any gaseous byproducts.



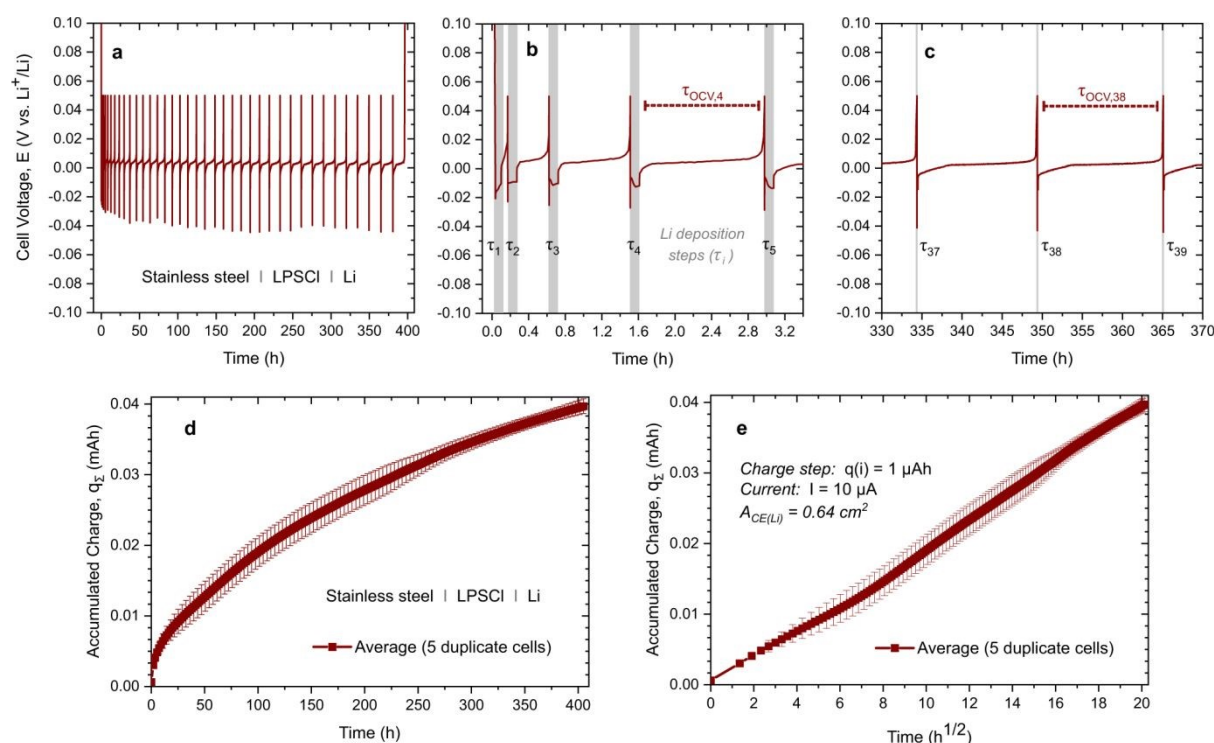


Fig. 20 CTTA measurements. a) Output for the LPSCI SE in a stainless steel/LPSCI/Li assembly at a temperature of 25 °C and pressure of approximately 13 MPa. The potential profiles are depicted for two distinct time intervals: an early stage (b) and a later stage (c) of the measurement. The total stored capacity over time is illustrated in (d) as a function of time and (e) as a function of the square root of time.³¹⁶

4.2 X-Ray Photoelectron Spectroscopy

XPS is a well-established method for chemical analysis³¹⁷, particularly effective in examining the composition of interfaces in ASSBs. It offers high sensitivity, accuracy, resolution, and the ability to test various elements across the periodic table. This makes XPS especially valuable for obtaining valence band spectra, which are crucial for analyzing the electronic structure of surfaces and interfaces in these systems. The SE/electrode interfaces are vital in ASSB, yet ex-situ XPS fails to accurately capture these interfaces' chemical and electronic properties. In situ measurements are possible by connecting an ultrahigh vacuum transfer system to the XPS chamber³¹⁸, allowing for real-time analysis of interfacial properties during electrode deposition. Wood et al.¹¹⁷ utilized in situ XPS to investigate the interphase between lithium and sulfide solid electrolyte during electrochemical cycling, finding that a Li_3PO_4 phase forms



initially through phase segregation of $\text{Li}_3\text{PO}_x\text{S}_{4-x}$ and then evolves further (Li_{3-x}P and Li_2O) during discharge.

Burak et al.³¹⁹ conducted operando hard X-ray photoelectron spectroscopy (HAXPES) study on a sulfide-based SE, $\text{Li}_6\text{PS}_5\text{Cl}$, to examine its reduction reactions during lithiation and the resulting development of SEI. As illustrated in Figs. 21a–21d, the surface of the solid electrolyte pellet is coated with a 6 nm layer of nickel, which serves as both a CC and a working electrode (WE). Li metal is pressed in place on the pellet's opposite side, functioning as a counter electrode (CE) and a reference electrode (RE). This setup is termed an "anode-free" configuration due to the absence of an initial lithium reservoir in a specialized holder connected to a potentiostat. This arrangement allows for the gradual polarization of the WE to specific potentials, eventually leading to the electrochemical plating of lithium metal below 0 V vs Li^+/Li . Utilizing the high photon energies from a synchrotron source enables the detection of higher kinetic energy electrons, essential for analyzing the Ni|LPSCl interface beneath the 6 nm nickel layer within a proper timeframe. This methodology permits investigating the SEI formed beneath a thin metal film, like the 6 nm nickel, in an electrochemical cell incorporating the $\text{Li}_6\text{PS}_5\text{Cl}$ SE. The electrolyte begins to undergo reduction reactions at 1.75 V (vs Li^+/Li), leading to the significant formation of Li_2S , particularly within the voltage range of 1.5–1.0 V. A heterogeneous and layered microstructure of the SEI is noted, with Li_2O and Li_2S deposits primarily found near the CC. Additionally, the study reveals the reversibility of decomposition products as Li_2O and Li_2S degrade within the 2–4 V potential range, producing oxidized sulfur species, sulfites, and sulfates.

Additionally, Zhang et al. employed complementary in situ approaches, including atomic force microscopy (AFM) and XPS, to directly observe the morphological and chemical changes, Li plating and stripping processes, and SEI dynamics at the Li and sulfide SE interface.³²⁰ The morphology at the open circuit potential (OCP) was first analyzed using AFM (Fig. 22a). At the same time, XPS was employed to identify the functional groups present in LPS (Fig. 22g). After applying a discharge overpotential (0.1 V) for approximately 240 seconds, small particles began to show on the Li metal surface, as designated by the white arrows in Fig. 22b. After 600 seconds of Li plating, a few isolated particles were observed on the Li metal surface (Fig. 22c). In addition to morphological alterations, the chemical evolution at the Li-SE interface during the Li plating process was investigated using in situ XPS (Fig. 22g). The emergence and increased intensity of signals corresponding to Li_2S , Li_xP , and Li_3P reveal the formation of SEI containing these components, which occurs concurrently with the Li plating process.



An over-potential of 0.1 V was applied to investigate the Li stripping processes. As indicated in Figs. 22d–22e, the Li spheres began to dissolve upon application of the stripping potential. After 600 seconds of stripping, most of the deposited Li spheres had dissolved, leaving wrinkles at the sites where dissolution occurred (Fig. 22f). Analysis of the primary XPS signals for Li_2S , Li_xP , and Li_3P (Fig. 22g) indicated that these residual wrinkles were primarily due to the SEI present at the interface. The detailed Li plating and stripping processes were elucidated through in situ AFM and in situ XPS analyses. This approach allowed for a detailed examination of the morphological/chemical changes of the SEI. The findings indicate that the presence of the SEI, characterized by limited electron-conducting properties, plays a vital role in sustaining the interfacial stability of LPS. The dynamics of lithium plating/stripping within the LPS system were analyzed by examining the Li volumes derived from in situ AFM images. Fig. 22h shows the changes in Li volume throughout the plating and stripping processes, with the Li plating rate in the LPS system determined to be $0.15 \mu\text{m}^3/\text{s}$. Simultaneously, the evolution of species containing sulfur and phosphorus was investigated through quantitative analysis of in situ XPS spectra, as depicted in Figs. 22i and 22j, respectively. The authors concluded that the rate of lithium plating is not directly linked to the rate of SE decomposition or SEI formation.

Despite the advantages of in situ XPS for monitoring electrochemical reactions at ASSB interfaces, relevant studies remain limited. Integrating the charge/discharge testing apparatus with XPS equipment is a key challenge. Additionally, the electrode thickness required for in situ tests must be nanoscale, complicating the application of common coating methods.³²¹ Therefore, effectively designing ASSBs compatible with XPS technology is essential for advancing in situ XPS applications.



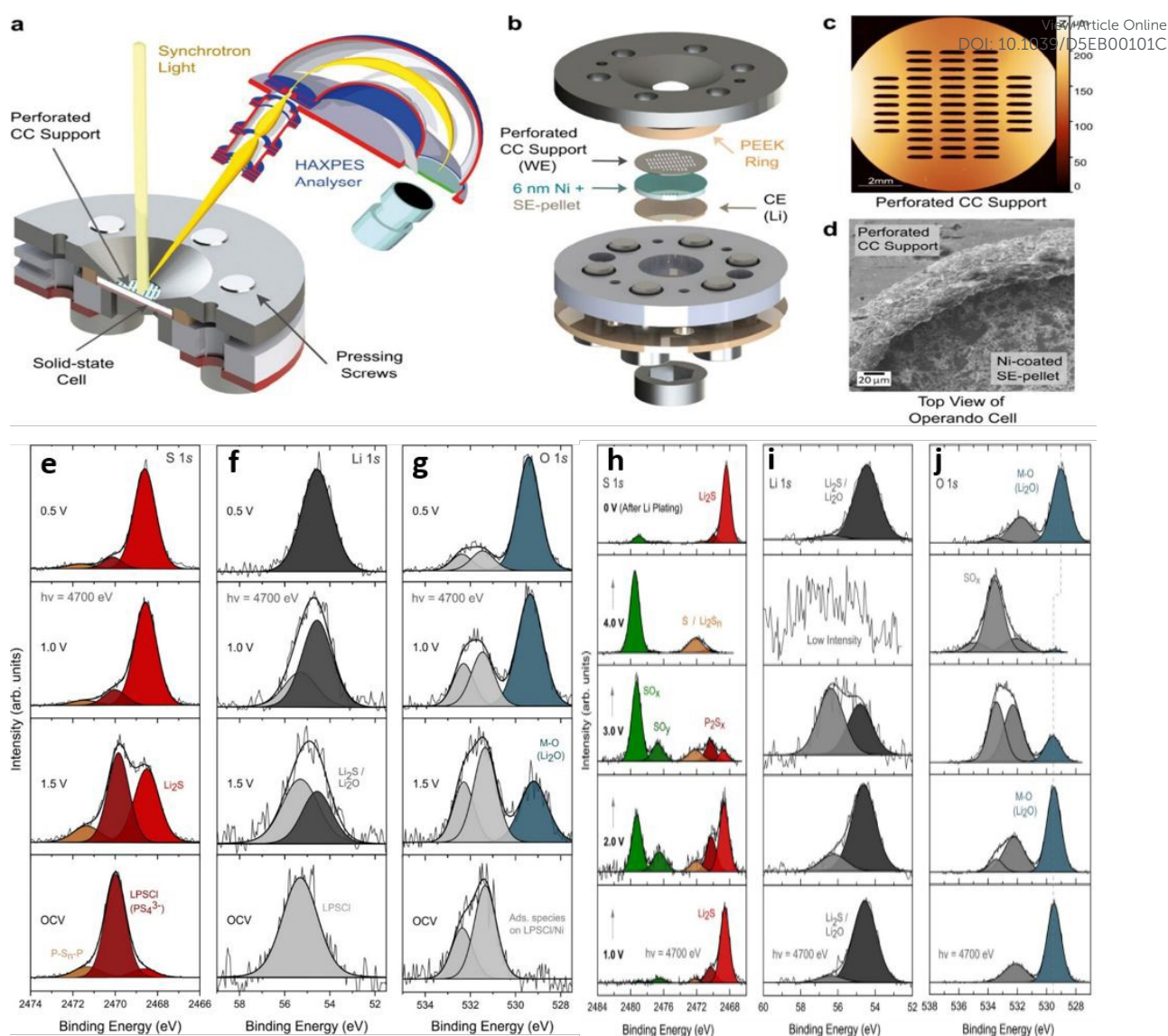


Fig. 21 (a) Scheme illustrating the operando HAXPES experiment setup. (b) An enlarged view of the operando cell. (c) A confocal microscope image showing the Ni-coated stainless steel perforated CC support. (d) A top-down SEM image of the operando cell. The normalized HAXPES spectra, including peak fittings at various working electrode potentials, are presented for (e) S 1s, (f) Li 1s, and (g) O 1s core levels. Normalized HAXPES detailed spectra change during polarization to elevated potentials, with peak fittings for (h) S 1s, (i) Li 1s, and (j) O 1s core levels.³¹⁹



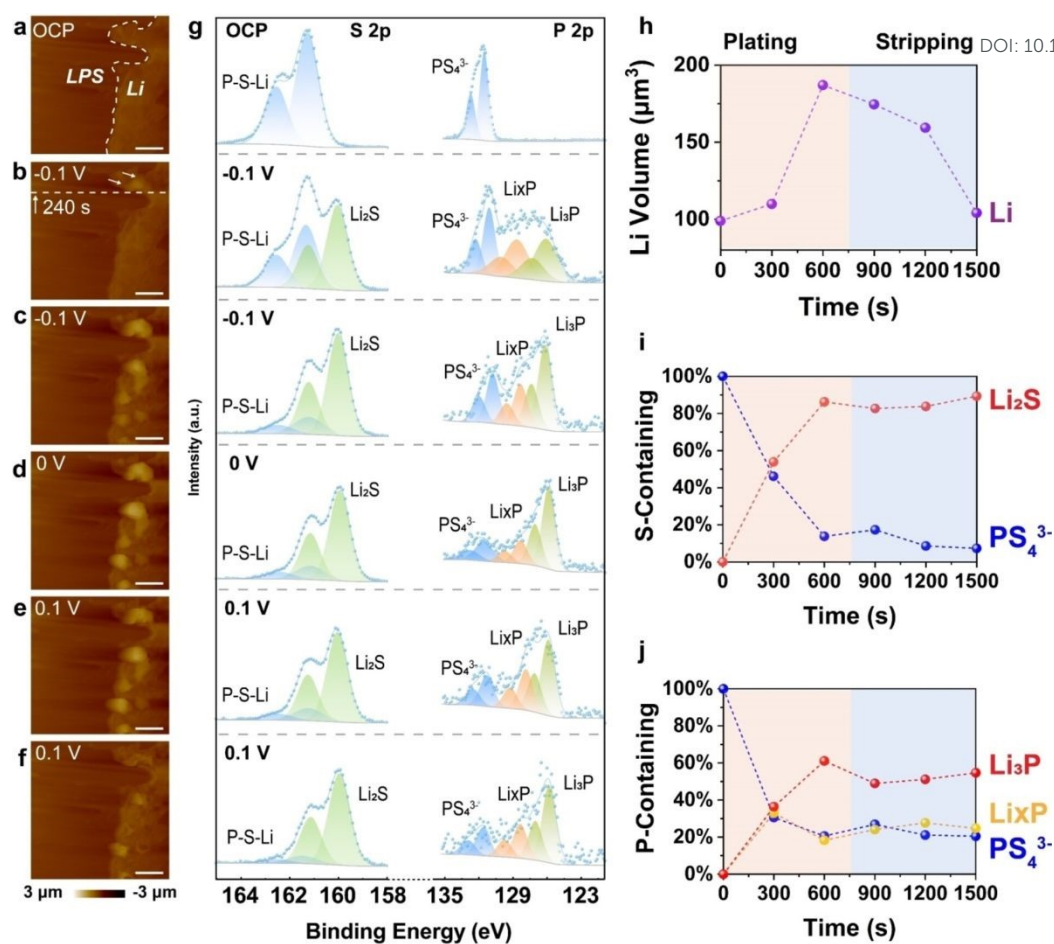


Fig. 22 *In situ* studies of the morphological/chemical evolution and dynamics at the lithium and sulfide SE interface. *In situ* AFM images of the lithium and LPS interface captured at various potentials: (a) OCP, (b–c) cathodic -0.1 V, (d) 0 V, (e–f) anodic 0.1 V. (g) *In situ* XPS spectra of the lithium and LPS interface at different potentials. Each AFM image's capture time and the XPS spectrum collection is 300 s. (h) The Li volume alterations during lithium plating/stripping. (i) Changes of the S-containing species during lithium plating/stripping. (j) Alterations of the P-containing species during Li plating and stripping.³²⁰

4.3 Raman spectroscopy

The Raman technique is a valuable tool for investigating various organic and inorganic compounds at the interfaces of ASSBs, thanks to its suitability, greater accuracy, and undestructive nature.^{322, 323} Li et al.³²⁴ verified that decomposition reaction occurs at the interface between Ni-rich cathodes and sulfide SEs. At the same time, a Ni-poor coating layer can mitigate these reactions. Raman spectroscopy also illustrated the structural alterations of the $\text{P}_4\text{S}_{16}/\text{C}$ cathode during lithiation and delithiation, indicating the formation of Li_xPS_4 and



PS_4^{3-} species during lithiation, while the P–S characteristic peak returned without observing P=S bonds after delithiation.³²⁵

Raman mapping, a derivative of Raman spectroscopy, offers an intuitive view of the phase composition at ASSB interfaces. Luo et al. analyzed the surface of In foil after being in contact with $\text{Li}_6\text{PS}_5\text{Cl}$ and compared it with fresh In foil without contact via Raman spectroscopy. The obtained result showed the formation of In_2S_3 after In foil contacted with $\text{Li}_6\text{PS}_5\text{Cl}$ ²⁹². Rui et al. examined the thermal stability of $\text{Li}_6\text{PS}_5\text{Cl}$ and $\text{LiNi}_{0.8}\text{Co}_{0.1}\text{Mn}_{0.1}\text{O}_2$ mixture via Raman spectroscopy¹⁸³. The result indicates the formation of PO_4^{3-} and SO_4^{2-} , Li_2S_x decomposition products at 400–500 °C. Zhou et al. utilized in situ electrochemical Raman microscopy to analyze the interfacial degradation of $\text{Li}_6\text{PS}_5\text{Cl}$ with lithium metal and LiCoO_2 , detecting Li_2S during Li deposition and identifying polysulfides and P_2S_x species at the $\text{Li}_6\text{PS}_5\text{Cl}$ / LiCoO_2 interface during charging (Fig. 23).³²⁶ Zeng et al. compared the stability of $\text{Li}_{6.4}\text{PS}_{5.4}\text{Cl}_{0.6}$ and $\text{Li}_{5.7}\text{PS}_{4.7}\text{Cl}_{1.3}$ towards Li metal via in situ Raman measurement³²⁷. Their results showed that for the $\text{Li}_{6.4}\text{PS}_{5.4}\text{Cl}_{0.6}$ cell, new peaks associated with P_2S_5 and Li_2S_n emerged after charging to 3.6 V, with peak intensities increasing with voltage. In contrast, the $\text{Li}_{5.7}\text{PS}_{4.7}\text{Cl}_{1.3}$ cell did not show decomposition product peaks, and the PS_4^{3-} peak intensity only slightly decreased, indicating a self-limiting interface characteristic for $\text{Li}/\text{Li}_{5.7}\text{PS}_{4.7}\text{Cl}_{1.3}$.

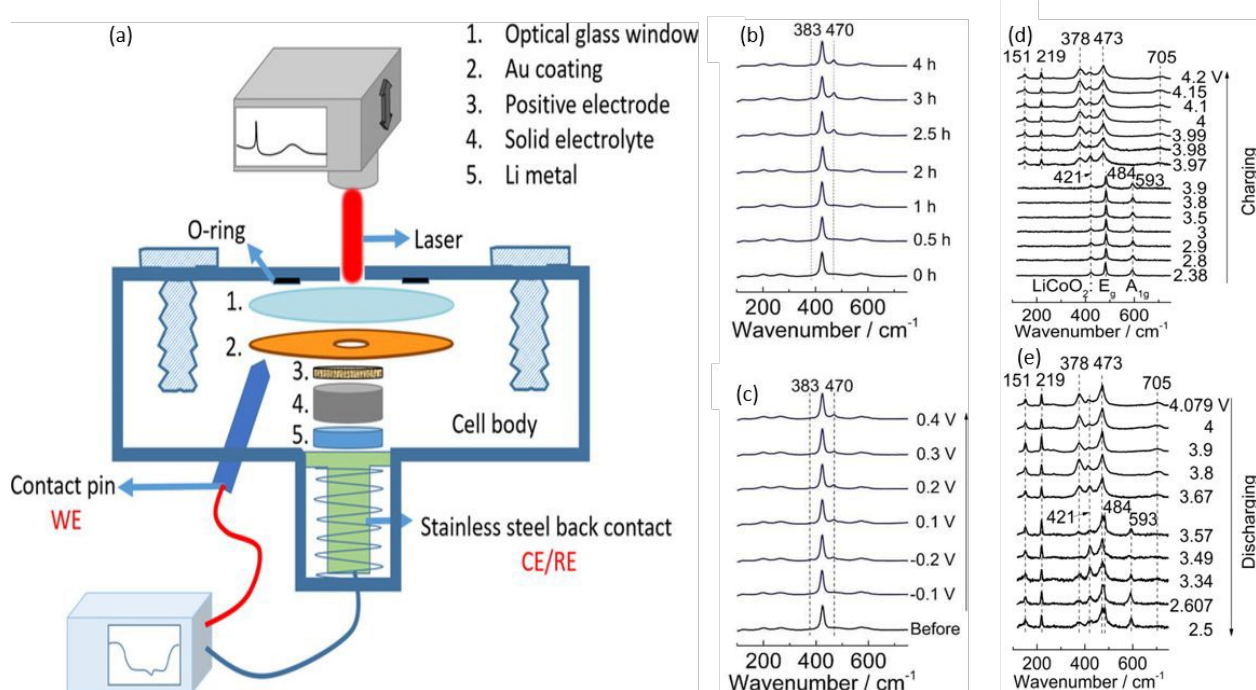


Fig. 23 (a) The diagram illustrates the in situ Raman cell setup. In situ Raman spectra of $\text{Li}_6\text{PS}_5\text{Cl}/\text{Li}$ interface in $\text{Li}/\text{Li}_6\text{PS}_5\text{Cl}/\text{Cu}$ configuration under (b) constant potential of -0.1 V vs



Li⁺/Li; (c) under varying potential. In situ Raman spectra of LiCoO₂/Li₆PS₅Cl interface during (d) charging to 4.2 V and (e) discharging to 2.5 V.³²⁶

4.4 Electrochemical impedance spectroscopy

EIS is a virtual approach for examining the interfacial behavior between electrodes and SEs, providing valuable insights into lithium-ion diffusion in ASSLMs.³²⁸ It has been observed that the interfacial stability and resistance during cycling can be assessed through the changes in the semicircles observed in both low- and high-frequency ranges.³²⁹ Thus, EIS is a valuable technique in electrochemical studies, useful for analyzing materials, complete cell devices, and battery packs.³³⁰ Chaochao et al.³³¹ examined how σ affects the impedance changes in ASSBs during cycling through in situ EIS measurements. As illustrated in Fig. 24a, the bulk impedance of the 3Li₂S–LiI/Li_{5.5}PS_{4.5}Cl_{1.5}/Li–In cell elevated during the initial charging process, with the increment in interfacial resistance attributed to the decomposition of the sulfide solid electrolyte throughout cycling.³³² In Fig. 24b, the 5Li₂S–LiI/Li_{5.5}PS_{4.5}Cl_{1.5}/Li–In cell exhibited similar changes in the resistances at the interfaces of the AM and the SE. However, these resistance amounts were noticeably greater than those observed in the 3Li₂S–LiI/Li_{5.5}PS_{4.5}Cl_{1.5}/Li–In cell during the first cycle, which can be ascribed to the enhanced σ in the cathode mixture following the addition of LiI. Furthermore, Zhang et al. compared the interfacial stabilities of a single sulfide SE with the sandwiched sulfide SE in a Li–Li symmetric configuration via in situ EIS and associated DRT measurements (Figs. 24c–24d). The results demonstrated the advantages of sandwich SEs, revealing reduced resistance and stable interfacial characteristics.³²⁰



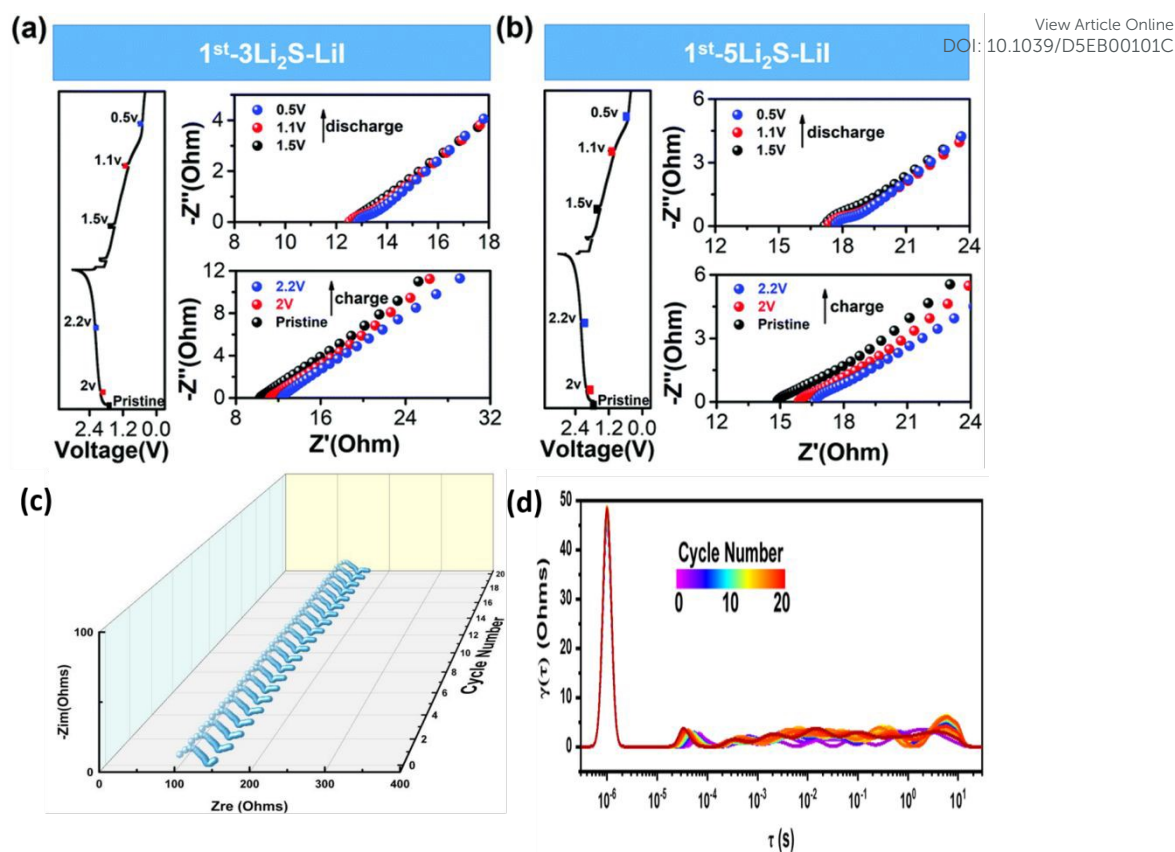


Fig. 24 In situ EIS measurements. In situ EIS performed on Li_{5.5}PS_{4.5}Cl_{1.5}-based ASSBs, utilizing cathode mixtures of 3Li₂S-LiI (a) and 5Li₂S-LiI (b) during the first cycle at a CD of 0.13 mA cm⁻², within a voltage range of 0.4 to 3 V vs. Li-In at ambient temperature.³³¹ c) In situ EIS of Li|LPS-LGPS-LPS|Li cells operated at 0.1 mA cm⁻² and 0.1 mAh cm⁻². d) DRT results from the in situ EIS of Li|LPS-LGPS-LPS|Li cells operated at 0.1 mA cm⁻² and 0.1 mAh cm⁻².³²⁰

4.5 Diffuse reflectance infrared Fourier-transformed spectroscopy

In situ diffuse reflectance infrared Fourier-transform spectroscopy (*in situ* DRIFTS) is a method used to study the intricate changes in surface species of SEs.³³³ Our research team examined the behavior of functional groups and C-S bonding during CO₂ adsorption on Li₆PS₅Cl using *in situ* DRIFTS (Fig. 25).³³⁴ The adsorption of CO₂ facilitated an essential for enhancing both interfacial and electrochemical stability between Li and Li₆PS₅Cl. The emergence of the new S-CO₂ bond is critical for altering interfacial behavior, as it improves interfacial stability between Li and Li₆PS₅Cl while decreasing cell resistance. Furthermore, the Li|CO₂@ Li₆PS₅Cl|LTO configuration demonstrates impressive performance, achieving 62% capacity retention and an extremely high coulombic efficiency of 99.91% after 1000 cycles.



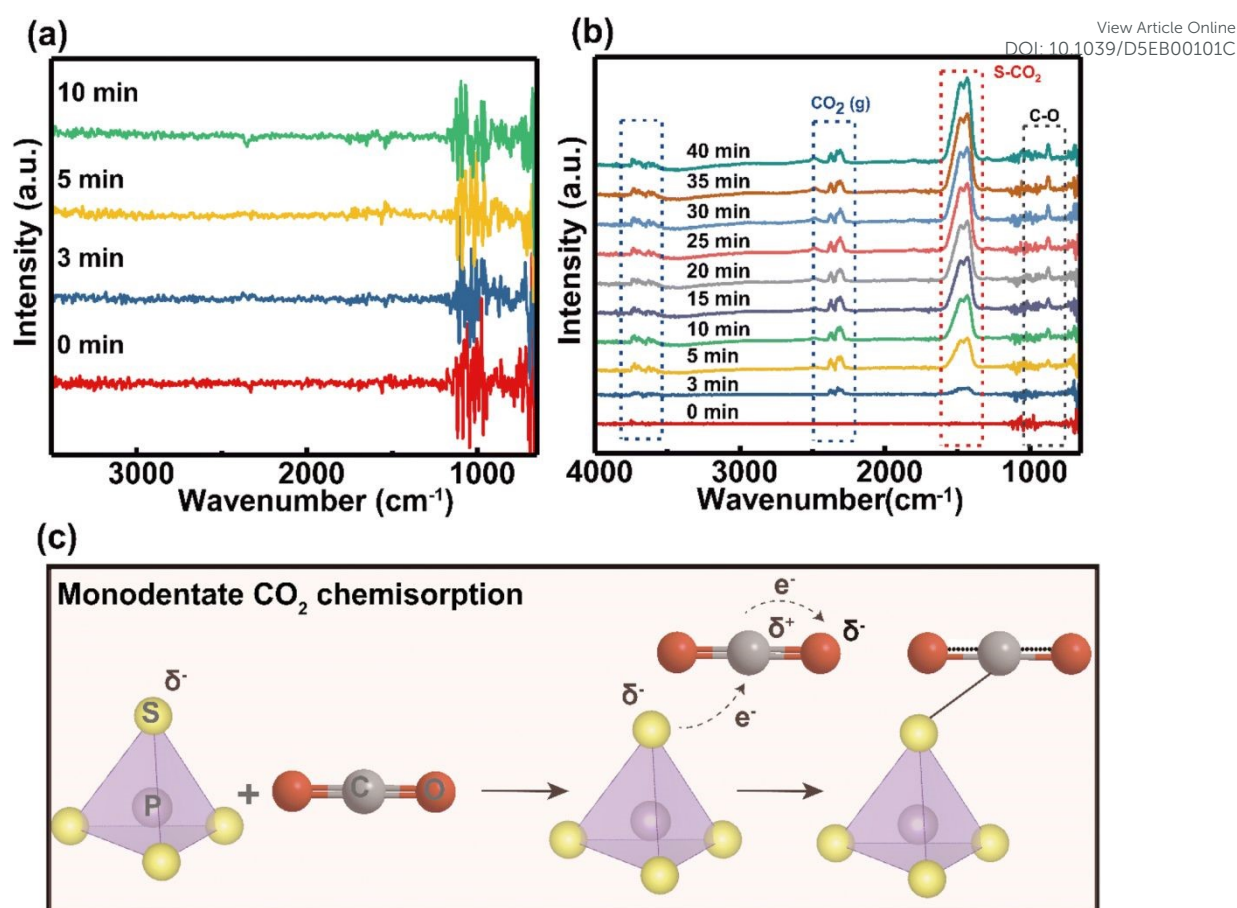


Fig. 25 In situ DRIFTS measurements. The in situ DRIFTS findings of CO₂ adsorption on Li₆PS₅Cl at 150 °C show: (a) the initial condition under Ar purging and (b) the spectral alterations of Li₆PS₅Cl when CO₂ is purged at a rate of 30 c.c. min⁻¹. (c) A depiction of monodentate CO₂ chemisorption on Li₆PS₅Cl is also provided.³³⁴

4.6 Pressure measurements

Yuqi et al.³³⁵ conducted operando pressure measurements to monitor pressure changes in Li_{1.2}Ni_{0.13}Mn_{0.54}Co_{0.13}O₂-based ASSLBs during cycling, aiming to systematically explore the connection between internal stress and electrochemical performance. A zero-strain LTO anode was utilized as the CE, allowing the CAM to dominate the overall pressure changes. Both the polycrystal (PC)- and single crystal (SC)-Li_{1.2}Ni_{0.13}Mn_{0.54}Co_{0.13}O₂ cathodes displayed similar pressure profiles (Fig. 26). The pressure decreased during charging and increased during discharging, indicating high reversibility. This pressure variation primarily results from volume contraction and expansion upon lithium extraction and intercalation from/into the Li_{1.2}Ni_{0.13}Mn_{0.54}Co_{0.13}O₂, respectively.³³⁶ However, it is noteworthy that the pressure fluctuations in PC-Li_{1.2}Ni_{0.13}Mn_{0.54}Co_{0.13}O₂ were less pronounced than those in SC-Li_{1.2}Ni_{0.13}Mn_{0.54}Co_{0.13}O₂. This difference can be attributed to two main factors: first, SC-



$\text{Li}_{1.2}\text{Ni}_{0.13}\text{Mn}_{0.54}\text{Co}_{0.13}\text{O}_2$ provides higher capacities, leading to more significant changes in lithium content and, consequently, more noticeable pressure variations. Second, uneven stress distribution in the PC- $\text{Li}_{1.2}\text{Ni}_{0.13}\text{Mn}_{0.54}\text{Co}_{0.13}\text{O}_2$ cathode can cause structural collapse, forming gaps or voids that can partially accommodate the volume changes associated with electrode breathing.

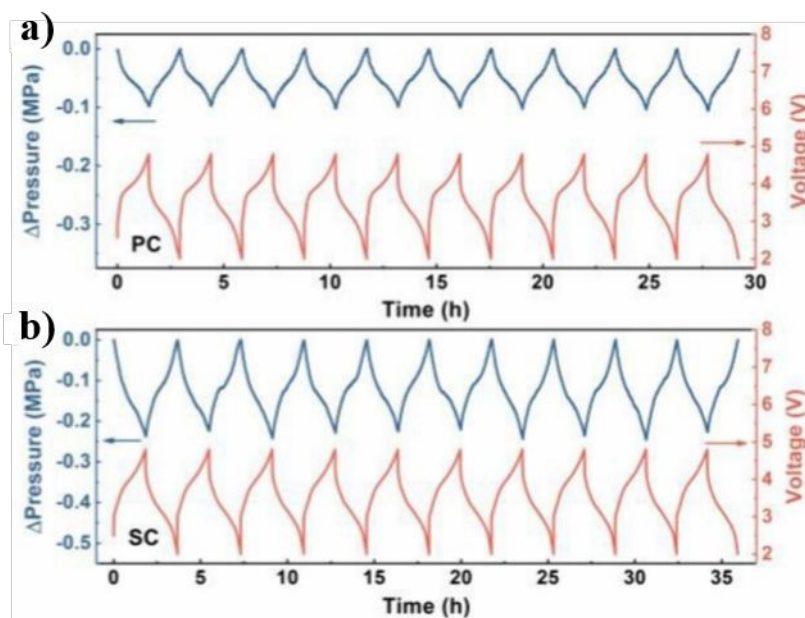


Fig. 26 Operando pressure curves of PC- and SC- $\text{Li}_{1.2}\text{Ni}_{0.13}\text{Mn}_{0.54}\text{Co}_{0.13}\text{O}_2$ in $\text{Li}_4\text{Ti}_5\text{O}_{12}|\text{Li}_6\text{PS}_5\text{Cl}|\text{Li}_{1.2}\text{Ni}_{0.13}\text{Mn}_{0.54}\text{Co}_{0.13}\text{O}_2$ cells.³³⁵

4.7 X-ray diffraction

X-ray diffraction (XRD) is a method used to analyze the structure of crystals. In this technique, an X-ray beam is directed at a sample, which diffracts the rays in various directions due to its crystalline structure. By measuring the angles and intensities of these diffracted beams, crystallographer can create a three-dimensional representation of the electron density within the crystal. This allows for the extraction of information about the crystalline structure, including chemical bonds, crystallographic defects, and atomic distances based on the positions of atoms. XRD is favored as an analytical tool due to its straightforward operation, minimal contamination during detection, and ease of data processing, making it the most widely used method for determining crystalline structures.³³⁷

Hau et al.³³⁸ explored the microstructure of manganese-based cathodes using in situ XRD measurements. They found that the nanoscale domain structure and the little coherence length of partly disordered spinel-like domains are vital for the electrochemical performance of the δ -



phase. These characteristics adequately mitigate the two-phase reaction typically seen in nanomaterials.³³⁹ Reducing the coherence length in a material can turn first-order phase transitions into second-order transitions or eliminate them.³⁴⁰ In the δ -phase, a little coherence length significantly impacts electrochemical performance by eliminating the 3 V plateau and converting the related phase change into a solid solution region (Fig. 27a). This attribute of the δ -phase removes phase change strain as a potential decomposition pathway, allowing manganese-based spinels to cycle across their entire theoretical capacity range. Furthermore, forming the δ -phase enhances rate performance, aligning with previous theoretical findings that spinel-like arrangements have a greater extensive low-barrier transition metal percolation network, facilitating lithium transport. In the δ -phase, a larger portion of the capacity is delivered at greater voltages, which is advantageous for power delivery in practical battery applications. The δ -phase exhibits spinel-like voltage profiles and rates while maintaining a sufficiently small coherence length to exist as a solid solution, thus inhibiting the two-phase reaction observed in ordered spinels (Fig. 27).

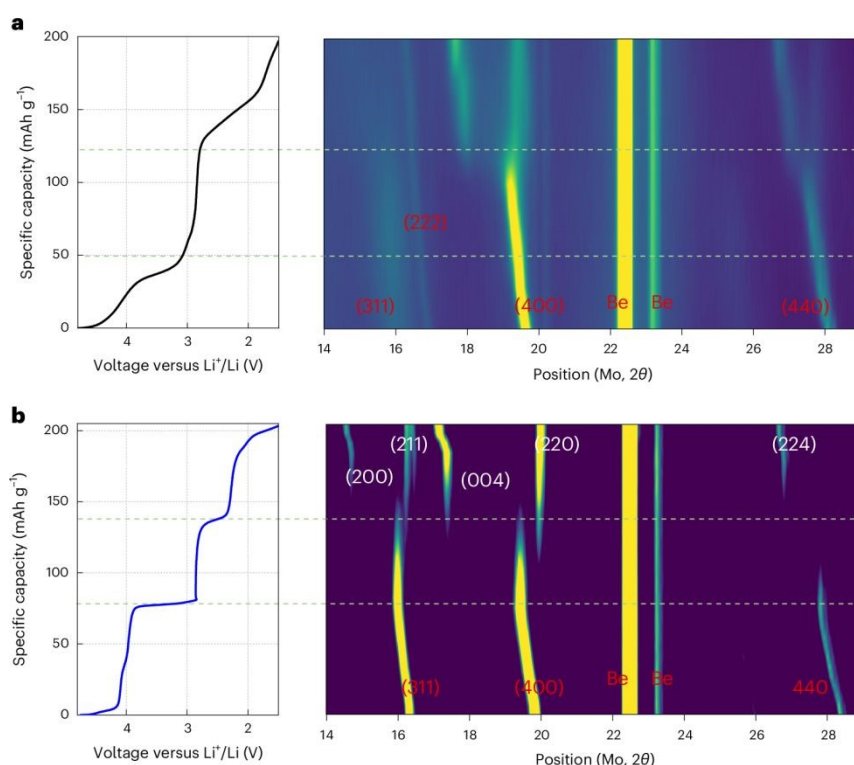


Fig. 27 In situ XRD measurements. In situ XRD measurement for $\text{Li}_{0.7}\text{Mn}_{0.65}\text{Ti}_{0.1}\text{O}_{1.9}\text{F}_{0.1}$ (L07M65-DH) and LiMn_2O_4 during their initial cycle. Voltage profile (left) and in situ XRD patterns (right) for (a) L07M65-DH and (b) LiMn_2O_4 . The current rate was 20 mA g^{-1} , with



X-ray scans performed every 30 minutes. Peaks corresponding to cubic spinel are highlighted in red, while those for tetragonal spinel are indicated in white.³³⁸

4.8 Electron backscatter diffraction

Electron backscatter diffraction (EBSD) is the most potent method for analyzing the microstructure of metals and tracking their evolution. This technique provides quantitative data on grain size, orientation, boundaries, and potential dislocations and strain within large single grains.³⁴¹⁻³⁴³ However, it necessitates a well-defined sample surface regarding flatness, crystallinity, and chemical composition. Thin decomposition layers, often less than 50 nm, that form on lithium^{344, 345} can obscure the electron diffraction pattern because EBSD has a limited probe depth of about 20 nm. Consequently, there are minimal studies utilizing EBSD on lithium foils.^{341, 346-348}

Till et al.³⁴⁹ developed a method to study metal growth and dissolution in anode-free solid-state batteries using in situ electron backscatter diffraction (EBSD). Their examination throughout cross-sectional deposition and dissolution provided insights into microstructural evolution (Fig. 28), revealing that small lithium grains undergo annealing akin to Ostwald ripening. They found that pore emergence during the discharge of the metal anode primarily happens at the interface between the grain bulk and the solid electrolyte. Notably, the areas where metal grain boundaries encounter the interface remain undamaged, this is because of the more rapid diffusion of metal and vacancies along these boundaries. The density of nucleation is impacted by factors like applied CD, temperature, and the surface characteristics of the SE.^{131, 350, 351} Furthermore, their in situ EBSD findings indicate that both grain nucleation and the growth process are crucial for controlling the resulting microstructure. The applied CD may also affect grain development during electrodeposition, and applying stack pressure could be an effective method to manage the lateral extension of developing grains.³⁵² Overall, this analysis enhances the understanding of metal electrodes and their microstructural evolution.



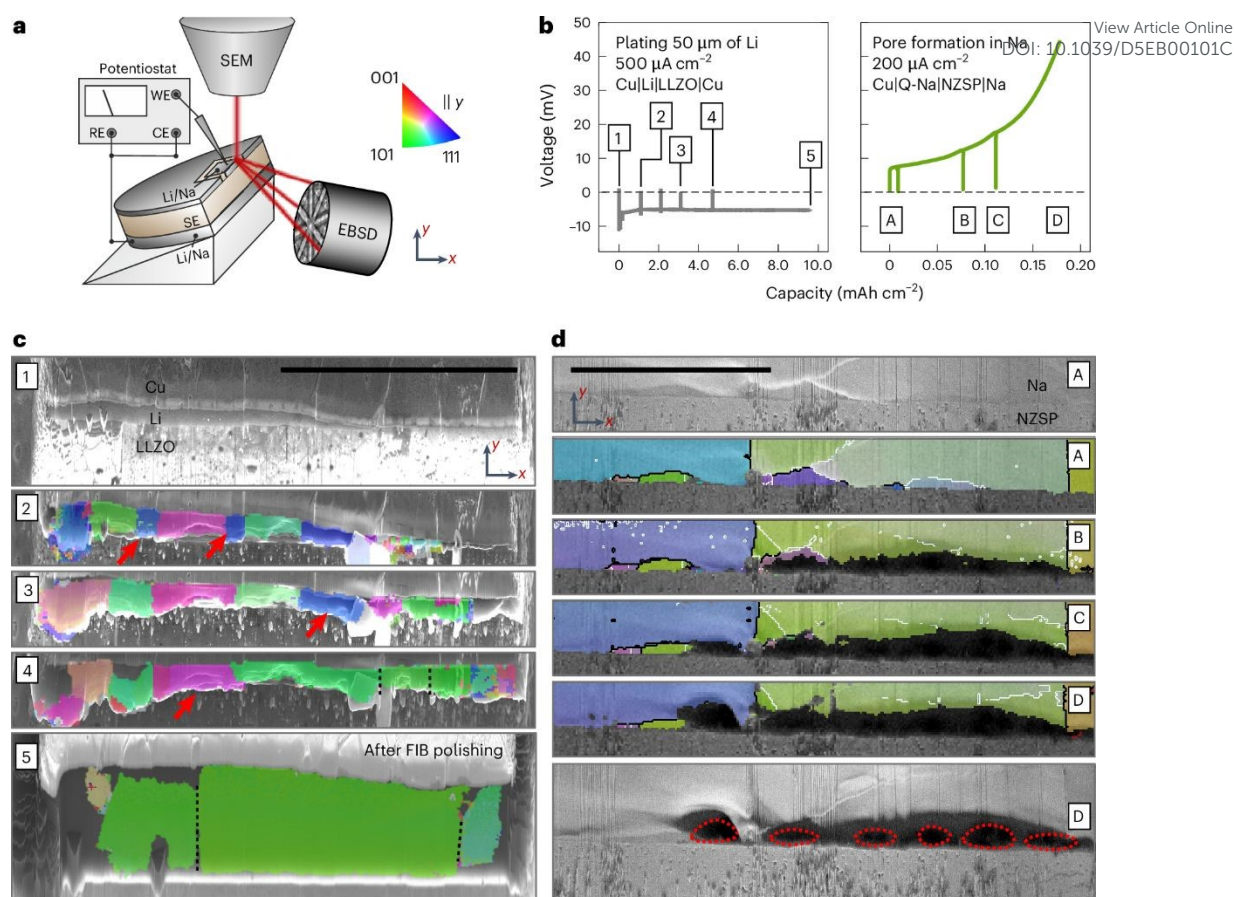


Fig. 28 In situ EBSD approach to examine the microstructural changes occurring during the electrodeposition and electrodisolution of an alkali metal electrode in contact with a solid electrolyte. (a) A schematic representation of the in situ EBSD setup (b) Voltage profiles for depositing 50 μm of Li at the Cu|Li|SE interface and for stripping Na until pore formation occurs at the Cu|Q-Na|SE interface. The microstructural change during (c) Li plating and (d) Na stripping.³⁴⁹

4.9 Cryo-Electron Microscopy

Cryo-electron microscopy (Cryo-EM), originally developed for structural biology, is increasingly attracting interest from materials scientists who seek to exploit its capabilities for studying beam-sensitive materials.^{353, 354} Battery materials, particularly after cycling, are often sensitive to air exposure, making cryogenic temperatures crucial for maintaining their native state and preserving inherent information. Cryo-EM enables the observation of battery materials with enhanced electron beam tolerance, minimizing radiation damage. For instance, Li et al. utilized cryo-EM to image the atomic structure of lithium metal dendrites formed through electrochemical deposition, as well as their interfaces with the SEI³⁵⁴ (Fig. 29a). They discovered variations depending on the electrolyte systems used, which aids in understanding



the failing causes within high-energy batteries. This approach can also be applied to other chemically reactive and beam-sensitive materials. Similarly, Wang et al.³⁵⁵ investigated the microstructure of electrochemically deposited lithium (EDLi) and its associated SEI at the atomic level (Fig. 29b), noting how different electrolyte additives impacted the surface properties of EDLi, thereby influencing Coulombic efficiency. This demonstrates cryo-EM's effectiveness in examining micro-mechanisms related to lithium materials that affect battery efficiency. Zachman et al.³⁵⁵ also employed a novel cryo-FIB method to characterize and extract intact interfaces from coin cell batteries for cryo-STEM analysis. Cryo-STEM's structural/chemical mapping revealed insights into lithium dendrites' formation mechanisms (Fig. 29c). These cryo-EM studies significantly enhance the perception of reaction intermediates and mechanisms in lithium-metal batteries. By merging cryo-STEM with cryo-FIB³⁵⁵, new insights into interactions and failing causes at the lithium/solid electrolyte interfaces may emerge, potentially leading to effective strategies for advancing lithium metal anode technology. A comprehensive review of cryo-EM application in battery material research is available for further reference.³⁵⁶

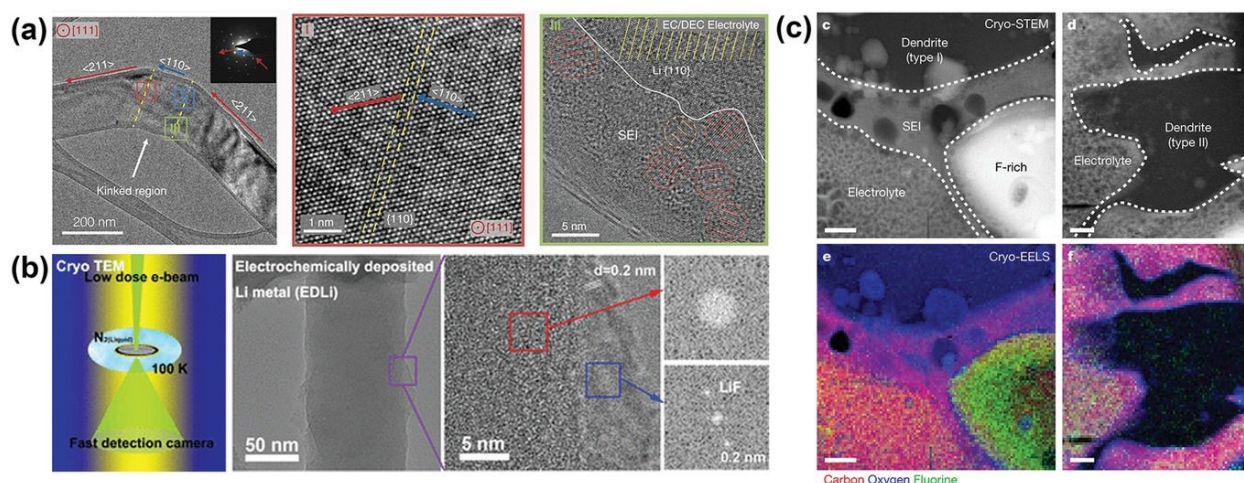


Fig. 29 (a) Atomic-resolution transmission electron microscopy images showcasing Li metal and its interface with the SEI.³⁵⁷ (b) Cryogenic transmission electron microscopy image depicting EDLi.³⁵⁵ (c) High-angle annular dark field cryo-scanning transmission electron microscopy images along with corresponding electron energy loss spectroscopy elemental mapping for two distinct types of dendrites dendrites³⁵⁸.

4.10 Scanning electron microscopy (SEM)

In contrast to ex-situ characterizations, in situ and operando techniques, such as SEM, enable real-time observation of interfacial structural changes and phase transitions in non-equilibrium



states during charging and discharging. These methods provide immediate insights into lithiation and delithiation processes, aiding in understanding structure-performance relationships and electrochemical mechanisms in ASSLMs. Recent studies have employed in situ/operando techniques to examine interfacial challenges within solid-state systems. For instance, in-situ SEM characterization has shown that achieving uniform Li deposition on the SE and preventing dendrite formation is essential for facilitating highly reversible Li deposition/dissolution reactions.³⁵⁹

Motohiro et al.²⁰⁰ investigated the Li deposition/dissolution processes at varying CDs in sulfide-based ASSLM using in situ SEM observations (Fig. 30). Fig. 30a presents schematics of the Li/SE/stainless steel cells before cycling, along with a magnified view of SE and stainless steel interface during charging/discharging. As Li is deposited onto the stainless steel during the charging process, the space between the SE and stainless steel enlarges due to the increasing thickness of the accumulated Li. Conversely, during discharging, as Li ions dissolve into the SE, this space narrows. Fig. 30b illustrates the voltage curves for Li deposition/dissolution in Li/SE/stainless steel cells at 0.01 mA cm² during the first and second cycling and at 0.05 mA cm² during the third and fourth cycling. The cell maintains a relatively stable voltage of approximately +40 mV for only two cycles at 0.01 mA cm². Fig. 30c shows the morphological changes at the SE/CC interface (first → second cycle). Unlike the morphology observed during high CD electrochemical tests, no new crack or pillared deposit appears across the SE surface during charge/discharge processes via a lower CD of 0.01 mA cm².

Figs. 30d-30f displays SEM images of the interface morphology between the SE layer and the stainless steel at the same location within the cell under different conditions: (d) immediately after a short circuit, (e) during Li deposition at 5 mA cm² for 10 minutes following the short circuit, and (f) during Li dissolution at 20 mA cm² for 20 minutes after (e). These images illustrate the morphological changes that occur when electrochemical measurements are conducted at high current densities after short circuits, indicating limited Li deposition and dissolution. In Fig. 30d, a pillared deposit is visible, emerging from big cracks in the SE layer's surface. This deposit differs from the SE layer's morphology, suggesting it is lithium. In Fig. 30e, lithium appears to grow slightly during the deposition process compared to Fig. 30d, with the dotted line measuring 6.6 mm in (d) and 12.8 mm in (e). A new big crack is observed on the right side of the pillared deposit, likely resulting from the elongation of Li deposition, demonstrating that lithium is extending from the inner part of the solid electrolyte layer. In



other ways, Fig. 30f reveals that the pillared deposit decreases following the Li dissolution reactions, with the dotted line in this image measuring 10.9 μm , which is smaller than the measurement in Fig. 30e, confirming lithium contraction.

In general, their findings visually demonstrated that the morphologies of Li deposition change with CDs. When the CD exceeds 1 mA cm^{-2} , localized Li deposition causes significant cracking, which reduces the reversibility of deposition/dissolution processes. Conversely, at a low CD of 0.01 mA cm^{-2} , the uniform deposition allows for reversible lithium processes and minimizes the formation of harmful cracks. These outcomes indicate that obtaining uniform Li deposition on the solid electrolyte and preventing Li metal development along grain boundaries within the solid electrolyte are crucial for facilitating repetitive Li deposition/dissolution without compromising the integrity of the solid electrolyte.

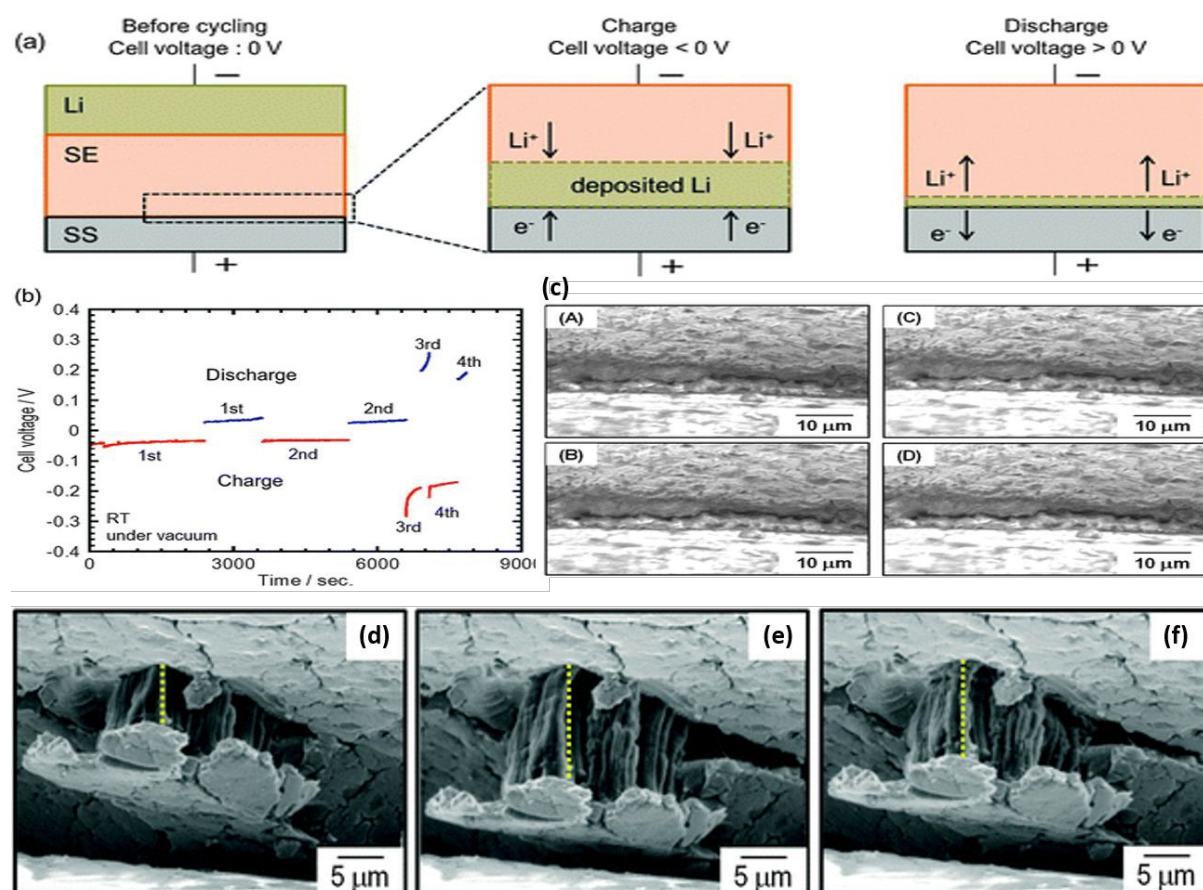


Fig. 30 In situ SEM measurements at different CDs. (a) Schematic diagrams illustrate the Li/SE/SS cells before the cycle and a detailed view of the interface between the solid electrolyte and stainless steel during charging and discharging. (b) Li deposition and dissolution curves for Li/SE/SS are presented at a CD of 0.01 mA cm^{-2} during the first and second cycles and at



0.05 mA cm⁻² during the third and fourth cycles. (c) SEM images of the interface show conditions (A) after the first charge, (B) after the first discharge, (C) after the second charge, and (D) after the second discharge. SEM images of SE/stainless steel interface at a similar location within a similar configuration are shown (d) instantly following a short circuit, (e) during Li deposition via 5 mA cm⁻² for 10 minutes after the short circuit, and (f) during Li dissolution via 20 mA cm⁻² for 20 minutes shortly after (e).²⁰⁰

4.11 Optical microscope

Di et al.³⁶⁰ examined the lithium plating/stripping phenomena in argyrodite-based ASSLMs using optical microscopy (OM). To explore the impact of current densities on the CE, they performed an in situ OM study to analyze lithium plating and stripping behaviors during the initial two cycles (Fig. 31a). As plating commences, small white spots appear on the surface of SE, indicating nucleation of metallic lithium. This nucleation is observed to be random and heterogeneous (Fig. 31b). As plating progresses, these white spots serve as seeds that enlarge. The central region becomes black during this growth while the surrounding area remains white. Ultimately, large white islands with a central black spot are randomly distributed across the SE surface (Fig. 31c). During the stripping phase, the white islands are anticipated to shrink. However, they unexpectedly expand even while lithium is being removed from them (Figs. 31d and 31e), likely due to internal pressure within the in situ cell. As plating continues, additional white spots appear beneath the existing islands (marked by blue circles in Figs. 31f and 31g). In the second stripping cycle, similar behavior was observed, characterized by the expansion of the outer white areas and the shrinkage of the central dark regions (blue circles in Figs. 31h and 31i). Overall, lithium eventually forms isolated islands on the surface of the SE.³⁶¹ Additionally, a cell's plating and stripping processes that cycled at 200 μ A cm⁻² exhibited behaviors similar to those observed at 10 μ A cm⁻². The initial lithium plating remains non-uniform and localized. Still, with higher CD, more lithium islands form, featuring larger central black spots, and these islands grow at an accelerated rate.



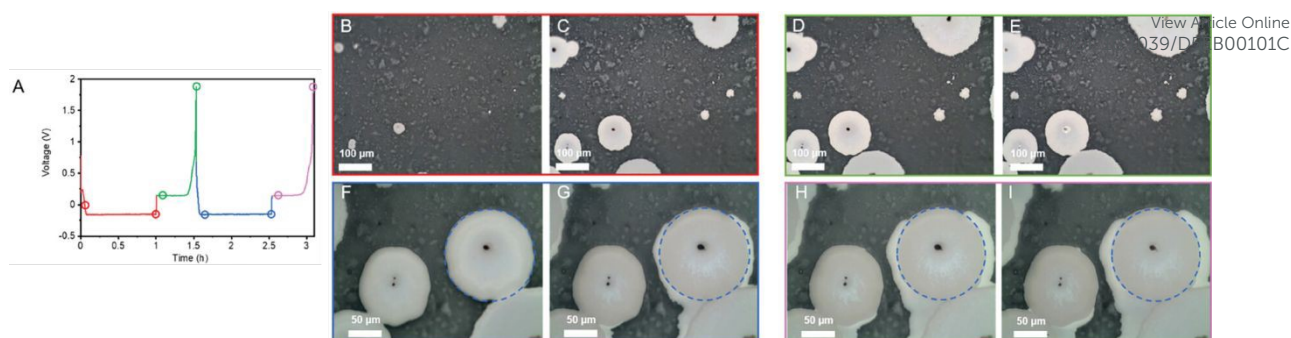


Fig. 31 In situ OM measurements. a) Voltage profiles at $10 \mu\text{A cm}^{-2}$ along with optical images taken at various time points, b) and c) during the first plating, d) and e) during the first stripping, f) and g) during the second plating, h) and i) during the second stripping.³⁶⁰

4.12 Time-of-Flight Secondary Ion Mass Spectrometry (ToF-SIMS)

Huo et al. investigated the phenomena of particles in the $\text{Li}_6\text{PS}_5\text{Cl}$ matrix before cycling and after 100 cycles via ToF-SIMS mass images (Figs. 32a and 32b)³⁶². Specifically, after cycling, a layer exhibiting increased intensity of sulfur fragments was observed around the silicon particles (Fig. 32b). This is interpreted as strong confirmation for the Li_2S -rich SEI at the $\text{Si}|\text{Li}_6\text{PS}_5\text{Cl}$ interface.

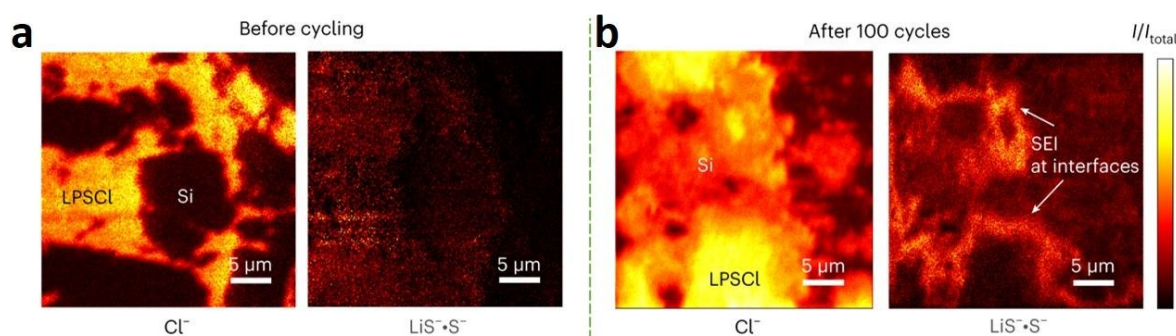


Fig. 32 ToF-SIMS images of the Cl^- fracture and the product of the LiS^- and S^- fractures in $\text{Si}/\text{Li}_6\text{PS}_5\text{Cl}$ composites before cycle (a) and after 100 cycling (b).³⁶²

4.13 Kelvin Probe Force Microscopy (KPFM)

Recently, Wan et al. utilized in situ Kelvin probe force microscopy (KPFM), a robust technique for monitoring potential variations, to visualize the lithium ion behavior in $\text{LPS}|\text{LGPS}|\text{LPS}$ sandwich electrolyte interfaces (Fig. 33a). The $\text{LPS}|\text{LGPS}|\text{LPS}$ sandwich electrolyte will be a model system to examine the interfacial interactions between distinct SEs. Fig. 33b shows the



KPFM image of the LGPS|LPS interface at OCP. Upon applying an overpotential of -0.5 V, the potential at the interface increased, as depicted in Fig. 33c. Both LGPS and LPS, as inorganic SEs, have transference numbers close to unity, indicating that Li ions are nearly the only mobile ions in these SEs.⁶⁴ Therefore, the increased interfacial potential was ascribed to the accumulation of Li ions at the interface. Amplification of the overpotential led to a further increase in interfacial potential (Fig. 33d), indicating a huge concentration of lithium ions at the interfaces. KPFM imaging successfully visualized the distribution of the lithium-ion field. Complementary COMSOL simulations (Figs. 33e–33g) provided further insight into this phenomenon, confirming the results obtained from the in situ KPFM analysis.

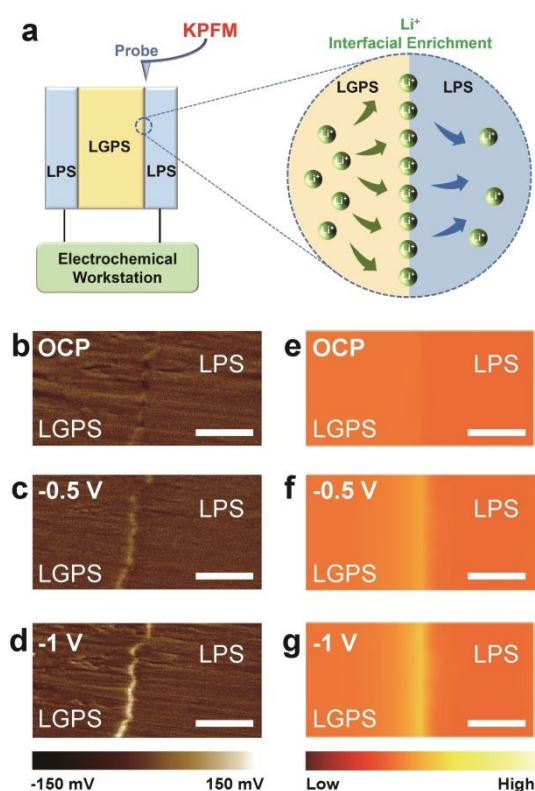


Fig. 33 Li-ion behavior at the interface between different SEs. (a) A schematic illustrating the in situ KPFM setup and Li-ion interfacial enrichment at the sandwiched SE. In situ KPFM images of the LGPS/LPS interface at various overpotentials of (b) OCP, (c) cathodic -0.5 V, (g) cathodic -1 V.³²⁰

Advanced in-situ and ex-situ characterization techniques are crucial for understanding solid interfacial reactions, including structural evolution, phase transitions, and fundamental ion-transport mechanisms at interfaces. These methods can help address interfacial challenges, such as compatibility, stability, and resistance in solid-state systems, thus revealing the kinetics



of reactions and mechanisms of decay in ASSBs. A combination of various in-situ and ex-situ methods is essential to investigate interface evolution further.

[View Article Online](#)

DOI: 10.1039/D5EB00101C



5. Perspectives

Improving the efficiency of ASSBs hinges on integrating SEs that exhibit significant σ at ambient temperature and enhanced stability at interfaces. While Li-argyrodites stand out as the most promising electrolyte for ASSBs, substantial challenges persist concerning the material itself, electrode materials, and their interfaces, despite notable advancements achieved thus far. To realize Li-argyrodite-based ASSBs, these problems should be solved first as follows.

- **Optimization of SEs based on interfacial stability:** Despite the current focus in ASSB research on developing high ionic conductive SEs to match the conductivity of LEs, there is a notable lack of consideration for the electrode–SE charge transfer resistance in the design of these new SEs. While adding halides like I, Br, or Cl can enhance the ionic conductivity of Li argyrodites, they are incompatible with Li metal and high-voltage oxide cathode materials due to numerous anionic redox phenomena while charging. This leads to a thicker and unstable SEI and CEI layer with high interfacial resistance, making these electrolytes impractical. Hence, there is a need to prioritize and conduct the examination of SEs according to their interfacial characteristics with specific electrode materials. For instance, using a cation-doped argyrodite SE and optimizing the interface stability between lithium metal and the electrolyte through a Li-M alloy formation leads to a minimized interfacial resistance.
- **Mechanical property of SEs and electrodes:** The mechanical characteristics of each component in ASSBs are critical factors for ensuring successful cycle performance. This is particularly crucial for the soft lithium metal anode because the development of lithium metal dendrites and lithium plating/stripping kinetics are heavily influenced by mechanical integrity around the interface. Applying lithophilic coatings on lithium anode stabilizes the lithium and solid electrolyte interface, promoting non-dendritic lithium deposition but typically at small current densities. Nevertheless, questions remain regarding the long-term mechanical stabilities of these lithophilic coating layers, especially with higher capacities of lithium depositions. For instance, a coating thickness of 1–2 nm is optimal for electronically insulating but chemically protective layers like Al_2O_3 , while a thickness of 5–10 nm is more appropriate for lithium-ion conductive coatings. In addition, heat treatment ($\sim 400\text{--}600\text{ }^\circ\text{C}$) generally increases the crystallinity of argyrodite SEs, leading to improved ionic conductivity. Pore size and distribution play a crucial role in shaping lithium-ion



transport paths. They may act as stress concentration points, increasing the risk of fractures or lithium dendrite intrusion. Densification methods such as hot-pressing or sintering will be employed to reduce porosity and enhance mechanical integrity. Mechanical strain develops throughout battery cycling due to volumetric changes, requiring solid electrolytes to endure compressive and tensile stresses without fracturing. Incorporating dopants can enhance the ductility of solid electrolytes, helping to suppress crack initiation. At the interfaces between solid electrolytes and electrodes, lattice mismatch can cause interfacial strain and defects, compromising interfacial stability and elevating resistance. This challenge can be addressed through the use of interlayers or surface coatings. Additionally, interface defects such as cracks, voids, or delamination can obstruct ion transport and contribute to mechanical degradation. Optimization of microstructural design and the application of surface coatings can enhance interfacial contact and help prevent such degradation. Furthermore, the mechanical characteristics and structures of new interfaces toward battery performance, require thorough investigation. Detailed mechanical and chemical modeling of interfaces under static and dynamic changes in electric fields is necessary. Additionally, mechanical stress in ASSBs can extend over considerable distances. For instance, extensive lithium depositions (negative electrode side) can induce stress propagating through the solid electrolyte toward cathodes. This impacts chemical and mechanical compatibility during cycling. Therefore, comprehensive stress characterization at the full cell level is essential, as it is more relevant than focusing solely on characterizing individual components in ASSBs.

- ***Appropriate and optimized binder:*** Binders are commonly employed to address issues such as electrode or electrolyte disintegration and the disruption of conducting paths. These are essential for achieving thin film electrolytes with robust mechanical properties, which significantly impact battery performance. Traditional binders like PVDF, PTFE, or PEO are typically electrically insulating and ionically inactive, which can hinder lithium-ion transport, especially if they are unevenly distributed, potentially obstructing conductive pathways. To enhance overall transport performance, dual-conductive binders can support both ionic and electronic conduction. Additionally, binders may cause interfacial resistance or create voids at the electrode-electrolyte interface, impairing effective solid-solid contact essential for lithium-ion movement. Under cycling or thermal stress, some binders may swell or deform, disrupting interfacial pressure and stability. As a solution, hybrid inorganic/polymer binders will offer a good compromise by providing mechanical



robustness and improved conductivity, thereby mitigating adverse effects on electrochemical transport. However, it's crucial to consider the interaction between Li argyrodites and binders as a design factor for ASSLB electrodes. Therefore, it is strongly advised that the adhesive properties of binders be thoroughly understood and the binder quantity optimized before cell assembly.

- **Pressure:** In ASSB systems, the procedures related to external pressure during assembly are closely linked to the stabilities of materials at atomistic/interface level. Applying external pressure on the cathode side enhances interfacial ion diffusion, decreases interfacial impedance, and boosts ion transport efficiency. Suitable pressure helps eliminate interfacial voids on the anode side, preserving a continuous ion transport network. However, excessive pressure may lead to short circuits, as many anode materials exhibit creep behavior under high stress. Applying stack pressures in the range of 3–7 MPa can effectively minimize problems such as lithium metal deformation and improve the physical contact between the solid electrolyte and electrodes, lowering interfacial resistance and enhancing cycling performance. The concept of local mechanical constriction connects the macroscopic parameters of the device with the microscopic properties of materials. In such environments, degradation reactions with positive reaction strains, leading to volume extension during decomposition, may encounter a unique effect called constriction-induced meta-stability. This effect can cause a sudden change in the energy landscape related to these decomposition reactions. Therefore, understanding the local mechanical constriction effect and interfacial compatibility during cycling is crucial for exploring the potential to further design this effect for Li argyrodites. This understanding could lead to unlocking battery performance improvements beyond what is currently achieved in commercial batteries. Developing ductile electrodes, electrolytes, and interphases of a Li-argyrodite-based ASSB is crucial for its practical application under reasonable pressure. For example, using a solid electrolyte with intrinsically ductile and low porosity can help lower both the fabrication pressure required during processing and the stack pressure needed during operation of ASSB.
- **Artificial intelligence (AI) and machine learning (ML):** Machine learning models are capable of forecasting key properties of solid electrolytes, such as ionic conductivity, chemical stability, and compatibility with electrode materials, based on their structural and compositional features. Moreover, ML can be utilized to simulate interfacial degradation



phenomena, including the development of resistive interphase layers, by utilizing extensive molecular simulations supported by machine-learning-derived interatomic potentials. This approach enables rapid evaluation of new material candidates before committing to time-intensive experimental testing. Additionally, AI techniques assist in interpreting intricate interfacial transport behaviors, including lithium-ion diffusion and the dynamics of charged species.

AI and ML are poised to significantly enhance the development of battery technologies. To realize this potential, several challenges must be addressed:

- i. Establishing standardized protocols: Developing widely accepted standards for data collection, processing, and reporting in battery research is essential. This includes defining data formats, measurement conditions, and performance metrics to ensure consistency and comparability across studies. Implementing systematic data disclosure practices will facilitate data sharing and collaboration within the research community.
- ii. Identifying appropriate descriptors: Selecting the most relevant descriptors (features) for ML models is crucial. Descriptors should capture the underlying physics and chemistry of battery materials and interfaces to enable accurate predictions. Integrating domain-specific knowledge can aid in identifying these descriptors and improving model interpretability.
- iii. Quantifying model uncertainty: Determining the associated error or uncertainty of ML models is vital for assessing their reliability and robustness. Implementing uncertainty quantification methods can help identify areas where models may be less confident and guide further data collection or model refinement.

Addressing these challenges will pave the way for AI and ML to play a transformative role in the advancement of battery technologies, leading to more efficient, durable, and sustainable energy storage solutions.

- **Characterization techniques:** While advanced characterization techniques have revealed crucial mechanisms related to interfaces, most of these methods are ex-situ, providing limited real-time information. On the other hand, in situ/operando approaches are essential for understanding interface composition and structure, which are vital for ASSB design. In situ characterization is essential for capturing the dynamic and coupled chemo-mechanical processes occurring at interfaces in SSBs. For example, in situ X-ray computed tomography



(CT) facilitates the real-time observation of morphological changes within SSBs during cycling, such as the development of cracks and voids in the SE and at interfaces. These structural alterations can lead to capacity loss and failure. Identifying these changes is crucial for understanding failure modes and guiding design improvements. In addition, optical coherence tomography (OCT) is a non-invasive, high-resolution imaging technique that enables real-time, cross-sectional visualization of internal structures in SSBs. It has been effectively employed to monitor the morphology, growth, and evolution of lithium dendrites at the interfaces between electrodes and SEs during cycling under various conditions. This capability allows for the dynamic observation of dendrite formation and progression, providing valuable insights into the mechanisms affecting SSB performance and safety. At the same time, ex-situ methods serve as valuable complements by delivering high-resolution structural or compositional information after changes have occurred. However, ex-situ techniques offer only fixed, post-mortem views, which can miss short-lived or intermediate phenomena. Additionally, transferring samples to measurement setups can introduce artifacts, such as reactions with air or moisture, and these methods often struggle to accurately reflect the true interfacial chemistry, particularly in reactive materials like sulfide-based electrolytes. However, extracting solid-solid interfaces embedded in ASSBs presents challenges. Moreover, due to the fragility of interfaces, solid electrolytes, and lithium metal, cryogenic protection is vital to reduce beam destruction and stabilize samples. Hence, developing and customizing new techniques with integrated functionalities is crucial for obtaining information on structure, composition, and kinetics. In general, computational modeling and experimental methods necessitate high-throughput screening, diagnosis, and interfacial engineering for ASSBs.



Associated Content

View Article Online
DOI: 10.1039/D5EB00101C

Supporting Information

Interfacial challenges: assembly, additives, and space charge layer,

Strategies to improve the interface stability: Li metal coating techniques, protection layers, appropriate additives, appropriate assembling techniques, and utilizing the appropriate ratio of materials

Tables: Comparison of the electrochemical performance of coated/doped cathodes with bare cathodes, solvents and binders used for wet-slurry fabrication of ASSLB electrodes using Li-argyrodite SEs, properties of $\text{Li}_6\text{PS}_5\text{Cl}$ film with different binders, the Hansen solubility parameters for the chosen polymer binders and the p-xylene solvent, and the conductivity of the Li-argyrodites as documented in the literature along with the fabrication pressure, stack pressure, and electrode material

Figures: XPS spectra of the S 2p and P 2p signals for cycled and uncycled composite cathodes with and without VGCF after surface cleaning, the influence of carbon on SE degradation, Li coating techniques, schematic representation of how protective layers help prevent lithium dendrite formation in SEs, scheme illustrating the criteria that binders are expected to fulfill, plots of ionic conductivity versus pressure for samples with various binder materials, and the impact of pressure on the battery assembly.

Acknowledgments

Financial support from the National Science and Technology Council of Taiwan (NSTC 112-2639-E-011-001-ASP, 112-2923-E-011-005, 112-2923-E-011-001, 112-2923-E-011-004-MY3; 112-2218-E-011-011), the Ministry of Education of Taiwan (the Sustainable Electrochemical Energy Development Center (SEED Center) from the Featured Areas Research Center Program), as well as the supporting facilities from National Taiwan University of Science and Technology (NTUST), National Center for High performance Computing (NCHC), and National Synchrotron Radiation Research Centre (NSRRC), are all gratefully acknowledged.



References

1. S. Boulinaeu, M. Courty, J.-M. Tarascon and V. Viallet, *Solid State Ionics*, 2012, **221**, 1-5.
2. B. Vinay, Y. Nikodimos, T. Agnihotri, S. A. Ahmed, T. M. Hagos, R. Hasan, E. B. Tamararasan, W.-N. Su and B. J. Hwang, *Energy & Environmental Science*, 2025.
3. P. Birke, F. Salam, S. Döring and W. Weppner, *Solid State Ionics*, 1999, **118**, 149-157.
4. A. Aboulaich, R. Bouchet, G. Delaizir, V. Seznec, L. Tortet, M. Morcrette, P. Rozier, J. M. Tarascon, V. Viallet and M. Dollé, *Advanced Energy Materials*, 2011, **1**, 179.
5. C. Masquelier, *Nature materials*, 2011, **10**, 649-650.
6. T. Chen, L. Zhang, Z. Zhang, P. Li, H. Wang, C. Yu, X. Yan, L. Wang and B. Xu, *ACS applied materials & interfaces*, 2019, **11**, 40808-40816.
7. Y. Cheng, X. Ke, Y. Chen, X. Huang, Z. Shi and Z. Guo, *Nano Energy*, 2019, **63**, 103854.
8. X.-B. Cheng, C.-Z. Zhao, Y.-X. Yao, H. Liu and Q. Zhang, *Chem*, 2019, **5**, 74-96.
9. R. Xu, X. Xia, S. Zhang, D. Xie, X. Wang and J. Tu, *Electrochimica Acta*, 2018, **284**, 177-187.
10. J. Auvergniot, A. Cassel, J.-B. Ledeuil, V. Viallet, V. Seznec and R. Dedryvère, *Chemistry of Materials*, 2017, **29**, 3883-3890.
11. J. Auvergniot, A. Cassel, D. Foix, V. Viallet, V. Seznec and R. Dedryvère, *Solid State Ionics*, 2017, **300**, 78-85.
12. G. G. Serbessa, B. W. Taklu, Y. Nikodimos, N. T. Temesgen, Z. B. Muche, S. K. Merso, T.-I. Yeh, Y.-J. Liu, W.-S. Liao and C.-H. Wang, *ACS Applied Materials & Interfaces*, 2024, **16**, 10832-10844.
13. Y. Nikodimos, C.-J. Huang, B. W. Taklu, W.-N. Su and B. J. Hwang, *Energy & Environmental Science*, 2022, **15**, 991-1033.
14. N. T. Temesgen, H. K. Bezabh, M. A. Weret, K. N. Shitaw, Y. Nikodimos, B. W. Taklu, K. Lakshmanan, S.-C. Yang, S.-K. Jiang and C.-J. Huang, *Journal of Power Sources*, 2023, **556**, 232462.
15. H. Lee, P. Oh, J. Kim, H. Cha, S. Chae, S. Lee and J. Cho, *Advanced Materials*, 2019, **31**, 1900376.
16. J. Ma, B. Chen, L. Wang and G. Cui, *Journal of Power Sources*, 2018, **392**, 94-115.
17. S. P. Culver, R. Koerver, T. Krauskopf and W. G. Zeier, *Chemistry of Materials*, 2018, **30**, 4179-4192.
18. Y. Wang, W. D. Richards, S. P. Ong, L. J. Miara, J. C. Kim, Y. Mo and G. Ceder, *Nature materials*, 2015, **14**, 1026-1031.
19. Y. Kato, S. Hori, T. Saito, K. Suzuki, M. Hirayama, A. Mitsui, M. Yonemura, H. Iba and R. Kanno, *Nature Energy*, 2016, **1**, 1-7.
20. N. Kamaya, K. Homma, Y. Yamakawa, M. Hirayama, R. Kanno, M. Yonemura, T. Kamiyama, Y. Kato, S. Hama and K. Kawamoto, *Nature materials*, 2011, **10**, 682-686.
21. Y. Seino, T. Ota, K. Takada, A. Hayashi and M. Tatsumisago, *Energy & Environmental Science*, 2014, **7**, 627-631.
22. M. Nagao, H. Kitaura, A. Hayashi and M. Tatsumisago, *Journal of The Electrochemical Society*, 2013, **160**, A819.
23. B. D. Dandena, D.-S. Tsai, S.-H. Wu, W.-N. Su and B. J. Hwang, *Energy Storage Materials*, 2024, 103305.
24. B.-Y. Tsai, S.-K. Jiang, Y.-T. Wu, J.-S. Yang, S.-H. Wu, P.-C. Tsai, W.-N. Su, C.-Y. Chiang and B. J. Hwang, *The Journal of Physical Chemistry C*, 2023, **127**, 14336-14343.
25. S.-K. Jung, H. Gwon, S.-S. Lee, H. Kim, J. C. Lee, J. G. Chung, S. Y. Park, Y. Aihara and D. Im, *Journal of Materials Chemistry A*, 2019, **7**, 22967-22976.
26. F. Zhao, J. Liang, C. Yu, Q. Sun, X. Li, K. Adair, C. Wang, Y. Zhao, S. Zhang and W. Li, *Advanced Energy Materials*, 2020, **10**, 1903422.
27. H. Liu, Q. Zhu, Y. Liang, C. Wang, D. Li, X. Zhao, L. Gao and L.-Z. Fan, *Chemical Engineering Journal*, 2023, **462**, 142183.
28. D. H. Tan, E. A. Wu, H. Nguyen, Z. Chen, M. A. Marple, J.-M. Dour, X. Wang, H. Yang, A. Banerjee and Y. S. Meng, *ACS Energy Letters*, 2019, **4**, 2418-2427.



29. Y. Zhu, X. He and Y. Mo, *ACS applied materials & interfaces*, 2015, **7**, 23685-23693.
30. T. K. Schwietert, V. A. Arszewska, C. Wang, C. Yu, A. Vasileiadis, N. J. de Klerk, J. Hageman, T. Hupfer, I. Kerkamm and Y. Xu, *Nature materials*, 2020, **19**, 428-435.
31. S. Wenzel, S. J. Sedlmaier, C. Dietrich, W. G. Zeier and J. Janek, *Solid State Ionics*, 2018, **318**, 102-112.
32. B. D. Dandena, L.-T. Wu, T.-I. Yeh, C.-Y. Chang, J.-C. Jiang, D.-S. Tsai, M. Ihrig, G. G. Serbessa, S.-C. Yang and K. Lakshmanan, *Chemical Engineering Journal*, 2025, 162450.
33. X. Han, Y. Gong, K. Fu, X. He, G. T. Hitz, J. Dai, A. Pearce, B. Liu, H. Wang and G. Rubloff, *Nature materials*, 2017, **16**, 572-579.
34. S. Choi, M. Jeon, J. Ahn, W. D. Jung, S. M. Choi, J.-S. Kim, J. Lim, Y.-J. Jang, H.-G. Jung and J.-H. Lee, *ACS applied materials & interfaces*, 2018, **10**, 23740-23747.
35. R. Koerver, I. Aygün, T. Leichtweiß, C. Dietrich, W. Zhang, J. O. Binder, P. Hartmann, W. G. Zeier and J. r. Janek, *Chemistry of Materials*, 2017, **29**, 5574-5582.
36. F. Han, Y. Zhu, X. He, Y. Mo and C. Wang, *Advanced Energy Materials*, 2016, **6**, 1501590.
37. X. Fan, X. Ji, F. Han, J. Yue, J. Chen, L. Chen, T. Deng, J. Jiang and C. Wang, *Science advances*, 2018, **4**, eaau9245.
38. J. Haruyama, K. Sodeyama, L. Han, K. Takada and Y. Tateyama, *Chemistry of Materials*, 2014, **26**, 4248-4255.
39. J. L. Barton and J. O. M. Bockris, *Proceedings of the Royal Society of London. Series A. Mathematical and Physical Sciences*, 1962, **268**, 485-505.
40. F. Han, A. S. Westover, J. Yue, X. Fan, F. Wang, M. Chi, D. N. Leonard, N. J. Dudney, H. Wang and C. Wang, *Nature Energy*, 2019, **4**, 187-196.
41. F. Walther, R. Koerver, T. Fuchs, S. Ohno, J. Sann, M. Rohnke, W. G. Zeier and J. r. Janek, *Chemistry of materials*, 2019, **31**, 3745-3755.
42. F. Walther, S. Randau, Y. Schneider, J. Sann, M. Rohnke, F. H. Richter, W. G. Zeier and J. r. Janek, *Chemistry of Materials*, 2020, **32**, 6123-6136.
43. F. Walther, F. Strauss, X. Wu, B. Mogwitz, J. Hertle, J. Sann, M. Rohnke, T. Brezesinski and J. r. Janek, *Chemistry of Materials*, 2021, **33**, 2110-2125.
44. Y. Yamagishi, H. Morita, Y. Nomura and E. Igaki, *ACS Applied Materials & Interfaces*, 2020, **13**, 580-586.
45. S. Narayanan, U. Ulissi, J. S. Gibson, Y. A. Chart, R. S. Weatherup and M. Pasta, *Nature Communications*, 2022, **13**, 7237.
46. J. Kasemchainan, S. Zekoll, D. Spencer Jolly, Z. Ning, G. O. Hartley, J. Marrow and P. G. Bruce, *Nature materials*, 2019, **18**, 1105-1111.
47. R. Schlenker, D. Stepien, P. Koch, T. Hupfer, S. Indris, B. Roling, V. Miß, A. Fuchs, M. Wilhelmi and H. Ehrenberg, *ACS Applied Materials & Interfaces*, 2020, **12**, 20012-20025.
48. W. Jiang, X. Zhu, Y. Liu, S. Zhao, R. Huang, M. Ling, L. Wang and C. Liang, *eTransportation*, 2023, **17**, 100246.
49. T. Krauskopf, B. Mogwitz, H. Hartmann, D. K. Singh, W. G. Zeier and J. Janek, *Advanced Energy Materials*, 2020, **10**, 2000945.
50. Y. Lu, C. Z. Zhao, H. Yuan, X. B. Cheng, J. Q. Huang and Q. Zhang, *Advanced Functional Materials*, 2021, **31**, 2009925.
51. Y. Liu, X. Xu, M. Sadd, O. O. Kapitanova, V. A. Krivchenko, J. Ban, J. Wang, X. Jiao, Z. Song and J. Song, *Advanced Science*, 2021, **8**, 2003301.
52. Y. Pang, J. Pan, J. Yang, S. Zheng and C. Wang, *Electrochemical Energy Reviews*, 2021, **4**, 169-193.
53. L. Mazzapioda, A. Tsurumaki, G. Di Donato, H. Adenusi, M. A. Navarra and S. Passerini, *Energy Materials*, 2023, **3**, 1-3025.
54. T. Tao, Z. Zheng, Y. Gao, B. Yu, Y. Fan, Y. Chen, S. Huang and S. Lu, *Energy Materials*, 2022, **2**, N/A-N/A.
55. T. Rahman and T. Alharbi, *Batteries*, 2024, **10**, 220.

View Article Online

DOI: 10.1039/D5EB00101C



56. H. Sano, Y. Morino, A. Yabuki, S. Sato, N. Itayama, Y. Matsumura, M. Iwasaki, M. Takehara, T. Abe and Y. Ishiguro, *Electrochemistry*, 2022, **90**, 037012-037012.
57. C. Yu, S. Ganapathy, E. R. van Eck, L. van Eijck, S. Basak, Y. Liu, L. Zhang, H. W. Zandbergen and M. Wagemaker, *Journal of Materials Chemistry A*, 2017, **5**, 21178-21188.
58. S. Y. Han, C. Lee, J. A. Lewis, D. Yeh, Y. Liu, H.-W. Lee and M. T. McDowell, *Joule*, 2021, **5**, 2450-2465.
59. S. Lou, Q. Liu, F. Zhang, Q. Liu, Z. Yu, T. Mu, Y. Zhao, J. Borovilas, Y. Chen and M. Ge, *Nature communications*, 2020, **11**, 5700.
60. S. Wang, A. La Monaca and G. P. Demopoulos, *Energy Advances*, 2025.
61. S. Wenzel, S. Randau, T. Leichtweiß, D. A. Weber, J. Sann, W. G. Zeier and J. r. Janek, *Chemistry of Materials*, 2016, **28**, 2400-2407.
62. S. Wenzel, T. Leichtweiss, D. Krüger, J. Sann and J. Janek, *Solid State Ionics*, 2015, **278**, 98-105.
63. Y. Xiao, Y. Wang, S.-H. Bo, J. C. Kim, L. J. Miara and G. Ceder, *Nature Reviews Materials*, 2020, **5**, 105-126.
64. Q. Zhao, S. Stalin, C.-Z. Zhao and L. A. Archer, *Nature Reviews Materials*, 2020, **5**, 229-252.
65. T. Famprikis, P. Canepa, J. A. Dawson, M. S. Islam and C. Masquelier, *Nature materials*, 2019, **18**, 1278-1291.
66. S. Wang, H. Song, X. Song, T. Zhu, Y. Ye, J. Chen, L. Yu, J. Xu and K. Chen, *Energy Storage Materials*, 2021, **39**, 139-145.
67. Y. Xuan, Y. Wang, B. He, S. Bian, J. Liu, B. Xu and G. Zhang, *Chemistry of Materials*, 2022, **34**, 9104-9110.
68. J. Tan, X. Ao, H. Zhuo, L. Zhuang, X. Huang, C. Su, W. Tang, X. Peng and B. Tian, *Chemical Engineering Journal*, 2021, **420**, 127623.
69. J. Xu, K. Liu, M. A. Khan, H. Wang, T. He, H. Zhao, D. Ye, Y. Tang and J. Zhang, *Chemical Engineering Journal*, 2022, **443**, 136637.
70. P. Lu, S. Gong, C. Wang, Z. Yu, Y. Huang, T. Ma, J. Lian, Z. Jiang, L. Chen and H. Li, *ACS nano*, 2024, **18**, 7334-7345.
71. S. Deng, M. Jiang, N. Chen, W. Li, M. Zheng, W. Chen, R. Li, H. Huang, J. Wang and C. V. Singh, *Advanced Functional Materials*, 2022, **32**, 2205594.
72. P. Lu, Y. Wu, D. Wu, F. Song, T. Ma, W. Yan, X. Zhu, F. Guo, J. Lu and J. Peng, *Energy Storage Materials*, 2024, **67**, 103316.
73. X. Shen, Y. Yang, X. Zhang and M. Chen, *Journal of Energy Storage*, 2023, **74**, 109296.
74. L. Guan, Y. Shi, C. Gao, T. Wang, J. Zhou and R. Cai, *Electrochimica Acta*, 2023, **440**, 141669.
75. J. Yan, J. Liu, Z. Liu, Q. Zhang, Y. Feng, W. Xia and J. Zhou, *Journal of Power Sources*, 2025, **631**, 236186.
76. H. S. Shin, W. G. Ryu, M. S. Park, K. N. Jung, H. Kim and J. W. Lee, *ChemSusChem*, 2018, **11**, 3184-3190.
77. Z. Jiang, H. Xie, S. Wang, X. Song, X. Yao and H. Wang, *Advanced Energy Materials*, 2018, **8**, 1801433.
78. B. Shao, Y. Huang and F. Han, *Advanced Energy Materials*, 2023, **13**, 2204098.
79. F. Zhao, Q. Sun, C. Yu, S. Zhang, K. Adair, S. Wang, Y. Liu, Y. Zhao, J. Liang and C. Wang, *ACS Energy Letters*, 2020, **5**, 1035-1043.
80. W. D. Richards, L. J. Miara, Y. Wang, J. C. Kim and G. Ceder, *Chemistry of Materials*, 2016, **28**, 266-273.
81. C. Wang, J. Liang, S. Hwang, X. Li, Y. Zhao, K. Adair, C. Zhao, X. Li, S. Deng and X. Lin, *Nano Energy*, 2020, **72**, 104686.
82. Q. Lv, Y. Jiang, B. Wang, Y. Chen, F. Jin, B. Wu, H. Ren, N. Zhang, R. Xu and Y. Li, *Cell Reports Physical Science*, 2022, **3**.
83. D. Avadanii, S. Ganschow, M. Stypa, S. Müller, S. Lang, D. Kramer, C. Kirchlechner and R. Mönig, *ACS Energy Letters*, 2025, **10**, 2061-2067.

View Article Online
DOI: 10.1039/D5EB00101C



84. B. Zhang, B. Yuan, X. Yan, X. Han, J. Zhang, H. Tan, C. Wang, P. Yan, H. Gao and Y. Liu, *Nature Communications*, 2025, **16**, 1906. View Article Online
DOI: 10.1039/D5EB00101C
85. C. Zhu, T. Fuchs, S. A. Weber, F. H. Richter, G. Glasser, F. Weber, H.-J. Butt, J. Janek and R. Berger, *Nature communications*, 2023, **14**, 1300.
86. H. Liu, Y. Chen, P.-H. Chien, G. Amouzandeh, D. Hou, E. Truong, I. P. Oyekunle, J. Bhagu, S. W. Holder and H. Xiong, *Nature Materials*, 2025, 1-8.
87. N. Sarfraz, N. Kanwal, M. Ali, K. Ali, A. Hasnain, M. Ashraf, M. Ayaz, J. Iftikhar, S. Ali and A. Hendi, *Energy Storage Materials*, 2024, 103619.
88. M. K. Tufail, P. Zhai, W. Khokar, M. Jia, N. Zhao and X. Guo, *Interdisciplinary Materials*, 2023, **2**, 529-568.
89. B. W. Taklu, W.-N. Su, Y. Nikodimos, K. Lakshmanan, N. T. Temesgen, P.-X. Lin, S.-K. Jiang, C.-J. Huang, D.-Y. Wang and H.-S. Sheu, *Nano Energy*, 2021, **90**, 106542.
90. Y. Jin, B. Zhu, Z. Lu, N. Liu and J. Zhu, *Advanced Energy Materials*, 2017, **7**, 1700715.
91. A. Franco Gonzalez, N.-H. Yang and R.-S. Liu, *The Journal of Physical Chemistry C*, 2017, **121**, 27775-27787.
92. V. A. Sethuraman, M. J. Chon, M. Shimshak, V. Srinivasan and P. R. Guduru, *Journal of Power Sources*, 2010, **195**, 5062-5066.
93. X. Yuan, H. Liu and J. Zhang, *Lithium-ion batteries: advanced materials and technologies*, CRC press, 2011.
94. W. Xu, J. Wang, F. Ding, X. Chen, E. Nasybulin, Y. Zhang and J.-G. Zhang, *Energy & Environmental Science*, 2014, **7**, 513-537.
95. D. Lin, Y. Liu and Y. Cui, *Nature nanotechnology*, 2017, **12**, 194-206.
96. K. N. Wood, M. Noked and N. P. Dasgupta, *ACS Energy Letters*, 2017, **2**, 664-672.
97. Y.-G. Lee, S. Fujiki, C. Jung, N. Suzuki, N. Yashiro, R. Omoda, D.-S. Ko, T. Shiratsuchi, T. Sugimoto and S. Ryu, *Nature Energy*, 2020, **5**, 299-308.
98. R. Xu, J. Yue, S. Liu, J. Tu, F. Han, P. Liu and C. Wang, *ACS Energy Letters*, 2019, **4**, 1073-1079.
99. A. Dey, *J. Electrochem. Soc.*, 1970, **117**.
100. E. Peled, *Journal of The Electrochemical Society*, 1979, **126**, 2047.
101. E. Peled, D. Golodnitsky and G. Ardel, *Journal of the Electrochemical Society*, 1997, **144**, L208.
102. D. Aurbach, B. Markovsky, M. Levi, E. Levi, A. Schechter, M. Moshkovich and Y. Cohen, *Journal of power sources*, 1999, **81**, 95-111.
103. M. Winter, *Zeitschrift für physikalische Chemie*, 2009, **223**, 1395-1406.
104. P. Verma, P. Maire and P. Novák, *Electrochimica Acta*, 2010, **55**, 6332-6341.
105. A. Wang, S. Kadam, H. Li, S. Shi and Y. Qi, *npj Computational Materials*, 2018, **4**, 15.
106. L. M. Riegger, S. Mittelsdorf, T. Fuchs, R. Rueß, F. H. Richter and J. r. Janek, *Chemistry of Materials*, 2023, **35**, 5091-5099.
107. G. Chaney, A. Golov, A. van Rookeghem, J. Carrasco and N. Mingo, *ACS Applied Materials & Interfaces*, 2024, **16**, 24624-24630.
108. P. Albertus, V. Anandan, C. Ban, N. Balsara, I. Belharouak, J. Buettner-Garrett, Z. Chen, C. Daniel, M. Doeff and N. J. Dudney, *Journal*, 2021.
109. Y. Lu, Z. Tu and L. A. Archer, *Nature materials*, 2014, **13**, 961-969.
110. J.-G. Zhang, W. Xu and W. A. Henderson, *Lithium metal anodes and rechargeable lithium metal batteries*, Springer International Publishing Cham, 2017.
111. R. Cao, W. Xu, D. Lv, J. Xiao and J. Zhang, *Journal*, 2015.
112. N. W. Li, Y. Shi, Y. X. Yin, X. X. Zeng, J. Y. Li, C. J. Li, L. J. Wan, R. Wen and Y. G. Guo, *Angewandte Chemie*, 2018, **130**, 1521-1525.
113. S. H. Wang, Y. X. Yin, T. T. Zuo, W. Dong, J. Y. Li, J. L. Shi, C. H. Zhang, N. W. Li, C. J. Li and Y. G. Guo, *Advanced Materials*, 2017, **29**, 1703729.
114. M. J. Wang, R. Choudhury and J. Sakamoto, *Joule*, 2019, **3**, 2165-2178.
115. P. Albertus, S. Babinec, S. Litzelman and A. Newman, *Nature Energy*, 2018, **3**, 16-21.
116. K. N. Wood and G. Teeter, *ACS Applied Energy Materials*, 2018, **1**, 4493-4504.



117. K. N. Wood, K. X. Steirer, S. E. Hafner, C. Ban, S. Santhanagopalan, S.-H. Lee and G. Teeter, *Nature communications*, 2018, **9**, 2490. View Article Online
DOI: 10.1039/D5EB00101C
118. L. Zhou, N. Minafra, W. G. Zeier and L. F. Nazar, *Accounts of chemical research*, 2021, **54**, 2717-2728.
119. Q. Zhang, D. Cao, Y. Ma, A. Natan, P. Aurora and H. Zhu, *Advanced Materials*, 2019, **31**, 1901131.
120. R. Chen, Q. Li, X. Yu, L. Chen and H. Li, *Chemical reviews*, 2019, **120**, 6820-6877.
121. L. Xu, S. Tang, Y. Cheng, K. Wang, J. Liang, C. Liu, Y.-C. Cao, F. Wei and L. Mai, *Joule*, 2018, **2**, 1991-2015.
122. S. Xin, Y. You, S. Wang, H.-C. Gao, Y.-X. Yin and Y.-G. Guo, *ACS Energy Letters*, 2017, **2**, 1385-1394.
123. C.-Z. Zhao, H. Duan, J.-Q. Huang, J. Zhang, Q. Zhang, Y.-G. Guo and L.-J. Wan, *Science China Chemistry*, 2019, **62**, 1286-1299.
124. C. Monroe and J. Newman, *Journal of The Electrochemical Society*, 2004, **151**, A880.
125. C. Monroe and J. Newman, *Journal of The Electrochemical Society*, 2005, **152**, A396.
126. P. Barai, K. Higa and V. Srinivasan, *Physical Chemistry Chemical Physics*, 2017, **19**, 20493-20505.
127. W. S. LePage, Y. Chen, E. Kazyak, K.-H. Chen, A. J. Sanchez, A. Poli, E. M. Arruda, M. Thouless and N. P. Dasgupta, *Journal of The Electrochemical Society*, 2019, **166**, A89-A97.
128. A. Masias, N. Felten, R. Garcia-Mendez, J. Wolfenstine and J. Sakamoto, *Journal of materials science*, 2019, **54**, 2585-2600.
129. L. Porz, T. Swamy, B. W. Sheldon, D. Rettenwander, T. Frömling, H. L. Thaman, S. Berendts, R. Uecker, W. C. Carter and Y. M. Chiang, *Advanced Energy Materials*, 2017, **7**, 1701003.
130. X. Liu, R. Garcia-Mendez, A. R. Lupini, Y. Cheng, Z. D. Hood, F. Han, A. Sharafi, J. C. Idrobo, N. J. Dudney and C. Wang, *Nature Materials*, 2021, **20**, 1485-1490.
131. T. Krauskopf, R. Dippel, H. Hartmann, K. Peppler, B. Mogwitz, F. H. Richter, W. G. Zeier and J. Janek, *Joule*, 2019, **3**, 2030-2049.
132. Z. Ning, D. S. Jolly, G. Li, R. De Meyere, S. D. Pu, Y. Chen, J. Kasemchainan, J. Ihli, C. Gong and B. Liu, *Nature Materials*, 2021, **20**, 1121-1129.
133. A. Banerjee, X. Wang, C. Fang, E. A. Wu and Y. S. Meng, *Chemical reviews*, 2020, **120**, 6878-6933.
134. R. Usiskin and J. Maier, *Advanced Energy Materials*, 2021, **11**, 2001455.
135. H. Tang, Z. Deng, Z. Lin, Z. Wang, I.-H. Chu, C. Chen, Z. Zhu, C. Zheng and S. P. Ong, *Chemistry of Materials*, 2018, **30**, 163-173.
136. C. Wang, W. Ping, Q. Bai, H. Cui, R. Hensleigh, R. Wang, A. H. Brozena, Z. Xu, J. Dai and Y. Pei, *Science*, 2020, **368**, 521-526.
137. C. Yang, H. Xie, W. Ping, K. Fu, B. Liu, J. Rao, J. Dai, C. Wang, G. Pastel and L. Hu, *Advanced Materials*, 2019, **31**, 1804815.
138. E. Kazyak, R. Garcia-Mendez, W. S. LePage, A. Sharafi, A. L. Davis, A. J. Sanchez, K.-H. Chen, C. Haslam, J. Sakamoto and N. P. Dasgupta, *Matter*, 2020, **2**, 1025-1048.
139. M. Wang, J. B. Wolfenstine and J. Sakamoto, *Electrochimica Acta*, 2019, **296**, 842-847.
140. J. Janek and W. G. Zeier, *Nature Energy*, 2023, **8**, 230-240.
141. C. Chen, M. Jiang, T. Zhou, L. Raijmakers, E. Vezhlev, B. Wu, T. U. Schüllli, D. L. Danilov, Y. Wei and R. A. Eichel, *Advanced Energy Materials*, 2021, **11**, 2003939.
142. S. Guo, Y. Sun and A. Cao, *Chemical Research in Chinese Universities*, 2020, **36**, 329-342.
143. M. Hansen, *Journal*, 1983.
144. R. M. Tiggelaar, V. Verdoold, H. Eghbali, G. Desmet and J. G. Gardeniers, *Lab on a Chip*, 2009, **9**, 456-463.
145. G. Bucci, T. Swamy, Y.-M. Chiang and W. C. Carter, *Journal of Materials Chemistry A*, 2017, **5**, 19422-19430.



146. Y. Liu, H. Su, M. Li, J. Xiang, X. Wu, Y. Zhong, X. Wang, X. Xia, C. Gu and J. Tu, *Journal of Materials Chemistry A*, 2021, **9**, 13531-13539. View Article Online
DOI: 10.1039/D1TB00101C
147. G. Liu, W. Weng, Z. Zhang, L. Wu, J. Yang and X. Yao, *Nano letters*, 2020, **20**, 6660-6665.
148. Z. Zhang, L. Zhang, X. Yan, H. Wang, Y. Liu, C. Yu, X. Cao, L. van Eijck and B. Wen, *Journal of Power Sources*, 2019, **410**, 162-170.
149. Y. Subramanian, R. Rajagopal, S. Kang and K.-S. Ryu, *Journal of Alloys and Compounds*, 2022, **925**, 166596.
150. H. Liu, Q. Zhu, C. Wang, G. Wang, Y. Liang, D. Li, L. Gao and L. Z. Fan, *Advanced Functional Materials*, 2022, **32**, 2203858.
151. A. C. Luntz, J. Voss and K. Reuter, *Journal*, 2015, **6**, 4599-4604.
152. H. Gerischer, F. Decker and B. Scrosati, *Journal of the Electrochemical Society*, 1994, **141**, 2297.
153. P. G. Bruce, *Solid state electrochemistry*, Cambridge university press, 1997.
154. G. Liu, H. Zheng, A. Simens, A. Minor, X. Song and V. Battaglia, *Journal of The Electrochemical Society*, 2007, **154**, A1129.
155. M. Manickam and M. Takata, *Electrochimica acta*, 2003, **48**, 957-963.
156. B. Stiaszny, J. C. Ziegler, E. E. Krauß, J. P. Schmidt and E. Ivers-Tiffée, *Journal of Power Sources*, 2014, **251**, 439-450.
157. R. Hausbrand, G. Cherkashinin, H. Ehrenberg, M. Gröting, K. Albe, C. Hess and W. Jaegermann, *Materials Science and Engineering: B*, 2015, **192**, 3-25.
158. T. Liu, L. Yu, J. Liu, J. Lu, X. Bi, A. Dai, M. Li, M. Li, Z. Hu and L. Ma, *Nature Energy*, 2021, **6**, 277-286.
159. B. Xiao, H. Liu, N. Chen, M. N. Banis, H. Yu, J. Liang, Q. Sun, T. K. Sham, R. Li and M. Cai, *Angewandte Chemie International Edition*, 2020, **59**, 14313-14320.
160. Y. Zhang, X. Sun, D. Cao, G. Gao, Z. Yang, H. Zhu and Y. Wang, *Energy Storage Materials*, 2021, **41**, 505-514.
161. T. Li, X.-Z. Yuan, L. Zhang, D. Song, K. Shi and C. Bock, *Electrochemical Energy Reviews*, 2020, **3**, 43-80.
162. S. P. Culver, R. Koerver, W. G. Zeier and J. Janek, *Advanced Energy Materials*, 2019, **9**, 1900626.
163. A. M. Nolan, Y. Zhu, X. He, Q. Bai and Y. Mo, *Joule*, 2018, **2**, 2016-2046.
164. D. H. Tan, A. Banerjee, Z. Chen and Y. S. Meng, *Nature nanotechnology*, 2020, **15**, 170-180.
165. Q. Xie, Z. Cui and A. Manthiram, *Advanced Materials*, 2021, **33**, 2100804.
166. V. Etacheri, R. Marom, R. Elazari, G. Salitra and D. Aurbach, *Energy & Environmental Science*, 2011, **4**, 3243-3262.
167. Y. Mao, X. Wang, S. Xia, K. Zhang, C. Wei, S. Bak, Z. Shadik, X. Liu, Y. Yang and R. Xu, *Advanced Functional Materials*, 2019, **29**, 1900247.
168. C. Wang, R. Yu, S. Hwang, J. Liang, X. Li, C. Zhao, Y. Sun, J. Wang, N. Holmes and R. Li, *Energy Storage Materials*, 2020, **30**, 98-103.
169. X. Li, W. Peng, R. Tian, D. Song, Z. Wang, H. Zhang, L. Zhu and L. Zhang, *Electrochimica Acta*, 2020, **363**, 137185.
170. R. Koerver, W. Zhang, L. de Biasi, S. Schweidler, A. O. Kondrakov, S. Kolling, T. Brezesinski, P. Hartmann, W. G. Zeier and J. Janek, *Energy & Environmental Science*, 2018, **11**, 2142-2158.
171. C. Liu, F. Roters and D. Raabe, *Nature Communications*, 2024, **15**, 7970.
172. C. Park, J. Lee, S. Lee, Y. J. Han, J. Kim and S. K. Jung, *Advanced Energy Materials*, 2023, **13**, 2203861.
173. T. Shi, Y.-Q. Zhang, Q. Tu, Y. Wang, M. Scott and G. Ceder, *Journal of Materials Chemistry A*, 2020, **8**, 17399-17404.
174. M. Clausnitzer, M. Ihrig, L. Cressa, S. Hein, M. Finsterbusch, S. Eswara, L.-Y. Kuo, T. Danner, P. Kaghazchi and D. Fattakhova-Rohlfing, *Energy Storage Materials*, 2024, **67**, 103262.
175. H. Huo, Y. Bai, S. L. Benz, T. Weintraut, S. Wang, A. Henss, D. Raabe and J. Janek, *Advanced Materials*, 2025, **37**, 2415006.
176. S. P. Jand and P. Kaghazchi, *MRS Communications*, 2018, **8**, 591-596.



177. B. Gao, R. Jalem, Y. Ma and Y. Tateyama, *Chemistry of Materials*, 2019, **32**, 85-96.
178. A. Sakuda, A. Hayashi and M. Tatsumisago, *Chemistry of Materials*, 2010, **22**, 949-956.
179. S. Lee, Y. Kim, C. Park, J. Kim, J.-S. Kim, H. Jo, C. J. Lee, S. Choi, D.-H. Seo and S.-K. Jung, *ACS Energy Letters*, 2024, **9**, 1369-1380.
180. P. Nzereogu, A. Oyesanya, S. Ogba, S. Ayanwunmi, M. Sobajo, V. Chimsunum, V. Ayanwunmi, M. Amoo, O. Adefemi and C. Chukwudi, *Hybrid Advances*, 2024, 100339.
181. S. J. Yang, J. K. Hu, F. N. Jiang, H. Yuan, H. S. Park and J. Q. Huang, *InfoMat*, 2024, **6**, e12512.
182. T. Kim, K. Kim, S. Lee, G. Song, M. S. Jung and K. T. Lee, *Chemistry of Materials*, 2022, **34**, 9159-9171.
183. X. Rui, D. Ren, X. Liu, X. Wang, K. Wang, Y. Lu, L. Li, P. Wang, G. Zhu and Y. Mao, *Energy & Environmental Science*, 2023, **16**, 3552-3563.
184. Y. Wang, X. Feng, W. Huang, X. He, L. Wang and M. Ouyang, *Advanced Energy Materials*, 2023, **13**, 2203841.
185. Y. Wang, X. Feng, Y. Peng, F. Zhang, D. Ren, X. Liu, L. Lu, Y. Nitta, L. Wang and M. Ouyang, *Joule*, 2022, **6**, 2810-2820.
186. A. Sakuda, A. Hayashi, T. Ohtomo, S. Hama and M. Tatsumisago, *Electrochemical and Solid-State Letters*, 2010, **13**, A73.
187. A. Sakuda, A. Hayashi, T. Ohtomo, S. Hama and M. Tatsumisago, *Journal of Power Sources*, 2011, **196**, 6735-6741.
188. A. Hayashi, K. Noi, A. Sakuda and M. Tatsumisago, *Nature communications*, 2012, **3**, 856.
189. A. Sakuda, A. Hayashi, Y. Takigawa, K. Higashi and M. Tatsumisago, *Journal of the Ceramic Society of Japan*, 2013, **121**, 946-949.
190. Y. Kubota, M. C. S. Escaño, H. Nakanishi and H. Kasai, *Journal of Applied Physics*, 2007, **102**.
191. M. Ashuri, Q. He and L. L. Shaw, *Nanoscale*, 2016, **8**, 74-103.
192. M. Gu, Z. Wang, J. G. Connell, D. E. Perea, L. J. Lauhon, F. Gao and C. Wang, *ACS nano*, 2013, **7**, 6303-6309.
193. A. Sakuda, A. Hayashi and M. Tatsumisago, *Scientific reports*, 2013, **3**, 2261.
194. J. Wu, S. Liu, F. Han, X. Yao and C. Wang, *Advanced Materials*, 2021, **33**, 2000751.
195. M. K. Tufail, P. Zhai, M. Jia, N. Zhao and X. Guo, *Energy Material Advances*, 2023, **4**, 0015.
196. M. Jia, M. Khurram Tufail and X. Guo, *ChemSusChem*, 2023, **16**, e202201801.
197. W. Qin, T. Nagase, Y. Umakoshi and J. Szpunar, *Philosophical Magazine Letters*, 2008, **88**, 169-179.
198. R. Sudo, Y. Nakata, K. Ishiguro, M. Matsui, A. Hirano, Y. Takeda, O. Yamamoto and N. Imanishi, *Solid State Ionics*, 2014, **262**, 151-154.
199. Y. Ren, Y. Shen, Y. Lin and C.-W. Nan, *Electrochemistry Communications*, 2015, **57**, 27-30.
200. M. Nagao, A. Hayashi, M. Tatsumisago, T. Kanetsuku, T. Tsuda and S. Kuwabata, *Physical Chemistry Chemical Physics*, 2013, **15**, 18600-18606.
201. R. Bradbury, G. F. Dewald, M. A. Kraft, T. Arlt, N. Kardjilov, J. Janek, I. Manke, W. G. Zeier and S. Ohno, *Advanced Energy Materials*, 2023, **13**, 2203426.
202. Y. Kimura, M. Fakkao, T. Nakamura, T. Okumura, N. Ishiguro, O. Sekizawa, K. Nitta, T. Uruga, M. Tada and Y. Uchimoto, *ACS Applied Energy Materials*, 2020, **3**, 7782-7793.
203. L. Froboese, J. F. Van Der Sichel, T. Loellhoeffel, L. Helmers and A. Kwade, *Journal of The Electrochemical Society*, 2019, **166**, A318.
204. A. Bielefeld, D. A. Weber and J. r. Janek, *The journal of physical chemistry C*, 2018, **123**, 1626-1634.
205. L. Ketter, N. Greb, T. Bernges and W. G. Zeier, *Nature Communications*, 2025, **16**, 1-9.
206. P. Minnmann, L. Quillman, S. Burkhardt, F. H. Richter and J. Janek, *Journal of The Electrochemical Society*, 2021, **168**, 040537.
207. J. Zahnow, T. Bernges, A. Wagner, N. Bohn, J. R. Binder, W. G. Zeier, M. T. Elm and J. r. Janek, *ACS Applied Energy Materials*, 2021, **4**, 1335-1345.
208. D. K. Ferry, *Science*, 2012, **335**, 45-46.



209. S. Kirkpatrick, *Reviews of modern physics*, 1973, **45**, 574.
210. M. E. Frary and C. A. Schuh, *Physical Review E—Statistical, Nonlinear, and Soft Matter Physics*, 2007, **76**, 041108.
211. S. Hao, Q. Zhang, X. Kong, Z. Wang, X. P. Gao and P. R. Shearing, *Advanced Energy Materials*, 2025, **15**, 2404384.
212. Z. Deng, Z. Wang, I.-H. Chu, J. Luo and S. P. Ong, *Journal of The Electrochemical Society*, 2015, **163**, A67.
213. Z. Jiang, Q. Han, S. Wang and H. Wang, *ChemElectroChem*, 2019, **6**, 2970-2983.
214. R. Schlenker, D. Stępień, P. Koch, T. Hupfer, S. Indris, B. Roling, V. Miß, A. Fuchs, M. Wilhelmi and H. Ehrenberg, *ACS applied materials & interfaces*, 2020, **12**, 20012-20025.
215. G. G. Serbessa, Y. Nikodimos, B. W. Taklu, S. K. Merso, Z. B. Muche, B. D. Dandena, S. A. Vallal, T.-I. Yeh, F. Valencia and Y.-F. Hung, *Energy Storage Materials*, 2025, 104103.
216. L. E. Camacho-Forero and P. B. Balbuena, *Journal of Power Sources*, 2018, **396**, 782-790.
217. K. J. Kim and J. L. Rupp, *Energy & Environmental Science*, 2020, **13**, 4930-4945.
218. Y. Kimura, T. Fujisaki, T. Shimizu, T. Nakamura, Y. Iriyama and K. Amezawa, *Communications Materials*, 2024, **5**, 125.
219. Y. Xiao, L. J. Miara, Y. Wang and G. Ceder, *Joule*, 2019, **3**, 1252-1275.
220. H.-S. Kim, Y. Kim, S.-I. Kim and S. W. Martin, *Journal of power sources*, 2006, **161**, 623-627.
221. N. Ohta, K. Takada, L. Zhang, R. Ma, M. Osada and T. Sasaki, *Advanced Materials*, 2006, **18**, 2226-2229.
222. T. Kato, T. Hamanaka, K. Yamamoto, T. Hirayama, F. Sagane, M. Motoyama and Y. Iriyama, *Journal of Power Sources*, 2014, **260**, 292-298.
223. K. H. Kim, Y. Iriyama, K. Yamamoto, S. Kumazaki, T. Asaka, K. Tanabe, C. A. Fisher, T. Hirayama, R. Murugan and Z. Ogumi, *Journal of Power Sources*, 2011, **196**, 764-767.
224. D. Rettenwander, R. Wagner, A. Reyer, M. Bonta, L. Cheng, M. M. Doeff, A. Limbeck, M. Wilkening and G. Amthauer, *The Journal of Physical Chemistry C*, 2018, **122**, 3780-3785.
225. J. A. Lewis, F. J. Q. Cortes, M. G. Boebinger, J. Tippens, T. S. Marchese, N. Kondekar, X. Liu, M. Chi and M. T. McDowell, *ACS Energy Letters*, 2019, **4**, 591-599.
226. Z. D. Hood, A. U. Mane, A. Sundar, S. Tepavcevic, P. Zapol, U. D. Eze, S. P. Adhikari, E. Lee, G. E. Sterbinsky and J. W. Elam, *Advanced Materials*, 2023, **35**, 2300673.
227. M. Balaish, J. C. Gonzalez-Rosillo, K. J. Kim, Y. Zhu, Z. D. Hood and J. L. Rupp, *Nature Energy*, 2021, **6**, 227-239.
228. J. C. Bachman, S. Muy, A. Grimaud, H.-H. Chang, N. Pour, S. F. Lux, O. Paschos, F. Maglia, S. Lupart and P. Lamp, *Chemical reviews*, 2016, **116**, 140-162.
229. J. Maier, *Journal of The Electrochemical Society*, 1987, **134**, 1524.
230. J. Maier, *Progress in solid state chemistry*, 1995, **23**, 171-263.
231. E. Rangasamy, G. Sahu, J. K. Keum, A. J. Rondinone, N. J. Dudney and C. Liang, *Journal of Materials Chemistry A*, 2014, **2**, 4111-4116.
232. Z. D. Hood, H. Wang, Y. Li, A. S. Pandian, M. P. Paranthaman and C. Liang, *Solid State Ionics*, 2015, **283**, 75-80.
233. B. Ransom, A. Ramdas, E. Lomeli, J. Fidawi, A. Sendek, T. Devereaux, E. J. Reed and P. Schindler, *ACS Applied Materials & Interfaces*, 2023, **15**, 44394-44403.
234. F. Yang, S. Lin, Z. Guo, Y. Shao, B. Zhang, X. Zhang, S. Yan and A. A. Volinsky, *Journal of Alloys and Compounds*, 2019, **805**, 1034-1043.
235. E. Temeche, S. Indris and R. M. Laine, *ACS Applied Materials & Interfaces*, 2020, **12**, 46119-46131.
236. Y. Wu, D. Lei and C. Wang, *Materials Today Physics*, 2021, **18**, 100395.
237. S. Ito, S. Fujiki, T. Yamada, Y. Aihara, Y. Park, T. Y. Kim, S.-W. Baek, J.-M. Lee, S. Doo and N. Machida, *Journal of Power Sources*, 2014, **248**, 943-950.
238. S. Miyakawa, S. Matsuda, N. Tanibata, H. Takeda, M. Nakayama, T. Saito and S. Fukuchi, *Scientific Reports*, 2022, **12**, 16672.

View Article Online
DOI: 10.1039/D5EB00101C



239. R. Johnson Jr, B. Morosin, M. Knotek and R. Biefeld, *Physics Letters A*, 1975, **54**, 403-404.
240. F. Shin-ichi, S. Satoshi, S. Kaduhiro and T. Hitoshi, *Solid State Ionics*, 2004, **167**, 325-329.
241. Y. Sun, F. Li, Q. Qiao, J. Cao, Y. Wang and S. Ye, *Electrochimica Acta*, 2015, **176**, 1464-1475.
242. P. Quintana, F. Velasco and A. West, *Solid State Ionics*, 1989, **34**, 149-155.
243. C. Wang, K. Aoyagi, P. Wisesa and T. Mueller, *Chemistry of Materials*, 2020, **32**, 3741-3752.
244. H. Zhou, S. Yu, H. Liu and P. Liu, *Journal of Power Sources*, 2020, **450**, 227632.
245. C. Niu, H. Lee, S. Chen, Q. Li, J. Du, W. Xu, J.-G. Zhang, M. S. Whittingham, J. Xiao and J. Liu, *Nature Energy*, 2019, **4**, 551-559.
246. C. Fang, J. Li, M. Zhang, Y. Zhang, F. Yang, J. Z. Lee, M.-H. Lee, J. Alvarado, M. A. Schroeder and Y. Yang, *Nature*, 2019, **572**, 511-515.
247. Q. Cheng, L. Wei, Z. Liu, N. Ni, Z. Sang, B. Zhu, W. Xu, M. Chen, Y. Miao and L.-Q. Chen, *Nature communications*, 2018, **9**, 2942.
248. Z. Tu, S. Choudhury, M. J. Zachman, S. Wei, K. Zhang, L. F. Kourkoutis and L. A. Archer, *Joule*, 2017, **1**, 394-406.
249. Y. Gao, Z. Yan, J. L. Gray, X. He, D. Wang, T. Chen, Q. Huang, Y. C. Li, H. Wang and S. H. Kim, *Nature materials*, 2019, **18**, 384-389.
250. Y. Liu, Q. Sun, Y. Zhao, B. Wang, P. Kaghazchi, K. R. Adair, R. Li, C. Zhang, J. Liu and L.-Y. Kuo, *ACS applied materials & interfaces*, 2018, **10**, 31240-31248.
251. L. Sang, K. L. Bassett, F. C. Castro, M. J. Young, L. Chen, R. T. Haasch, J. W. Elam, V. P. Dravid, R. G. Nuzzo and A. A. Gewirth, *Chemistry of Materials*, 2018, **30**, 8747-8756.
252. P. Hartmann, T. Leichtweiss, M. R. Busche, M. Schneider, M. Reich, J. Sann, P. Adelhelm and J. Janek, *The Journal of Physical Chemistry C*, 2013, **117**, 21064-21074.
253. Y. Ruan, Y. Lu, X. Huang, J. Su, C. Sun, J. Jin and Z. Wen, *Journal of Materials Chemistry A*, 2019, **7**, 14565-14574.
254. Z. Zhang, S. Chen, J. Yang, J. Wang, L. Yao, X. Yao, P. Cui and X. Xu, *ACS applied materials & interfaces*, 2018, **10**, 2556-2565.
255. Y. Zhu, X. He and Y. Mo, *Advanced Science*, 2017, **4**, 1600517.
256. Q. Cheng, A. Li, N. Li, S. Li, A. Zangiabadi, W. Huang, A. C. Li, T. Jin, Q. Song and W. Xu, *Joule*, 2019, **3**, 1510-1522.
257. M. Shigeno, K. Nagao, M. Deguchi, C. Hotehama, H. Kowada, A. Sakuda, A. Hayashi and M. Tatsumisago, *Solid State Ionics*, 2019, **339**, 114985.
258. R. Court-Castagnet, C. Kaps, C. Cros and P. Hagenmuller, *Solid state ionics*, 1993, **61**, 327-334.
259. T. Tsujimura, S. Ito, K. Yoshida, Y. Higashiyama, Y. Aihara, N. Machida, Y. Park and D. Im, *Solid State Ionics*, 2022, **383**, 115970.
260. H. Lutz, W. Schmidt and H. Haeuseler, *Journal of Physics and Chemistry of Solids*, 1981, **42**, 287-289.
261. M. Calpa, N. C. Rosero-Navarro, A. Miura and K. Tadanaga, *Journal of Sol-Gel Science and Technology*, 2022, 1-8.
262. Y. Zheng, W. Zhang, J. Gui, Q. Cao, Y. Wang, Y. Xu, Y. Liu and Y. Liang, *Energy Storage Materials*, 2023, **61**, 102884.
263. Y. Zhu, X. He and Y. Mo, *Journal of Materials Chemistry A*, 2016, **4**, 3253-3266.
264. J. Liang, Y. Zhu, X. Li, J. Luo, S. Deng, Y. Zhao, Y. Sun, D. Wu, Y. Hu and W. Li, *Nature Communications*, 2023, **14**, 146.
265. J. Li, M. Zhang, D. Zhang, Y. Yan and Z. Li, *Chemical engineering journal*, 2020, **402**, 126195.
266. Z. Ahaliabadeh, X. Kong, E. Fedorovskaya and T. Kallio, *Journal of Power Sources*, 2022, **540**, 231633.
267. H. H. Sun, U.-H. Kim, J.-H. Park, S.-W. Park, D.-H. Seo, A. Heller, C. B. Mullins, C. S. Yoon and Y.-K. Sun, *Nature communications*, 2021, **12**, 6552.
268. G.-T. Park, B. Namkoong, S.-B. Kim, J. Liu, C. S. Yoon and Y.-K. Sun, *Nature Energy*, 2022, **7**, 946-954.



269. D. Shumei, T. Dan, L. Ping, L. Huiqin, W. Fenyan and H. Zhang, *Journal of Solid State Electrochemistry*, 2023, **27**, 1-23. View Article Online
DOI: 10.1039/D3EB00101C
270. L. Xu, F. Zhou, B. Liu, H. Zhou, Q. Zhang, J. Kong and Q. Wang, *International Journal of Electrochemistry*, 2018, **2018**, 1-12.
271. Q. Liu, Y. Zhang, J. Gao, Z. Zhou, H. Wang, K. Wang, X. Zhang, L. Li and J.-F. Li, *Energy & Environmental Science*, 2018, **11**, 3531-3539.
272. F. Han, J. Yue, X. Zhu and C. Wang, *Advanced Energy Materials*, 2018, **8**, 1703644.
273. G. Liu, D. Xie, X. Wang, X. Yao, S. Chen, R. Xiao, H. Li and X. Xu, *Energy Storage Materials*, 2019, **17**, 266-274.
274. N. Wang, K. Yang, L. Zhang, X. Yan, L. Wang and B. Xu, *Journal of Materials Science*, 2018, **53**, 1987-1994.
275. A. Kato, M. Nagao, A. Sakuda, A. Hayashi and M. Tatsumisago, *Journal of the Ceramic Society of Japan*, 2014, **122**, 552-555.
276. Y. Xia, J. Li, J. Zhang, X. Zhou, H. Huang, X. He, Y. Gan, Z. Xiao and W. Zhang, *Journal of Power Sources*, 2022, **543**, 231846.
277. Z. Jiang, H. Peng, Y. Liu, Z. Li, Y. Zhong, X. Wang, X. Xia, C. Gu and J. Tu, *Advanced Energy Materials*, 2021, **11**, 2101521.
278. L. Zhou, A. Assoud, Q. Zhang, X. Wu and L. F. Nazar, *Journal of the American Chemical Society*, 2019, **141**, 19002-19013.
279. V. Y. Prokhorenko, V. V. Roshchupkin, M. A. Pokrasin, S. Prokhorenko and V. Kotov, *High Temperature*, 2000, **38**, 954-968.
280. H. Ge, H. Li, S. Mei and J. Liu, *Renewable and Sustainable Energy Reviews*, 2013, **21**, 331-346.
281. J. Liu, Y.-X. Zhou, Y.-G. Lv and T. Li, 2005.
282. H. Ge and J. Liu, *Frontiers in Energy*, 2012, **6**, 207-209.
283. H. Ge and J. Liu, *Journal of heat transfer*, 2013, **135**, 054503.
284. S. Chen, D. Xie, G. Liu, J. P. Mwizerwa, Q. Zhang, Y. Zhao, X. Xu and X. Yao, *Energy Storage Materials*, 2018, **14**, 58-74.
285. J. Lau, R. H. DeBlock, D. M. Butts, D. S. Ashby, C. S. Choi and B. S. Dunn, *Advanced Energy Materials*, 2018, **8**, 1800933.
286. Z. Gao, H. Sun, L. Fu, F. Ye, Y. Zhang, W. Luo and Y. Huang, *Advanced materials*, 2018, **30**, 1705702.
287. W. Zhang, F. H. Richter, S. P. Culver, T. Leichtweiss, J. G. Lozano, C. Dietrich, P. G. Bruce, W. G. Zeier and J. r. Janek, *ACS applied materials & interfaces*, 2018, **10**, 22226-22236.
288. R. Koerver, F. Walther, I. Aygün, J. Sann, C. Dietrich, W. G. Zeier and J. Janek, *Journal of Materials Chemistry A*, 2017, **5**, 22750-22760.
289. W. Zhang, T. Leichtweiß, S. P. Culver, R. Koerver, D. Das, D. A. Weber, W. G. Zeier and J. r. Janek, *ACS applied materials & interfaces*, 2017, **9**, 35888-35896.
290. A. Banerjee, H. Tang, X. Wang, J.-H. Cheng, H. Nguyen, M. Zhang, D. H. Tan, T. A. Wynn, E. A. Wu and J.-M. Doux, *ACS applied materials & interfaces*, 2019, **11**, 43138-43145.
291. D. H. Tan, A. Banerjee, Z. Deng, E. A. Wu, H. Nguyen, J.-M. Doux, X. Wang, J.-h. Cheng, S. P. Ong and Y. S. Meng, *ACS Applied Energy Materials*, 2019, **2**, 6542-6550.
292. S. Luo, Z. Wang, X. Li, X. Liu, H. Wang, W. Ma, L. Zhang, L. Zhu and X. Zhang, *Nature Communications*, 2021, **12**, 6968.
293. W. Fitzhugh, L. Ye and X. Li, *Journal of Materials Chemistry A*, 2019, **7**, 23604-23627.
294. W. Hao, M. Lee and G. S. Hwang, *Journal of Power Sources*, 2023, **560**, 232689.
295. Z. Jiang, T. Liang, Y. Liu, S. Zhang, Z. Li, D. Wang, X. Wang, X. Xia, C. Gu and J. Tu, *ACS Applied Materials & Interfaces*, 2020, **12**, 54662-54670.
296. T. Chen, D. Zeng, L. Zhang, M. Yang, D. Song, X. Yan and C. Yu, *Journal of Energy Chemistry*, 2021, **59**, 530-537.
297. H. Xu, G. Cao, Y. Shen, Y. Yu, J. Hu, Z. Wang and G. Shao, *Energy & Environmental Materials*, 2022, **5**, 852-864.



298. Z. Wang, Y. Jiang, J. Wu, Y. Jiang, W. Ma, Y. Shi, X. Liu, B. Zhao, Y. Xu and J. Zhang, *Nano Energy*, 2021, **84**, 105906. View Article Online
DOI: 10.1039/D1EB00101C
299. Z. Jiang, Y. Liu, H. Peng, J. Li, X. Xu, H. Su, Y. Zhong, X. Wang, C. Gu and J. Tu, *Energy Storage Materials*, 2023, **56**, 300-309.
300. Y. Kato, S. Shiotani, K. Morita, K. Suzuki, M. Hirayama and R. Kanno, *The journal of physical chemistry letters*, 2018, **9**, 607-613.
301. A. M. Stavola, X. Sun, D. P. Guida, A. M. Bruck, D. Cao, J. S. Okasinski, A. C. Chuang, H. Zhu and J. W. Gallaway, *ACS Energy Letters*, 2023, **8**, 1273-1280.
302. D. Cao, Y. Zhao, X. Sun, A. Natan, Y. Wang, P. Xiang, W. Wang and H. Zhu, *ACS Energy Letters*, 2020, **5**, 3468-3489.
303. M. A. Kraft, S. Ohno, T. Zinkevich, R. Koerver, S. P. Culver, T. Fuchs, A. Senyshyn, S. Indris, B. J. Morgan and W. G. Zeier, *Journal of the American Chemical Society*, 2018, **140**, 16330-16339.
304. W. Zhang, D. A. Weber, H. Weigand, T. Arlt, I. Manke, D. Schröder, R. Koerver, T. Leichtweiss, P. Hartmann and W. G. Zeier, *ACS applied materials & interfaces*, 2017, **9**, 17835-17845.
305. M. Otoyama, A. Sakuda, M. Tatsumisago and A. Hayashi, *ACS applied materials & interfaces*, 2020, **12**, 29228-29234.
306. L. Ye and X. Li, *Nature*, 2021, **593**, 218-222.
307. P. Adeli, J. D. Bazak, K. H. Park, I. Kochetkov, A. Huq, G. R. Goward and L. F. Nazar, *Angewandte Chemie International Edition*, 2019, **58**, 8681-8686.
308. T. Krauskopf, F. H. Richter, W. G. Zeier and J. r. Janek, *Chemical reviews*, 2020, **120**, 7745-7794.
309. S. Samanta, S. Bera, R. K. Biswas, S. Mondal, L. Mandal and A. Banerjee, *ACS Energy Letters*, 2024, **9**, 3683-3693.
310. M. Sakuma, K. Suzuki, M. Hirayama and R. Kanno, *Solid State Ionics*, 2016, **285**, 101-105.
311. L. Yang, Z. Wang, Y. Feng, R. Tan, Y. Zuo, R. Gao, Y. Zhao, L. Han, Z. Wang and F. Pan, *Advanced Energy Materials*, 2017, **7**, 1701437.
312. C. Yu, S. Ganapathy, E. R. v. Eck, H. Wang, S. Basak, Z. Li and M. Wagemaker, *Nature communications*, 2017, **8**, 1086.
313. T. Kato, R. Yoshida, K. Yamamoto, T. Hirayama, M. Motoyama, W. C. West and Y. Iriyama, *Journal of Power Sources*, 2016, **325**, 584-590.
314. L. Mai, M. Yan and Y. Zhao, *Nature*, 2017, **546**, 469-470.
315. S. A. Pervez, M. A. Cambaz, V. Thangadurai and M. Fichtner, *ACS applied materials & interfaces*, 2019, **11**, 22029-22050.
316. B. Aktekin, L. M. Riegger, S.-K. Otto, T. Fuchs, A. Henss and J. Janek, *Nature Communications*, 2023, **14**, 6946.
317. Y. Huang, X. Li, J. Wang, L. Miao, C. Li, J. Han and Y. Huang, *Energy Storage Materials*, 2018, **15**, 108-115.
318. J. Yang, Z. Gao, T. Ferber, H. Zhang, C. Guhl, L. Yang, Y. Li, Z. Deng, P. Liu and C. Cheng, *Journal of materials chemistry A*, 2020, **8**, 7828-7835.
319. B. Aktekin, E. Kataev, L. M. Riegger, R. Garcia-Diez, Z. Chalkley, J. Becker, R. G. Wilks, A. Henss, M. Bär and J. r. Janek, *ACS Energy Letters*, 2024, **9**, 3492-3500.
320. X.-S. Zhang, J. Wan, Z.-Z. Shen, S.-Y. Lang, S. Xin, R. Wen, Y.-G. Guo and L.-J. Wan, *Angewandte Chemie International Edition*, e202409435.
321. Y. Li, Z. Gao, F. Hu, X. Lin, Y. Wei, J. Peng, J. Yang, Z. Li, Y. Huang and H. Ding, *Small Methods*, 2020, **4**, 2000111.
322. R.-J. Chen, Y.-B. Zhang, T. Liu, B.-Q. Xu, Y.-H. Lin, C.-W. Nan and Y. Shen, *ACS applied materials & interfaces*, 2017, **9**, 9654-9661.
323. B. Liu, K. Fu, Y. Gong, C. Yang, Y. Yao, Y. Wang, C. Wang, Y. Kuang, G. Pastel and H. Xie, *Nano letters*, 2017, **17**, 4917-4923.
324. X. Li, Q. Sun, Z. Wang, D. Song, H. Zhang, X. Shi, C. Li, L. Zhang and L. Zhu, *Journal of Power Sources*, 2020, **456**, 227997.



325. X. Li, J. Liang, M. N. Banis, J. Luo, C. Wang, W. Li, X. Li, Q. Sun, Y. Hu and Q. Xiao, *Energy Storage Materials*, 2020, **28**, 325-333. View Article Online
DOI: 10.1039/C9SEB00101C
326. Y. Zhou, C. Doerr, J. Kasemchainan, P. G. Bruce, M. Pasta and L. J. Hardwick, *Batteries & supercaps*, 2020, **3**, 647-652.
327. D. Zeng, J. Yao, L. Zhang, R. Xu, S. Wang, X. Yan, C. Yu and L. Wang, *Nature Communications*, 2022, **13**, 1909.
328. J. Dai, C. Yang, C. Wang, G. Pastel and L. Hu, *Advanced Materials*, 2018, **30**, 1802068.
329. P. Nellist, B. McCallum and J. M. Rodenburg, *nature*, 1995, **374**, 630-632.
330. P. Vadhva, J. Hu, M. J. Johnson, R. Stocker, M. Braglia, D. J. Brett and A. J. Rettie, *ChemElectroChem*, 2021, **8**, 1930-1947.
331. C. Wei, C. Yu, L. Peng, Z. Zhang, R. Xu, Z. Wu, C. Liao, W. Zhang, L. Zhang and S. Cheng, *Materials Advances*, 2022, **3**, 1047-1054.
332. C. Yu, J. Hageman, S. Ganapathy, L. van Eijck, L. Zhang, K. R. Adair, X. Sun and M. Wagemaker, *Journal of Materials Chemistry A*, 2019, **7**, 10412-10421.
333. L. H. Adem, B. N. Olana, B. W. Taklu, B. D. Dandena, G. G. Serbessa, B.-J. Hwang and S. D. Lin, *Electrochimica Acta*, 2024, **498**, 144622.
334. S.-K. Jiang, S.-C. Yang, W.-H. Huang, H.-Y. Sung, R.-Y. Lin, J.-N. Li, B.-Y. Tsai, T. Agnihotri, Y. Nikodimos and C.-H. Wang, *Journal of Materials Chemistry A*, 2023, **11**, 2910-2919.
335. Y. Wu, C. Li, X. Zheng, W. Zhao, H. Wang, J. Gu, Y. Cheng, Y. Lin, Y. Su and F. Ren, *ACS Energy Letters*, 2024, **9**, 5156-5165.
336. Z. Xu, X. Guo, W. Song, J. Wang, T. Qin, Y. Yuan and J. Lu, *Advanced Materials*, 2024, **36**, 2303612.
337. Q. Zhang, Y. Huang, Y. Liu, S. Sun, K. Wang, Y. Li, X. Li, J. Han and Y. Huang, *Sci China Mater*, 2017, **60**, 629-636.
338. H.-M. Hau, T. Mishra, C. Ophus, T.-Y. Huang, K. Bustilo, Y. Sun, X. Yang, T. Holstun, X. Zhao and S. Wang, *Nature Nanotechnology*, 2024, 1-9.
339. M. Okubo, Y. Mizuno, H. Yamada, J. Kim, E. Hosono, H. Zhou, T. Kudo and I. Honma, *ACS nano*, 2010, **4**, 741-752.
340. H. Ji, J. Wu, Z. Cai, J. Liu, D.-H. Kwon, H. Kim, A. Urban, J. K. Papp, E. Foley and Y. Tian, *Nature Energy*, 2020, **5**, 213-221.
341. J. Aspinall, D. E. Armstrong and M. Pasta, *Materials today energy*, 2022, **30**, 101183.
342. N. Brodusch, K. Zaghib and R. Gauvin, *Microscopy Research and Technique*, 2015, **78**, 30-39.
343. A. Bastos, S. Zaefferer and D. Raabe, *Journal of microscopy*, 2008, **230**, 487-498.
344. S.-K. Otto, Y. Moryson, T. Krauskopf, K. Pepler, J. Sann, J. r. Janek and A. Henss, *Chemistry of Materials*, 2021, **33**, 859-867.
345. S.-K. Otto, T. Fuchs, Y. Moryson, C. Lerch, B. Mogwitz, J. Sann, J. r. Janek and A. Henss, *ACS Applied Energy Materials*, 2021, **4**, 12798-12807.
346. S. Kaboli, P. Noel, D. Clément, H. Demers, A. Paoletta, P. Bouchard, M. L. Trudeau, J. B. Goodenough and K. Zaghib, *Science Advances*, 2020, **6**, eabd5708.
347. H. Somekawa, K. Nishikawa, T. Moronaga and T. Ohmura, *Journal of Power Sources*, 2023, **569**, 233019.
348. E. Darnbrough, J. Aspinall, M. Pasta and D. E. Armstrong, *Materials & Design*, 2023, **233**, 112200.
349. T. Fuchs, T. Ortmann, J. Becker, C. G. Haslam, M. Ziegler, V. K. Singh, M. Rohnke, B. Mogwitz, K. Pepler and L. F. Nazar, *Nature Materials*, 2024, 1-8.
350. M. Motoyama, M. Hirota, T. Yamamoto and Y. Iriyama, *ACS applied materials & interfaces*, 2020, **12**, 38045-38053.
351. T. Fuchs, J. Becker, C. G. Haslam, C. Lerch, J. Sakamoto, F. H. Richter and J. Janek, *Advanced Energy Materials*, 2023, **13**, 2203174.
352. M. J. Wang, E. Carmona, A. Gupta, P. Albertus and J. Sakamoto, *Nature Communications*, 2020, **11**, 5201.



353. Y. Li, Y. Li and Y. Cui, *Chem*, 2018, **4**, 2250-2252.
354. Y. Li, W. Huang, Y. Li, A. Pei, D. T. Boyle and Y. Cui, *Joule*, 2018, **2**, 2167-2177.
355. X. Wang, M. Zhang, J. Alvarado, S. Wang, M. Sina, B. Lu, J. Bouwer, W. Xu, J. Xiao and J.-G. Zhang, *Nano letters*, 2017, **17**, 7606-7612.
356. X. Wang, Y. Li and Y. S. Meng, *Joule*, 2018, **2**, 2225-2234.
357. Y. Li, Y. Li, A. Pei, K. Yan, Y. Sun, C.-L. Wu, L.-M. Joubert, R. Chin, A. L. Koh and Y. Yu, *Science*, 2017, **358**, 506-510.
358. M. J. Zachman, Z. Tu, S. Choudhury, L. A. Archer and L. F. Kourkoutis, *Nature*, 2018, **560**, 345-349.
359. A. Schwöbel, R. Hausbrand and W. Jaegermann, *Solid State Ionics*, 2015, **273**, 51-54.
360. D. Huang, G. Liu and W. Tong, *Small*, 2024, 2406862.
361. M. Motoyama, M. Ejiri and Y. Iriyama, *Journal of The Electrochemical Society*, 2015, **162**, A7067.
362. H. Huo, M. Jiang, Y. Bai, S. Ahmed, K. Volz, H. Hartmann, A. Henss, C. V. Singh, D. Raabe and J. Janek, *Nature Materials*, 2024, 1-9.

View Article Online
DOI: 10.1039/D5EB00101C



Data Availability Statement

View Article Online
DOI: 10.1039/D5EB00101C

The data supporting this article have been included as part of the Supplementary Information, which can be accessed via the link:

<https://www.....> Other data could be available upon kind request by contacting the corresponding authors.

